Dissertation ETH number : 18233

Invariant Manifolds and Lattice Boltzmann Method for Combustion

A dissertation submitted to

ETH Zurich

for the degree of

Doctor of Sciences (Dr. sc. ETH Zurich)

presented by

Eliodoro Chiavazzo

Dipl.-Ing. University of Naples, Federico II

born 25th May 1978

citizen of Italy

accepted on the recommendation of

Prof. Dr.-Ing. Konstantinos B. Boulouchos, examiner

Dr. Iliya V. Karlin, co-examiner

Prof. Dr. Hans J. Herrmann, co-examiner

Zurich, 2009

Invariant Manifolds and Lattice Boltzmann Method for Combustion

Published and distributed by:

Aerothermochemistry and Combustion Systems Laboratory
Institute of Energy Technology (IET)
Swiss Federal Institute of Technology (ETH) Zurich
ETH Zentrum, ML
8092 Zurich
Switzerland
`http://www.lav.ethz.ch/`

Printed in Switzerland by:

ETH Reprozentrale Hönggerberg
HIL C45
8093 Zurich
Switzerland

To Antonio and Prudenziana

Lentamente muore
chi diventa schiavo dell'abitudine,
ripetendo ogni giorno gli stessi percorsi,
chi non cambia la marcia,
chi non rischia e cambia colore dei vestiti,
chi non parla a chi non conosce.
Muore lentamente chi evita una passione,
chi preferisce il nero su bianco
e i puntini sulle "i"
piuttosto che un insieme di emozioni,
proprio quelle che fanno brillare gli occhi,
quelle che fanno di uno sbadiglio un sorriso,
quelle che fanno battere il cuore
davanti all'errore e ai sentimenti.
Lentamente muore
chi non capovolge il tavolo,
chi è infelice sul lavoro,
chi non rischia la certezza per l'incertezza per inseguire un sogno,
chi non si permette almeno una volta nella vita, di fuggire ai consigli sensati.
Lentamente muore chi non viaggia,
chi non legge,
chi non ascolta musica,
chi non trova grazia in se stesso.
Muore lentamente chi distrugge l'amor proprio,
chi non si lascia aiutare
chi passa i giorni a lamentarsi
della propria sfortuna o della pioggia incessante.
Lentamente muore
chi abbandona un progetto prima di iniziarlo,
chi non fa domande sugli argomenti che non conosce,
chi non risponde quando gli chiedono qualcosa che conosce.
Evitiamo la morte a piccole dosi,
ricordando sempre che essere vivo
richiede uno sforzo di gran lunga maggiore del semplice fatto di respirare.
Soltanto l'ardente pazienza
porterà al raggiungimento
di una splendida felicità.

Dies slowly
he who becomes the slave of habit,
repeating every day the same itineraries,
who never changes pace,
who does not risk and change the color of his clothes,
who doesn't talk to whom doesn't know.
Dies slowly he who shuns passion,
who prefers black on white,
dotting ones "is"
rather than a whirlpool of emotions,
the kind that make your eyes glimmer,
that turn a yawn into a smile,
that make the heart pound
in the face of mistakes and feelings.
Dies slowly
he who does not overthrow the table
when is unhappy at work,
who does not risk certain for uncertain to thus follow a dream,
he who do not forego sound advice at least once in their lives.
Dies slowly he who does not travel,
who does not read,
who does not listen to music,
who does not find grace in himself.
Dies slowly he who destroys his self love,
who does not accept somebody's help.
Dies slowly he who passes his days complaining
of his bad luck or the rain that never stops.
Dies slowly
he who abandons a project before starting it,
who fail to ask questions over a subjects that does not know
or who doesn't reply when asked about something he knows.
Let's avoid death in small doses,
always reminding oneself that being alive
demands an effort by far greater than the simple fact of breathing.
Only a burning patience
will lead to the attainment
of a splendid happiness.

Martha Medeiros

Acknowledgements

I like to consider my PhD degree as a target which led me towards a new road. However, new roads can be taken only if we are ready to take on a big risk as well, hence, once we make this decision, we start keeping our goal in mind and this helps to ride over the difficulties.

Wise people say that we need to enjoy the journey rather than the final destination itself, but I realized that we are generally too busy to care of that. I also understood that once we get to the end of the way, we turn around and promptly have the impression that those people were definitely right.

Therefore, in order to prevent any regrets, it becomes absolutely crucial to meet enthusiastic travel-mates and experienced guides on our pathway: the first ones share good events with us and can make bad events less bitter, the second ones can shed light on the right path whenever we grope in the dark. Now at the end of my PhD, I can turn around and feel the pleasure to remember in these few lines friends and guides met along the way.

First of all, I want to thank my scientific advisor Dr. Ilya Karlin who thought that I am the right candidate for this job, for offering his expertise during these years and for the ideas which came to my mind after our discussions. I want to reserve a special thank to Prof. Konstantinos Boulouchos: I shall never forget his kindness and encouragements in doing well. I really appreciate his attitude to take into big consideration, along with work, any aspects of life. I am indebted to Dr. Christos Frouzakis for suggestions, hints and the precious help offered whenever I was asking. Prof. Alexander Gorban is sincerely acknowledged for his suggestions and very helpful comments. I wish to state my appreciation to Prof. Hans Herrmann for accepting to be co-referee of this thesis.

I express my gratitude to all colleagues at LAV: I enjoyed so much the great time we had together in many occasions. In particular, I had the pleasure to work close to my long-standing friend Gianmarco Pizza, and to meet a wise person as Fabrizio Noembrini. I have appreciated the friendship

of Matteo Colangeli and Shyam Chikatamarla. Nikos Prasianakis and Evangelos Boutsianis deserve a special mention for sharing with me, not only the same office for long time, but also many thoughts about technical issues and philosophic aspects of Life.

A special thank goes to Marianna for her strength in facing sometimes my moodiness, and for providing me with love and support whenever needed in spite of the physical distances between us. I also have the pleasure to mention here my close friends Davide Belpedio, Luca Iovino and Alfonso Capozzoli.

Last but not least, I thank my parents. My gratitude to them, although great, will never be able to pay back their endless love and substantial contribution to the person I am today. For this reason, the present thesis is entirely dedicated to them.

The work presented in this thesis was accomplished at the Laboratory of Aero- thermochemistry and Combustion systems (LAV) of the Swiss Federal Institute of Techology in Zurich mostly under the financial support of Swiss National Science Foundation (SNF, Project 200021-107885/1).

Eliodoro Chiavazzo,
March 2009, Zurich.

Contents

Sommario

Negli ultimi decenni, è diventato di estrema importanza poter calcolare con affidabilità il processo di formazione degli inquinanti prodotti dalla combustione, a causa delle normative sempre più stringenti in materia. D'altra parte, oggigiorno, le simulazioni numeriche rappresentano uno strumento indispensabile sia per investigazioni meramente scientifiche che per la pratica tecnica. Calcoli al computer che usino dati sperimentali risultano essere difatti un mezzo potente, di basso costo ed affidabile per studiare i processi di combustione.

Sfortunatamente, nella maggioranza dei casi, i calcoli di emissione di specie inquinanti in atmosfera richiedono uno studio dettagliato dei meccanismi di reazione chimica, che possono includere centinaia di specie. In tal caso, infatti, l'uso di schemi di reazione semplificati è del tutto inadeguato. Dato che ogni componente coinvolto comporta la risoluzione di un'equazione di trasporto aggiuntiva, ne consegue un costo della simulazione tremendamente alto, sia in termini di tempo di calcolo che di spazio di memoria.

Per questa ragione, nella letteratura scientifica si possono trovare diverse tecniche per la semplificazione di modelli dettagliati di combustione. A tal riguardo, le tecniche più note e datate sono certamente l'ipotesi di *stato stazionario* e l'approssimazione dell'*equilibrio parziale*. Tali metodologie, sebbene caratterizzate dal pregio della semplicità, presentano lo svantaggio di un'implementazione non ancora automatica. Di recente, pertanto, sono stati introdotti i metodi di *Intrinsic low Dimensional Manifolds* (ILDM) e *Computational Singular Perturbation* (CSP), al fine di automatizzare la procedura di riduzione dei modelli ed ottenere schemi semplificati più accurati, al costo però di un'implementazione molto articolata.

In questa tesi, il *Metodo delle Griglie Invarianti* (MIG) è elaborato per applicazioni nell'ambito della combustione: ne risulta un algoritmo automatico basato su due punti chiave. Il primo consiste nella rapida costruzione di una sommaria descrizione ridotta del meccanismo chimico. A tal fine, la procedura MIG può essere inizializzata ricorrendo al cosiddetto *manifold*

di quasi equilibrio (QEM), approfonditamente discusso nel corso di questo lavoro. In particolare, in questa tesi introduciamo la versione discreta del QEM fornendone altresì l'algoritmo di costruzione. Tale procedura è convalidata nel caso di meccanismi per l'ossidazione dell'idrogeno, nonché per generare un'approssimazione delle popolazioni di equilibrio nel caso del metodo entropico di lattice Boltzmann.

Il secondo punto chiave della costruzione di un meccanismo ridotto è ugualmente automatico, e consiste nell'affinare l'approssimazione iniziale (e.g. QEM) per iterazioni successive. Qui, vogliamo dimostrare che un modello ridotto accurato può essere ottenuto come punto di convergenza di uno dei seguenti processi: iterazioni di Newton per risolvere la *condizione di invarianza* trattata come un'equazione, oppure il rilassamento della cosiddetta *equazione di film*. Schemi numerici espliciti per l'implementazione di tali tecniche sono riportati e convalidati. Tuttavia, introduciamo anche una realizzazione implicita caratterizzata da una migliore stabilità, nonché dal pregio di illustrare più chiaramente il principio di funzionamento della equazione di film.

Risulta che la costruzione di QEM ed il conseguente affinamento offrono una procedura automatica molto semplice da implementare. Inoltre, sulla base di studi di confronto condotti su modelli semplici, possiamo concludere che le prestazioni del metodo delle griglie invarianti sono perfettamente in linea con quelli ottenuti dal CSP. Tutto ciò ad ulteriore conferma del perfetto accordo ottenuto confrontando le soluzioni dettagliate e ridotte, nel caso di meccanismi per la combustione dell'idrogeno.

Infine, il meccanismo ridotto è impiegato con successo in codici fluidodinamici, basati sul metodo di lattice Boltzmann, per simulare fiamme laminari mono- e bidimensionali attraverso miscele omogenee. Il metodo di lattice Boltzmann (LB) costituisce un approccio nuovo nell'ambito delle simulazioni di fluidodinamica numerica. Studi recenti hanno dimostrato che esso è perfettamente competitivo se confrontato a metodi più tradizionali anche nel caso di flussi compressibili e turbolenti (sia in termini di accuratezza che efficienza di calcolo). D'altro canto, sebbene ciò renda LB una valida alternativa per la simulazione di flussi reattivi, le applicazioni in questo campo sono ancora limitate dal grande numero di variabili da risolvere e dalla rigidezza delle equazioni. In tal senso, tale ultimo studio vuole rappresentare un passo avanti per il metodo di lattice Boltzmann ed è pertanto fra i principali contributi di questa tesi.

Abstract

In the past decades, due to the emergence of stricter environmental regulations, the ability of predicting pollutant formation during combustion processes became of paramount importance. On the other hand, nowadays, numerical simulations of reactive flows represent an indispensable tool in several fields for scientists and designers. Indeed, associated with available experimental data, a numerical simulation proves to be a reliable, cheap and powerful way to study combustion.

Unfortunately, in order to describe pollutant emission, a detailed reaction mechanism with hundreds chemical species has to be considered, whereas a simpler few-step reaction often reveals unsuitable. The prediction of each species involves the solution of one additional transport equation increasing dramatically the computational cost (in terms of calculation time and memory space).

Therefore, several techniques for reducing complex reaction mechanisms have been proposed in the numerical combustion community. The oldest and most known techniques in this respect are certainly the *quasi steady state assumption* and the *partial equilibrium approximation* which present, on one hand the valuable aspect of simplicity, but on the other the drawback to be still hand-powered analytical procedures. Hence, more recently the methods of *Intrinsic Low Dimensional Manifolds* (ILDM) and *Computational Singular Perturbations* (CSP) were introduced in order to automate the process of reduction and provide more accurate simplified mechanisms, yet at the cost of a significant more complicated implementation.

In the present thesis, the *Method of Invariant Grids* (MIG) is elaborated for combustion applications with the aim of automating the model reduction procedure, and its realization follows two key steps. First of all, an initial rough reduced description of the complex chemical mechanism is constructed with no special effort. In this respect, the notion of *quasi equilibrium manifold* (QEM) for initializing the MIG procedure is investigated in great detail. More specifically, here the concept of discrete analog

of QEM is introduced, and a fully automated constructive algorithm is worked out. Validations in the case of hydrogen oxidation mechanisms, and for computing approximate equilibrium populations for the entropic lattice Boltzmann method are presented.

The second key step, for constructing a reduced description of a complex reaction mechanism, is also automated and can be achieved by refinements of the initial approximation. In this work, we demonstrate that the accurate reduced model is obtained as the stable fixed point of one of the following processes: Newton-like iterations for solving the *invariance condition* regarded as an equations, or relaxation due to a *film equation* of dynamics. Explicit numerical schemes for those techniques are discussed and tested. However, an implicit realization, with augmented stability properties, is here introduced, too.

As a matter of fact, constructing a QEM and refining it by means of relaxation methods proves to be an automated procedure with an embarrassingly simple implementation. Furthermore, comparative studies conducted on a simple benchmark model prove that the suggested methodology delivers consistent results with CSP, and it exhibits similar convergence properties. This is in accordance with the excellent agreement between detailed and reduced solutions, in the case of a realistic mechanism for hydrogen combustion.

Lately, the reduced model of the hydrogen mechanism is successfully employed in a lattice Boltzmann code for simulating a 1D propagating flame and 2D laminar counter-flow flames throughout a homogeneous mixture. The lattice Boltzmann (LB) method is a relatively novel approach to numerical flow simulations, and recent studies have proved that it is highly competitive to traditional methods when simulating compressible and turbulent flows (in terms of accuracy and efficiency). Although this makes LB a good candidate for computing reactive flows, applications in this field are still limited by the stiffness of the governing equations and the large amount of fields to solve. In this sense, the latter study intends to be a step ahead for the LB method and a major contribution of this thesis.

List of Figures

Considerate la vostra semenza:
fatti non foste a viver come
bruti, ma per seguir virtute e
canoscenza.

D. Alighieri (1265 - 1321)

1. Introduction

1.1. Motivation

The numerical solution of the full set of governing equations, as dictated by modeling of reactive flows with detailed chemical kinetics, remains a challenging task. The reason is, on one side, the large number of conservation equations to be solved in order to keep track of each chemical species. On the other side, as illustrated in Fig. 1.1, a detailed reaction mechanism contains many different chemical processes occurring on timescales that range over several orders of magnitude, from seconds down to nanoseconds. It is this feature that gives rise to the stiffness of the governing equations for the chemical reactions. Moreover, the fluid mechanics in chemically reactive flows usually occurs at a narrower range on the order of milliseconds to microsecond.

Those aspects have particularly negative impact on the lattice Boltzmann method, whose number of fields (known as distribution functions or populations) is significantly larger than the number of conventional fields (density, momenta, temperature, species mass fractions) by a factor ranging from tens to hundreds for 2D and 3D simulations.

Moreover, the stiffness drastically affects the efficiency of explicit schemes, such as the lattice Boltzmann method, where reducing the time step becomes necessary in order to avoid numerical instabilities. As a result, the smallest time scales need to be resolved even when one is interested only in the slow dynamics. In addition, the larger is the number of elementary reactions involved in the detailed mechanism, the more significant becomes the computational effort due to the evaluation of reaction rates (see section 1.2). These issues make computations of even simple flames time consuming.

On the other hand, some reduction is often possible by simply setting up a criterion for eliminating unimportant reactions (or species) from the detailed reaction mechanism. However, in the present thesis we exploit the

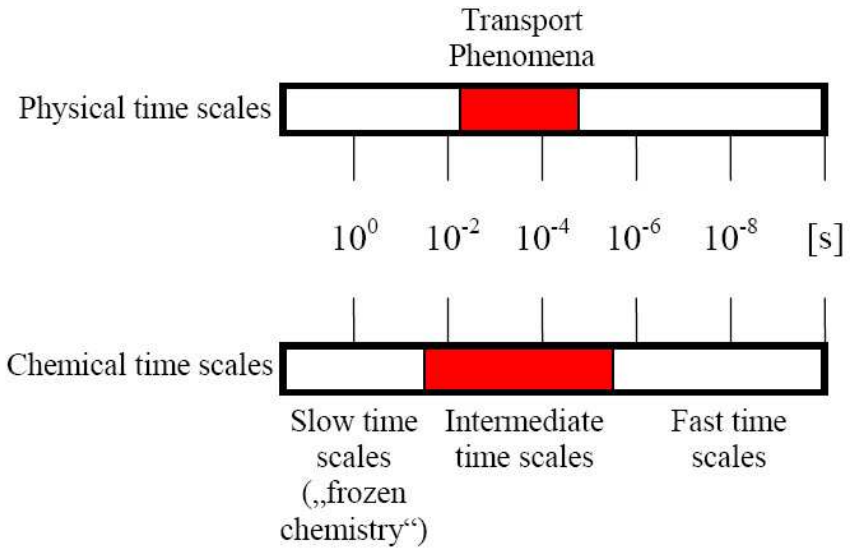

Figure 1.1.: Time scales of physical and chemical processes. (From [67])

more sophisticated concept of timescale separation in order to construct a reduced description of the detailed model. In fact, as mentioned above, there are many chemical processes that are much faster than the fluid dynamic phenomena, so if we are only interested in computing the system behavior on the scale of the fluid mechanics, several chemical processes will have already self-equilibrated. In this case, the reduction techniques can be based on decoupling the fast equilibrating chemical processes from the slower dynamics, and implemented by seeking a *low dimensional manifold* in the solution space of the detailed system.

The idea that a low dimensional manifold provides a reduced description of a complex system stems from the representation of numerical solutions of such systems in the *phase-space* (solution space). To be more precise, let us consider a closed reactive burner with a unique steady state (equilibrium point). The dynamics of such a complex reactive system is often characterized by short initial transients during which the solution trajectories approach low-dimensional manifolds in the concentration space, known as the *slow invariant manifolds* (SIM). The remaining dynamics lasts much longer and evolves along the SIM towards the steady state (see also Fig. 1.4). Thus, it turn out that constructing the SIM enables to establish

a simplified description of a complex system by extracting only the slow dynamics and neglecting the fast. As a result, the detailed large set of equations can be reduced to a much smaller system without a significant loss of accuracy. More details about the notion of SIM are discussed in the chapter 2.

For the sake of completeness, in the next sections we discuss further the concept of model reduction, and briefly review the different approaches that have been suggested in the literature.

1.2. Detailed reaction kinetics

In the following, we focus on homogeneous mixtures of ideal gases reacting in a closed system. Let $x_1, ..., x_n$ be n chemical species participating in a detailed reaction mechanism with r reversible steps

$$\nu'_{s1}x_1 + \ldots + \nu'_{sn}x_n \rightleftharpoons \nu''_{s1}x_1 + \ldots + \nu''_{sn}x_n, \quad s = 1, \ldots, r, \tag{1.1}$$

where ν'_{si} and ν''_{si} are the stoichiometric coefficients of species i in the reaction step s for reactants and products, respectively. Let the stoichiometric vectors be $\boldsymbol{\nu}'_s = (\nu'_{s1}, \ldots, \nu'_{sn})$, $\boldsymbol{\nu}''_s = (\nu''_{s1}, \ldots, \nu''_{sn})$ and $\boldsymbol{\nu}_s$=$\boldsymbol{\nu}''_s$-$\boldsymbol{\nu}'_s$. The reaction rate of step s reads as follows

$$\begin{aligned} &\Omega_s = \Omega_s^+ - \Omega_s^-, \\ &\Omega_s^+ = k_s^+(T) \prod_{i=1}^{n} c_i^{\alpha_i}, \Omega_s^- = k_s^-(T) \prod_{i=1}^{n} c_i^{\beta_i}. \end{aligned} \tag{1.2}$$

Let N_i and V be the mole number of species i and the reactor volume, respectively, the corresponding molar concentration is given by $c_i = N_i/V$. The forward and reverse reaction rate constants k_s^+, k_s^- take the Arrhenius form

$$k_s(T) = A_s T^{\beta_s} \exp\left(\frac{-E_{as}}{\mathcal{R}T}\right), \tag{1.3}$$

where A_s denotes the pre-exponential factor, β_s the temperature exponent, E_{as} the activation energy of reaction s and $\mathcal{R}$ is the universal gas constant. The rate of change of species i is given by

$$\dot{\omega}_i = \sum_{s=1}^{r} \boldsymbol{\nu}_s(i)\,\Omega_s, \quad i = 1, \ldots, n, \tag{1.4}$$

with forward and reverse reaction rate constants related by the equilibrium constant $K_{c,s} = k_s^+ / k_s^-$, which can be obtained by imposing the *principle of detail balance* at the steady state:

$$\Omega_s^+ = \Omega_s^-, \qquad s = 1, ..., r. \tag{1.5}$$

It is worth to stress that, throughout the present thesis, the words *phase-space*, *concentration space* and *composition space* shall be used as synonyms, and if not explicitly mentioned, a generic point of the phase-space will be denoted either by $\boldsymbol{c} = (c_1, \ldots, c_n)$ or by $\boldsymbol{\psi} = (Y_1, \ldots, Y_n)$ according as its coordinates are molar concentrations or mass fractions, respectively.

Notice that an arbitrary state of a homogeneous ideal gas mixture is fully described by the vector $\boldsymbol{c}$ and one independent *intensive* property, e.g. the corresponding temperature T. An alternative description of the system state is also given by $\boldsymbol{\psi}$ and two independent intensive properties, e.g. temperature T and total pressure p.

Under isochoric and isothermal conditions ($V, T = const$), the reaction kinetic equations (1.4) are closed, and the temporal evolution of the species concentrations in the reactor obeys:

$$\frac{d\boldsymbol{c}}{dt} = (\dot{\omega}_1, \ldots, \dot{\omega}_n)^T = \boldsymbol{f}, \tag{1.6}$$

whereas, for different cases, additional closure relations are needed. In this work, other two cases are studied: isolated reactor with constant volume and mixture-averaged internal energy ($V, \bar{U} = const$), and thermal isolated isobaric reactor with constant total pressure and mixture-averaged enthalpy ($p, \bar{h} = const$). In the first case, the governing equations read

$$\begin{aligned} \bar{U} &= \sum_{i=1}^{n} U_i(T)\, Y_i = const \\ \tfrac{d\boldsymbol{c}}{dt} &= (\dot{\omega}_1, \ldots, \dot{\omega}_n)^T = \boldsymbol{f}, \end{aligned} \tag{1.7}$$

where, for each species i, the temperature dependence of the specific internal energy U_i is taken into account by a polynomial fit

$$U_i(T) = \mathcal{R}\left(a_{1i}T + \frac{a_{2i}}{2}T^2 + \frac{a_{3i}}{3}T^3 + \frac{a_{4i}}{4}T^4 + \frac{a_{5i}}{5}T^5 + a_{6i}\right) - \mathcal{R}T. \tag{1.8}$$

Here, following [40], the temperature dependence of all relevant thermodynamic properties of species i are expressed in terms of the constants a_{ji}, with $j = 1, ..., 7$, and each time specified in the text.

Let W_i be the molecular weight of species i, for closed reactors under fixed total pressure and mixture-averaged enthalpy, the dynamics of the mass fractions Y_i obeys the following system of equations

$$\begin{aligned} \bar{h} &= \sum_{i=1}^{n} h_i\left(T\right) Y_i = const, \\ c_i &= \frac{p(Y_i/W_i)}{\mathcal{R}T \sum\limits_{j=1}^{n} Y_j/W_j}, \\ \frac{d\boldsymbol{\psi}}{dt} &= \left(\frac{W_1\dot{\omega}_1}{\bar{\rho}}, \ldots, \frac{W_n\dot{\omega}_n}{\bar{\rho}}\right)^T = \boldsymbol{f}, \end{aligned} \tag{1.9}$$

where the mixture density $\bar{\rho}$ and the specific enthalpy h_i of species i take the explicit form

$$\bar{\rho} = \sum_{i=1}^{n} W_i c_i, \quad h_i\left(T\right) = U_i\left(T\right) + \mathcal{R}T. \tag{1.10}$$

Notice that, for non-isothermal cases, the temperature corresponding to the composition state $\boldsymbol{\psi}$ is not explicitly known. Therefore, the right-hand side of (1.4) can be evaluated after solving the two energy conservation equations in (1.7) and (1.9) with respect to T (e.g. using the Newton-Raphson method).

Finally, in a closed chemically reactive system, the atom mole numbers N_k of each element k must be conserved:

$$\boldsymbol{D}\boldsymbol{\psi}^T = \left(N_1, \ldots, N_d\right)^T, \quad \frac{dN_k}{dt} = 0, \quad \boldsymbol{D}(k,i) = \frac{\mu_{ik}}{W_i}, \tag{1.11}$$

where μ_{ik} is the number of atoms of the kth element in species i, and $\boldsymbol{D}$ is a $(d \times n)$ matrix if d is the number of elements involved in the reaction. In other words, the vector field $\boldsymbol{f}$ of motions in the phase-space is always orthogonal (in Euclidean sense) to the rows of $\boldsymbol{D}$.

The interested reader is delegated to the classical work of Williams [68] for a detailed discussion on the theory of chemical kinetics.

1.3. The problem of reduced description

How do we "reduce the description of a chemical system"? This can be achieved as follows:

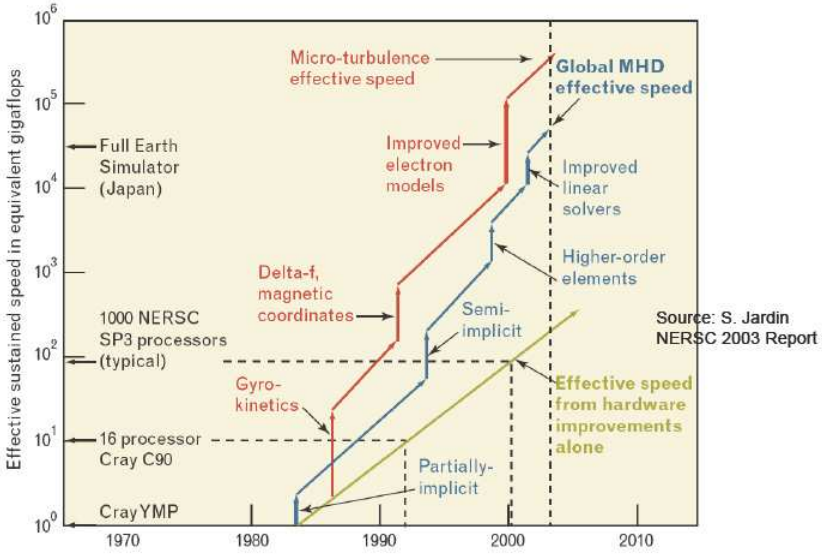

Figure 1.2.: Magneto-hydrodynamic Modeling: computational speedup mainly comes from better algorithms rather than hardware improvements. (From *www.nersc.gov*)

- By shortening the list of species. This, in turn, is accomplished in two ways:

  1. By elimination of unimportant compounds from the list (e.g. low concentration radicals);

  2. By lumping some species into integrated components.

- By shortening the list of reactions. This can be achieved in the following ways:

  1. By elimination of inessential reactions, which have a minor influence in the overall reaction process (using, e.g., the *sensitivity analysis* or the *reaction path analysis* discussed below);

  2. By the assumption that some reactions have been already completed, so that the equilibrium has been reached along their paths. All this leads to a dimension reduction, due to the fact that the equilibrium constants of the completed reactions

are only needed instead of the corresponding reaction rate constants.

- By motion decomposition into fast and slow or, in other words, into independent and slaved according to the corresponding timescales. As a result, the fast dynamics of a complex system can be decoupled from the slow one, and the system admits a study "in parts". Modern approaches to the problem of model reduction in chemical kinetics, based on the motion decomposition, exploit the notion of slow invariant manifold (SIM), and offer the advantage to compute the SIM in an automated manner.

Before proceeding further, we cannot avoid answering the following question: Why do we need to reduce detailed description in the age of supercomputers? First of all, in order to gain a better understanding. In fact, a reduced model often gives the opportunity to extract the essential from a too complicated process. Second, even for supercomputers there exist too demanding problems. Model reduction tries to make such problems less complicated, and sometimes offers us the possibility to solve them.

On the other hand, it is not reasonable to wait and hope that hardware improvements make computers powerful enough to tackle those problems. History has shown, indeed, that the main speedup in numerical computations comes from more efficient algorithms rather than better hardware. For example, in Fig. 1.2, it is possible to distinguish between software and hardware contribution to the overall speedup, in the field of magnetohydrodynamic numerical computations, over the past decades.

Several methods for reducing reaction mechanisms have been worked out in the literature, and recent reviews of such methods can be found in [26, 30, 66].

1.4. Sensitivity analysis

The sensitivity analysis [56, 57] has the scope to identify the major reaction steps that are rate limiting and therefore connot be neglected. Thus, sensitivity analysis reveals to be a useful tool to simplify detailed reaction mechanisms by eliminating unimportant reactions and, often, species that only appears in the negligible reaction steps.

As pointed out in section 1.2, the temporal evolution of a homogeneous in space reactor is described by a system of first order ordinary differential equations, which can be cast in the general form of an initial value problem:

$$\begin{array}{l} \frac{dc_i}{dt} = f_i\left(c_1, \ldots, c_n; k_1^+, \ldots, k_r^+\right), \\ c_i\left(t = t_0\right) = c_i^0, \quad i = 1, \ldots, n, \end{array} \tag{1.12}$$

where c_i^0 is the initial concentration of species i at the time $t = t_0$. The solution of 1.12 depends on both the initial conditions and the parameters (i.e. rate constants, pressure, etc.). Sensitivity analysis aims at quantifying the effect of *small* changes in parameters on the solution trajectory $c_i(t)$. It turns out that a change in the rate constant of most of the elementary reaction steps causes a negligible effect on the solution, meaning that the corresponding rate coefficients do not need to be known with big accuracy. However, for a few reactions, small changes in the rate constants result in large changes of the solution. These important reactions are the *rate-limiting* steps, and there is a need to know their rate constants very accurately.

The dependence of a solution $c_i(t)$ on the rate constants k_s^+ can be taken into account by considering the *absolute* and *relative sensitivities*, defined as follows:

$$S_{i,s}^{abs} = \frac{\partial c_i}{\partial k_s^+}, \qquad S_{i,s}^{rel} = \frac{k_s^+}{c_i}\frac{\partial c_i}{\partial k_s^+} = \frac{\partial \ln c_i}{\partial \ln k_s^+}. \tag{1.13}$$

Except for very simple mechanisms, the derivatives 1.13 can be computed only numerically, when integrating the following system:

$$\begin{array}{l} \frac{\partial}{\partial k_s^+}\left(\frac{dc_i}{dt}\right) = \frac{\partial}{\partial k_s^+} f_i\left(c_1, \ldots, c_n; k_1^+, \ldots, k_r^+\right), \\ \frac{d}{dt}\left(\frac{\partial c_i}{\partial k_r}\right) = \frac{dS_{i,s}^{abs}}{dt} = \frac{\partial f_i}{\partial c_j}\frac{\partial c_j}{\partial k_s^+}, \end{array} \tag{1.14}$$

obtained by differentiating 1.12 with respect to the parameter k_s^+. In the equations 1.14, $\partial f_i/\partial c_j$ is the Jacobian matrix (see the Appendix B), and it is evaluated during the integration of the full system 1.12.

1.5. Reaction path analysis

Similarly to sensitivity analysis, reaction path analysis can be utilized as a tool to eliminate inessential reaction steps and species from a detailed mechanism. In particular, it identifies the major reaction paths, namely the most important reaction steps connecting the reactants to the

final products. The path followed in the transformation from reactants to products is determined by analyzing the contribution of each step to the net rate of production (or depletion) of a given species.

The results of such an analysis are typically shown in the form of graphs, where all the theoretically possible dependencies among reactants and products are presented. It proves convenient, however, to assign thickness to the arrows linking reactants and products so that the most important pathway can be immediately identified. *Integral* reaction path analysis considers the total formation or depletion during combustion. *Atomic flux analysis* follows the rate of each element while transforming from a species to another. Because of element conservation, the sum of all paths into a species must equal the sum of all paths out from it. In Figure 1.3, the flux of carbon is shown in the combustion of a lean mixture of methane and air: here, the dominant path is clearly visible. A reaction step can be considered unimportant when its contribution to the production (or consumption) rates of all species is little (e.g. less than a few percent).

For the sake of completeness, it is worth mentioning that alternative approaches (based on the comparative analysis of entropy production), for estimating the relative importance of elementary steps in a complex reaction network, can be also found in the literature [10, 22].

1.6. Time scale analysis

The wide range of time scales in a reactive flow makes, on one hand more complex the numerical solution, but on the other enables us to approximate the detailed mechanism with a simplified one, that only retains information on the time scale of interest. Among the oldest techniques in this respect, there are the *partial equilibrium approximation* and the *quasi steady state assumption* (QSSA), mathematical procedures that originated early in the twentieth century by the work of Bodenstein and Semenov, and were formalized for combustion systems by Peters [50–52].

In a detailed mechanism, some steps may occur much faster than others, so that they rapidly equilibrate after any perturbation from their equilibrium condition. Therefore, the rate of change of species concentrations is mainly affected by the remaining slower reactions, which can be termed as rate limiting reactions. As illustrated below, using the partial equilibrium assumption, a detailed mechanism can be simplified on the basis of fast and slow reactions.

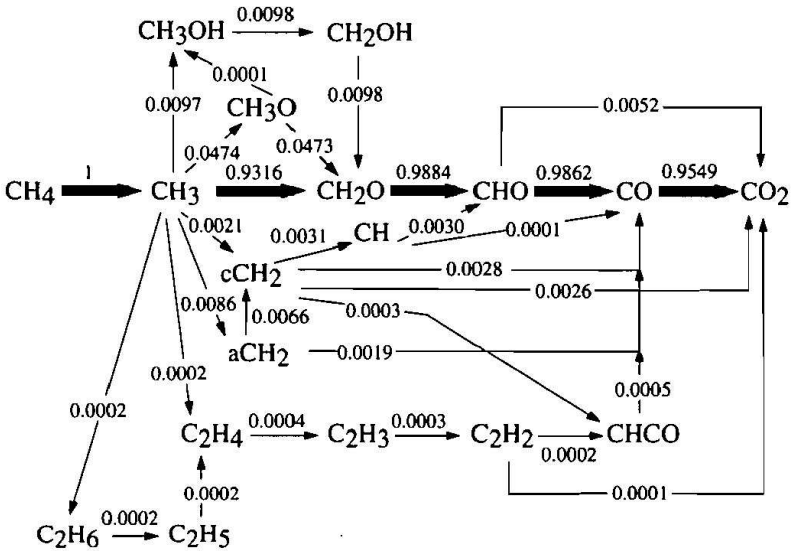

Figure 1.3.: Atomic path of carbon in the combustion of lean ($\phi = 0.5$) CH_4 in a perfectly stirred reactor with a residence time of $5ms$, under a constant pressure of $1bar$ and inlet temperature $T_{in} = 673K$. The detailed mechanism contains 53 species and 488 reactions (From [24]).

the QSSA refers to species rather than reactions. In this case, the steady state species are assumed to reach an almost constant concentration very fast. Thus, by imposing that the rate of change of their concentration vanishes, an algebraic expression (typically non-linear) can be obtained and solved in order to compute the concentration of the steady state species, also known as *QSSA species*.

Illustration: NO formation. The most important reactions responsible for the formation of nitrogen oxide NO, in a typical fuel-air flame at stoichiometric conditions, are listed below and reported along with the corresponding rate constants:

$$\begin{array}{ccccccccc} O & + & N_2 & \rightarrow & NO & + & N, & k_1^+ = 7.6\times10^{13}\exp\left(-38.00/T\right), \\ N & + & NO & \rightarrow & N_2 & + & O, & k_1^- = 1.6\times10^{13}, \\ N & + & O_2 & \rightarrow & NO & + & O, & k_2^+ = 6.4\times10^{9}T\exp\left(-3.15/T\right), \\ NO & + & O & \rightarrow & N & + & O_2, & k_2^- = 1.5\times10^{9}T\exp\left(-19.5/T\right), \\ N & + & OH & \rightarrow & NO & + & H, & k_3^+ = 4.1\times10^{13}, \\ NO & + & H & \rightarrow & N & + & OH, & k_3^- = 2.0\times10^{14}\exp\left(-23.65/T\right). \end{array} \tag{1.15}$$

Thus, the formation rates of NO and N (expressed in terms of molar concentrations c_i) are written as follows:

$$\begin{aligned} \frac{dc_{NO}}{dt} &= k_1^+ c_O c_{N_2} + k_2^+ c_N c_{O_2} + k_3^+ c_N c_{OH} \\ &\quad - \left(k_1^- c_{NO} c_N + k_2^- c_{NO} c_O + k_3^- c_{NO} c_H\right), \end{aligned} \tag{1.16}$$

$$\begin{aligned} \frac{dc_N}{dt} &= k_1^+ c_O c_{N_2} + k_2^- c_{NO} c_O + k_3^- c_{NO} c_H \\ &\quad - \left(k_1^- c_{NO} c_N + k_2^+ c_N c_{O_2} + k_3^+ c_N c_{OH}\right). \end{aligned} \tag{1.17}$$

The QSS assumption can be applied to c_N ($dc_N/dt = 0$), and the resulting expression used to eliminate the variable c_N in the equation 1.16 so that:

$$\frac{dc_{NO}}{dt} = 2k_1^+ c_O c_{N_2} \frac{1 - c_{NO}^2 \big/ \left(\left(k_1^+/k_1^-\right)\left(k_2^+/k_2^-\right) c_{O_2} c_{N_2}\right)}{1 + k_1^- c_{NO} \big/ \left(k_2^+ c_{O_2} + k_3^+ c_{OH}\right)}. \tag{1.18}$$

Although NO is formed both in the reaction zone and in the post-flame gases, the flame thickness is typically very thin and the residence time of the species in the reaction zone is short. Hence, the contribution of the post-flame region to the NO concentration is dominant, and its formation can be decoupled from the concentration of O, O_2, OH, H, N_2 which can be approximated by the corresponding equilibrium values (c_i^{eq}) at the

proper temperature and pressure. In this case, the partial equilibrium approximation for the reactions 1.15 read

$$\begin{aligned} k_1^+ c_O^{eq} c_{N_2}^{eq} - k_1^- c_O^{eq} c_{N_2}^{eq} &= 0, \\ k_2^+ c_N^{eq} c_{O_2}^{eq} - k_2^- c_{NO}^{eq} c_O^{eq} &= 0, \\ k_3^+ c_N^{eq} c_{OH}^{eq} - k_3^- c_{NO}^{eq} c_H^{eq} &= 0, \end{aligned} \tag{1.19}$$

and can be used to eliminate the variables c_O, c_{O_2}, c_{OH}, c_H and c_{N_2} from 1.18 to obtain:

$$\frac{dc_{NO}}{dt} = \frac{2k_1^+ c_O^{eq} c_{N_2}^{eq} \left(1 - (c_{NO}/c_{NO}^{eq})^2\right)}{1 + (c_{NO}/c_{NO}^{eq})\, k_1^+ c_O^{eq} c_{N_2}^{eq} / \left(k_2^+ c_N^{eq} c_{O_2}^{eq} + k_3^+ c_N^{eq} c_{OH}^{eq}\right)}. \tag{1.20}$$

Notice that, these techniques, although relatively simple to implement, involve a considerable *chemist's intuition* to know which species to set in steady state and which reactions in partial equilibrium. Several tools have been developed to aid that process, but they still need external information, hence those methods are certainly far from being fully automated.

On the other hand, the techniques of Intrinsic Low Dimensional Manifold (ILDM) and Computational Singular Perturbation (CSP) are numerical methods that aim at automating the process of mechanism reduction. They offer significant advantages over QSSA and partial equilibrium approximation, but require a considerably more complicated implementation.

The ILDM, introduced by Maas and Pope [47], explicitly computes the low dimensional manifolds approximating the invariant manifold on which the slow chemistry evolves in the phase-space, then the computed results are tabulated for later use in a fluid dynamics code. Referring to Fig. 1.4, for a given closed chemically active system, the thermodynamic equilibrium is a zeroth-dimensional attractor to which all solution trajectories, starting from different (but consistent) initial conditions are ultimately attracted. Based on eigenvalue considerations, ILDM extends this idea to higher-dimensional attractors.

The CSP method, suggested by Lam and Goussis [42], also seeks to reduce the dimensionality via analysis of local eigenvalues. In particular, it identifies basis vectors and classifies them into exhausted modes, active modes and dormant modes. In other words, it systematically looks for the actual reaction pathway of the detailed reaction mechanism. For instance, during the main heat release stage of the combustion of hydrocarbons, reaction steps involving carbon dioxide are active, the initial radical pool

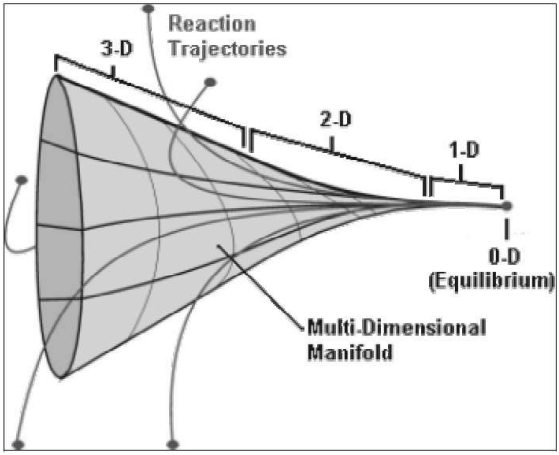

Figure 1.4.: From www.combustion.tue.nl: solution trajectories in composition space and the corresponding manifolds of slow motions.

is exhausted, while reactions related to the production of nitrogen oxide are still dormant. Unlike ILDM, it explicitly provides the reduced mechanism, hence it is more beneficial to a chemist that aims at gaining an understanding of the rate limiting chemistry.

The basic equations of ILDM and CSP are reviewed in chapter 4.

1.7. Outline of the thesis

The thesis is organized in chapters as follows:

- Chapter 1
  - This chapter contains the motivations of the present thesis, along with a basic description of the kinetic equations governing the dynamics of reactive ideal gas mixtures and a brief review of existing model reduction techniques.
- Chapter 2
  - In this chapter, the notions of positively slow invariant manifold, invariance equation, invariant grid and thermodynamic

projector are reviewed. Relevant properties of the thermodynamic projector are discussed and the method of invariant grid (MIG) illustrated in the form of the Newton method with incomplete linearization and relaxation of the film equation of dynamics.

- Chapter 3
  - In this chapter, we give a short introduction to the lattice Boltzmann method (and entropic lattice Boltzmann). In particular, we discuss three popular lattices, $D1Q3$, $D2Q9$, $D3Q15$ and the implementation of boundary conditions as used later on in the thesis.
- Chapter 4
  - Here, a simple test case (Michaelis-Menten mechanism) is considered, and various approximations of the one-dimensional reduced description are constructed and refined using both the Newton method and relaxation method. In particular, the concept of spectral quasi equilibrium manifold is introduced and validated for the studied case. Moreover, the computational singular perturbation method (CSP) is briefly reviewed and implemented. Finally, results from MIG and CSP are compared on the basis of the invariance defect.
- Chapter 5
  - We address here the issue of constructing initial grids when using MIG iterations. In particular, the notion of quasi equilibrium grid is introduced as a discrete analog of a quasi equilibrium manifold, and the corresponding constructive algorithm derived and illustrated by means of examples. More accurate description (compared to the spectral quasi equilibrium grid) of the slow manifold, such as the guided quasi equilibrium grid, are also suggested. Validations are provided considering a simplified mechanism for hydrogen oxidation, under isothermal conditions.
- Chapter 6
  - In this chapter, the method of invariant grid is used for constructing one- and two-dimensional reduced descriptions, in the case of air-hydrogen mixtures reacting under non-isothermal

conditions as dictated by a detailed mechanism. In particular, the spectral quasi equilibrium grid is computed using the algorithm of chapter 5, and refined using the Newton method. The two-dimensional invariant grid is finally tabulated and used during the numerical integration of the reduced system of dynamics. Moreover, the relaxation method for non-isothermal cases is also presented. Finally, a special implementation of the relaxation method, the relaxation redistribution method, is here introduced and validated.

- Chapter 7
  - Methodologies for coupling a reduced description, obtained via MIG, within the lattice Boltzmann framework are now introduced. To this end, we use a reduced description (two degrees of freedom) of a detailed mechanism for reactive mixtures of hydrogen-air. We outline the detailed lattice Boltzmann scheme for simulating reactive flows, and discuss the suggested coupling with reduced chemistry. Validation studies are presented in the case of one-dimensional flame propagating through an adiabatic channel, and two- dimensional counterflow premix flames.
- Chapter 8
  - In this chapter, the thesis conclusions are drawn, and possible future continuations of the present work are suggested.

All our science, measured against reality, is primitive and childlike-and yet it is the most precious thing we have.

A. Einstein (1879 - 1955)

2. Slow invariant manifolds

2.1. Introduction

The idea that dissipative systems of chemical kinetics can have a simplified description, in terms of fast and slow motions, derives from evidences arising when such systems are integrated numerically. In fact, the picture of solution trajectories in the phase-space, that we typically keep in mind, is the following: during the relaxation, from an arbitrary initial condition, a fast motion occurs towards a lower dimension manifold and, once it is reached, the trajectory proceeds slowly along the manifold, towards a steady state (equilibrium point). If such a manifold exists, it is termed the *slow invariant manifold* (SIM), and it can provide a simplification to the original system. In this scenario, a simplified macroscopic description of a complex system can be attained by extracting only the slow dynamics and neglecting the fast one.

2.2. Slow invariant manifold (SIM)

In this section, we introduce the notions of (positively) invariant manifold, slow invariant manifold, invariant grid, and slow invariant grid, for a general system of autonomous ordinary differential equations (ODEs) in a domain $\mathcal{D}$ in $\boldsymbol{R}^n$,

$$\dot{\boldsymbol{c}} = \frac{d\boldsymbol{c}}{dt} = \boldsymbol{f}(\boldsymbol{c}). \tag{2.1}$$

2.2.1. Invariant manifold and invariance equation

A manifold $\boldsymbol{\Omega} \subset \mathcal{D}$ is a *positively invariant manifold* for the system (2.1) if, for any solution $\boldsymbol{c}(t)$, inclusion $\boldsymbol{c}(t_0) \in \boldsymbol{\Omega}$ implies that $\boldsymbol{c}(t) \in \boldsymbol{\Omega}$ for $t > t_0$. Such a set $\boldsymbol{\Omega}$ is named an invariant manifold.

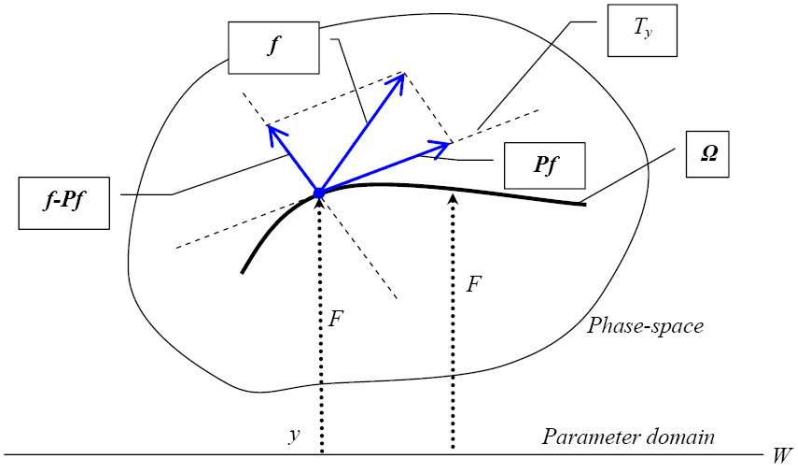

Figure 2.1.: Geometrical structure of model reduction (from [28])

Let the tangent space T_y be defined, for each point $\boldsymbol{c} \in \boldsymbol{\Omega}$. If $\boldsymbol{\Omega}$ is positively invariant under the dynamics of the system (2.1), then the vector $\boldsymbol{f}(\boldsymbol{c})$ belongs to T_y. This provides a necessary differential condition of invariance

$$\boldsymbol{f}(\boldsymbol{c}) \in T_y. \tag{2.2}$$

In order to transform the inclusion condition (2.2) into an equation, we need to execute the following steps:

- to take a complement E_y to T_y in $\boldsymbol{R}^n$,
- to decompose $\boldsymbol{f}(\boldsymbol{c})$ in two components: $\boldsymbol{f}(\boldsymbol{c}) = \boldsymbol{f}_{\parallel}(\boldsymbol{c}) + \boldsymbol{f}_{\perp}(\boldsymbol{c})$, $\boldsymbol{f}_{\parallel}(\boldsymbol{c}) \in T_y$, $\boldsymbol{f}_{\perp}(\boldsymbol{c}) \in E_y$,
- to write down an equation, $\boldsymbol{f}_{\perp}(\boldsymbol{c}) = 0$.

These operations are conveniently described by means of a projector operator. Let for any subspace T_y a projector $\boldsymbol{P}$ on T_y be defined with image $\mathrm{im}(\boldsymbol{P}) = T_y$ and kernel $\ker(\boldsymbol{P}) = E_y$. Then the necessary differential condition of invariance takes the following form

$$\boldsymbol{f} - \boldsymbol{P}\boldsymbol{f} = 0. \tag{2.3}$$

The left-hand side of this equation is important for many constructions and has its own name, the *defect of invariance*: $\Delta = \boldsymbol{f}_{\perp} = \boldsymbol{f} - \boldsymbol{P}\boldsymbol{f}$.

In this *invariance equation* (2.3) an unknown function is the manifold $\mathbf{\Omega}$. This manifold has to be represented in a parametric form, as an immersion $F : \mathcal{W} \to \mathcal{D}$ of a domain $\mathcal{W}$ in the parameter space into the domain $\mathcal{D}$; $\mathbf{\Omega}$ is the image of this immersion: $\mathbf{\Omega} = F(\mathcal{W})$. The tangent space at the point $F(y)$ is the image of the differential of F at the point y. Hence, Eq. (2.3) is a differential equation for F (see Fig. 2.1). The theory of analytic solutions of this equation with analytic vector field $\boldsymbol{f}$ near an equilibrium was developed by Lyapunov [46] (the Lyapunov auxiliary theorem). Applications of this theorem to model reduction were developed recently [38].

Projector $\boldsymbol{P}$ depends on the point $\boldsymbol{c}$ and the space T_y. Invariance equations for different choice of this projector field $\boldsymbol{P}$ are equivalent, the only requirement is $\mathrm{im}(\boldsymbol{P}) = T_y$. But the convergence properties of computational methods significantly depend on the projector choice. The definition of slowness can also be sensitive to this choice.

After defining at any $\boldsymbol{c}$ a positive definite inner product between two arbitrary vectors $\boldsymbol{\eta}_1$ and $\boldsymbol{\eta}_2$, $\langle \boldsymbol{\eta}_1, \boldsymbol{\eta}_2 \rangle$, there is a natural way for constructing a projector $\boldsymbol{P}$. In fact, $\boldsymbol{P}$ can be chosen as $\langle , \rangle$-orthogonal splitting or, in different words, the image and the null space of $\boldsymbol{P}$ are orthogonal with respect to the defined inner product. As reported below, in the case of chemical kinetics, all this leads to the definition of *thermodynamic projector* [27, 31], which corresponds to the following *entropic product* (also known as thermodynamic scalar product):

$$\langle \boldsymbol{\eta}_1, \boldsymbol{\eta}_2 \rangle = \boldsymbol{\eta}_1 \boldsymbol{H} \boldsymbol{\eta}_2^T, \tag{2.4}$$

where $\boldsymbol{H}$ represents the second derivative matrix of a Lyapunov function G with respect to the system (2.1). In a majority of applications, we are looking not for an approximation to an invariant manifold that definitely exists, but rather for an *approximate invariant manifold* with sufficiently small defect of invariance Δ ($\|\Delta\| \ll \|\boldsymbol{f}\|$, for example).

2.2.2. Slow manifold

Reduction of description for dissipative kinetics assumes (explicitly or implicitly) the following picture (Fig. 2.2): There exists a manifold of slow motions $\mathbf{\Omega}_{\mathrm{slow}}$ in the phase-space. From the initial conditions the system goes quickly in a small neighborhood of the manifold, and after that moves slowly along it. The manifold of slow motions (slow manifold, for short)

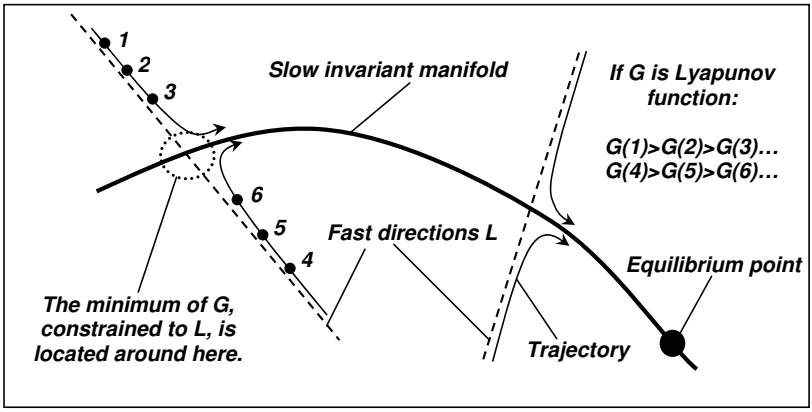

Figure 2.2.: Fast–slow motion decomposition: implications due to the existence of a Lyapunov function G. Several trajectories and correspondent directions of fast motion are presented schematically.

must be positively invariant: if a solution starts on the manifold at t_0, then it stays on the manifold at $t > t_0$. In some neighborhood of the slow manifold the directions of fast motion can be defined. Of course, we always deal not with the invariant slow manifold, but with some approximate slow manifold $\mathbf{\Omega}$. Thermodynamics is useful for model reduction in dissipative systems. The governing idea of these applications is [27]: during the fast motion the entropy (the Lyapunov function G) should increase (decrease), hence, the point of entropy maximum (minimum of G) on the plane of rapid motion is not far from the slow manifold, in the area where fast and slow motion have comparable velocities (Fig. 2.2, inside dashed circles). This implies that *differential of the entropy at points near the slow manifold almost annuls the planes of fast motions* (i.e. entropy gradient is almost orthogonal to these planes). For sufficiently strong fast–slow time separation the fast invariant subspace of the Jacobian matrix $\boldsymbol{J} = [\partial \boldsymbol{f}(i)/\partial c_j]$ near the slow manifold approximates the plane of fast motions, hence, this invariant subspace is also nearly orthogonal to the entropy gradient.

All the definitions of slow manifold for a given system are based on the comparison of motion *to* the manifold with motion *along* the manifold. There should be relatively fast contraction in selected transversal directions (in directions of projector kernel) and relatively slow change of vector field tangent component along manifold. In this work, we don't review

all these approaches (the spectral gap condition, the cone condition, various stability conditions), the details and further references are in Refs. [19, 21, 48, 60, 63].

For our approach, the slow invariant manifold is the *stable fixed point* of one of the following processes:

1. Relaxation due to a film extension of dynamics [28], that is defined by the equation for immersed manifold motion with velocity $\boldsymbol{f}_{\perp}(\boldsymbol{c})$ (*film equation*):
$$\frac{\mathrm{d}F(y)}{\mathrm{d}t} = \boldsymbol{f} - \boldsymbol{P}\boldsymbol{f}; \tag{2.5}$$

2. Iterations of the *Newton method with incomplete linearization* for invariance equation (2.3), that is the Newton process without linearization of $\boldsymbol{P}$: we take $\boldsymbol{f}$ in the first approximation, while for $\boldsymbol{P}$ use the zero one (for details see section 2.3.4 and Ref. [28]).

When the Newton method with incomplete linearization converges, then it leads to slow manifold in the usual sense while the standard Newton method does not. This is very convenient because the standard method is also much more complicated. For sufficiently strong fast-slow time separation, most of the numerous definitions of slow invariant manifold give the same result (exactly the same, or up to higher order terms, it depends on the required regularity of manifolds).

Finally, notice that global existence and uniqueness of slow invariant manifolds, obtained by film equation, have been proven recently for a class of problems [58].

Remark. Fast–slow motion separation in a vicinity of a wandering point[1] is not invariant with respect to smooth or analytical coordinate transformations. In vicinity of attractors (equilibria, closed orbits, or more complicated attractors) Lyapunov exponents exist, they are invariant with respect to smooth coordinate transformation. It is possible to perform invariant fast-slow separation on the base of these exponent values, and then continue the slow manifold to the areas of wandering points, in a spirit of the Lyapunov auxiliary theorem that is proved for a fixed point vicinity. For dissipative systems, most part of phase space consists of wandering points.

[1] $\boldsymbol{c}_0$ is a wandering point of system (2.1) if it has such a vicinity $\mathcal{U}$ that for some $t^* > 0$ any motion $\boldsymbol{c}(t)$ that starts in $\mathcal{U}$ ($\boldsymbol{c}(0) \in \mathcal{U}$) does not return in $\mathcal{U}$ after time t^* ($\boldsymbol{c}(t) \notin \mathcal{U}$ for $t > t^*$).

If we have found an *approximate* slow invariant manifold $\mathbf{\Omega}$, then the corresponding slow *reduced system* is the system on the manifold $\mathbf{\Omega}$ defined by the projected vector field:

$$\dot{\boldsymbol{c}} = \boldsymbol{P}\boldsymbol{f}(\boldsymbol{c}) \tag{2.6}$$

where $\boldsymbol{c} \in \mathbf{\Omega}$ and projector $\boldsymbol{P} : \boldsymbol{R}^n \to T_y$ depends on the point $\boldsymbol{c}$ and on the tangent space T_y, both.

2.2.3. Slow invariant grids

For computational purposes, the discrete analogue of the problem of slow invariant manifold was suggested in Refs. [26, 30].

Let a SIM be defined as an immersion F of the parameter domain $\mathcal{W}$ into $\mathcal{D}$, $F : \mathcal{W} \to \mathcal{D}$. Now we consider a discrete subset $\mathcal{G} \subset \mathcal{W}$. All functions are given on $\mathcal{G}$, and their smooth continuation on $\mathcal{W}$ could be constructed by various approximation techniques. We use notation $F\mid_{\mathcal{G}}$ for restriction a function on the grid. An approximation technique gives a smooth function $F[F\mid_{\mathcal{G}}]$. Let the transformation of discrete set of values into a smooth function,

$$F\mid_{\mathcal{G}} \mapsto F[F\mid_{\mathcal{G}}],$$

be chosen such that, for each $y \in \mathcal{G}$, a *tangent plane* T_y to the discrete set $F\mid_{\mathcal{G}}$ is defined by the differential of $F[F\mid_{\mathcal{G}}]$. We call $F\mid_{\mathcal{G}}$ $(\mathcal{G})$ an *invariant grid*, if it satisfies the grid version of invariance equation:

$$\boldsymbol{f}\left(F\left(y\right)\right) - \boldsymbol{P}\boldsymbol{f}\left(F\left(y\right)\right) = 0 \quad \text{for} \quad y \in \mathcal{G}, \quad \boldsymbol{P} : \boldsymbol{R}^n \to T_y. \tag{2.7}$$

The grid version of the film equation (2.5) is a motion in the defect of invariance direction, and the Newton method with incomplete linearization has the same form as for continuous manifolds (see section 2.3.4). Hence, we can define the *slow invariant grid* as a stable fixed point of (one of) these processes.

2.3. The method of invariant grids

In this section, we outline the MIG for chemical kinetics. For more details see Refs. [26–28, 30].

2.3.1. Thermodynamic potential

If we turn our attention to perfectly stirred closed chemically active mixtures, then dissipative properties of such systems can be characterized with a thermodynamic potential, which is also a Lyapunov function with respect to the kinetic equations. The latter function implements the second law of thermodynamics, and it is related to the mixture-averaged entropy. In other words, during the time relaxation from an initial condition to the steady state, a Lyapunov function $G(\boldsymbol{c})$ must decrease monotonically, thus the steady state $\boldsymbol{c}^{ss} = (c_1^{ss}, ..., c_n^{ss})$ is the point of global minimum of G in the phase space.

In this respect, a simple example is given by the Helmholtz free energy for a perfect gas in a constant volume and under a constant temperature:

$$G = \sum_{i=1}^{n} c_i[\ln(c_i/c_i^{ss}) - 1]. \tag{2.8}$$

Once G is known, the gradient $\boldsymbol{\nabla} G = (\partial G/\partial c_i)$ can be computed, and the second derivatives matrix $\boldsymbol{H} = \left[\partial^2 G/\partial c_i \partial c_j\right]$ enables us to introduce the thermodynamic scalar product according to (2.4) (see also the Appendix A).

2.3.2. Thermodynamic projector

Let us now discuss further the projector $\boldsymbol{P}$ appearing in the condition of invariance (2.3) and the film equation (2.5). Let $\boldsymbol{c}$ be a generic state on a given manifold $\boldsymbol{\Omega}$ (not necessarily invariant), corresponding to the point $y = \left(\xi^1, \ldots, \xi^q\right)$ in the parameter domain $\mathcal{W}$. $\boldsymbol{P}$ can be regarded as a matrix, dependent on $\boldsymbol{c}$, which projects the vector $\boldsymbol{f}(\boldsymbol{c})$ onto the local tangent subspace T_y of $\boldsymbol{\Omega}$ producing, in this way, the induced vector field $\boldsymbol{P}\boldsymbol{f}(\boldsymbol{c})$ (see Fig. 2.1). As mentioned above, only two basic features are requested for constructing a general projector matrix: $\boldsymbol{P}^2 = \boldsymbol{I}$ and the image $\mathrm{im}(\boldsymbol{P}) = T_y$, with $\boldsymbol{I}$ denoting the identity matrix. However, the thermodynamic properties of the kinetic equations define the projector unambiguously [28]. Let us introduce the linear functional, based on the gradient $\boldsymbol{\nabla} G$, and acting on the arbitrary vector $\boldsymbol{\eta}$ as follows:

$$DG(\boldsymbol{\eta}) = \boldsymbol{\nabla} G \boldsymbol{\eta}^T. \tag{2.9}$$

A special class of projectors is the thermodynamic one. Any projector, which belongs to such a class, respects the *dissipation inequality*:

$$DG(\boldsymbol{P}\boldsymbol{f}) \leq 0, \qquad \forall \boldsymbol{c} \in \boldsymbol{\Omega}. \tag{2.10}$$

It has been shown that a projector $\boldsymbol{P}$ respects the (2.10), if and only if [27]:

$$\ker(\boldsymbol{P}) \subseteq \ker(DG), \qquad \forall \boldsymbol{c} \in \boldsymbol{\Omega}, \tag{2.11}$$

where "ker" denotes the null space operator. Below we review the construction the thermodynamic projector, as it will be used in the implementation of MIG. This construction is local since it depends on the concentration point $\boldsymbol{c}$, and on the local tangent space to the manifold $\boldsymbol{\Omega}$.

Let us focus on a grid approximating a q-dimensional SIM. Let $\mathcal{G}$ be a discrete subset of q dimensional parameter space $\boldsymbol{R}^q$ and let $F\mid_{\mathcal{G}}$ be a mapping of $\mathcal{G}$ into the concentration space. Once we select an approximation procedure to restore the smooth map F from the discrete map $F\mid_{\mathcal{G}}$ (for example interpolation by low-order polynomials), the derivatives $\partial F/\partial \xi^i$ can be estimated and, for each grid point y, the tangent space T_y is defined by q independent vectors:

$$\frac{\partial F\,(y)}{\partial \xi^i}, \quad i = 1, ..., q. \tag{2.12}$$

We assume that one of the grid points maps into the steady state, and at other points intersection of manifold with G levels is transversal (i.e. $(DG)_{F(y)}(x) \neq 0$ for some $x \in T_y$). Let us consider the subspace $T_{0y} = T_y \cap \ker(DG)$. In order to define the thermodynamic projector, it proves convenient, if $T_{0y} \neq T_y$, to introduce the vector $\hat{\boldsymbol{u}}_1 \in T_y$ which satisfies the following conditions:

$$\begin{aligned} &\langle \hat{\boldsymbol{u}}_1, \boldsymbol{\eta} \rangle = 0, \quad \forall \boldsymbol{\eta} \in T_{0y}, \\ &DG\,(\hat{\boldsymbol{u}}_1) = 1, \end{aligned}$$

and the vector basis $\{\hat{\boldsymbol{u}}_2, \ldots, \hat{\boldsymbol{u}}_q\}$ of T_{0y} such that $\langle \hat{\boldsymbol{u}}_i, \hat{\boldsymbol{u}}_j \rangle = \delta_{ij}$, with δ_{ij} denoting the Kronecker delta. In the case $T_y \equiv T_{0y}$, let $\{\hat{\boldsymbol{u}}_1, \ldots, \hat{\boldsymbol{u}}_q\}$ be a vector basis of T_y such that $\langle \hat{\boldsymbol{u}}_i, \hat{\boldsymbol{u}}_j \rangle = \delta_{ij}$. The matrix $\boldsymbol{P}$ is a thermodynamic projector, if constructed as follows:

$$\boldsymbol{P} = \boldsymbol{P}_1 + \sum_{k=2}^{q} \boldsymbol{P}_k, \;\; \boldsymbol{P}_1\,(i,j) = \boldsymbol{\nabla} G_j \hat{\boldsymbol{u}}_{1i}, \;\; \boldsymbol{P}_k\,(i,j) = \left(\hat{\boldsymbol{u}}_k \boldsymbol{H}\right)_j \hat{\boldsymbol{u}}_{ki}. \tag{2.13}$$

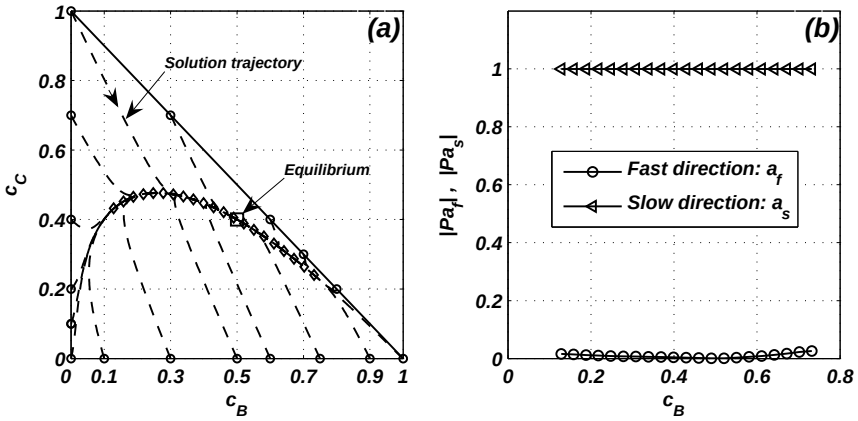

Figure 2.3.: Four-step three-species mechanism. (a) Solution trajectories in the phase space $c_B - c_C$ (dashed lines). Invariant grid (diamonds). (b) Euclidean norm of the thermodynamic projection of Jacobian eigenvectors at the invariant grid nodes.

Remark. A projector $\boldsymbol{P}$ is defined at the points of a smooth q-dimensional manifold $\boldsymbol{\Omega}$. Such a manifold may (or may not) be invariant. Notice that, for constructing a projector $\boldsymbol{P}$ at a given point $\boldsymbol{c} \in \boldsymbol{\Omega}$, the tangent vectors (2.12) are needed. In general, computation of those vectors does not require a global map F: a local one can be safely used for that scope (only derivatives of F at $\boldsymbol{c}$ are requested). In this sense, the invariance defect $\Delta(\boldsymbol{c}) = \boldsymbol{f} - \boldsymbol{P}\boldsymbol{f}$ can be considered a local quantity.

2.3.3. Discussion about grids and thermodynamic projector

For the sake of clarity, in the present section we shall give some more details about the notions of grid and thermodynamic projector. Let $\mathcal{G}$ be a discrete subset of $\boldsymbol{R}^q$. For every point $y \in \mathcal{G}$, a neighborhood of y, $V_y \subset \mathcal{G}$, can be considered. For regular grids, V_y is a finite set of points which, usually includes the nearest neighbors of $y = \left(\xi^1, ..., \xi^q\right)$. The notion of the grid becomes useful for our purposes, if grid differential operators on $\mathcal{G}$ are defined. Indeed, once a discrete mapping $F\mid_{\mathcal{G}}$ of $\mathcal{G}$ into the concentration space is known, there is a need to restore a differentiable map F from it (by approximating, for example, through low-order polynomials) so that

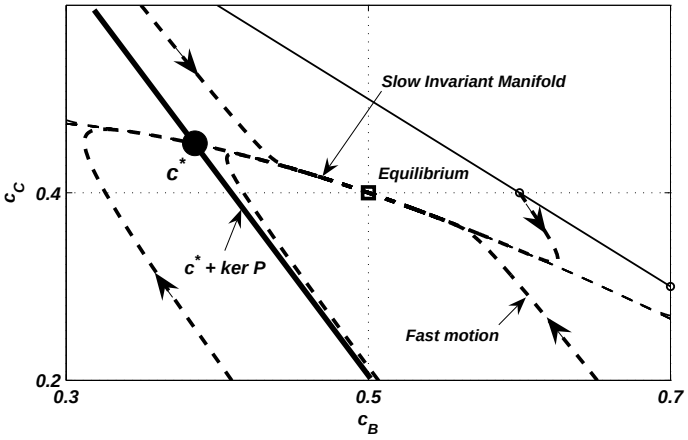

Figure 2.4.: The fast part of any trajectory lies in the null space ($ker\boldsymbol{P}$) of the thermodynamic projector constructed at the invariant grid nodes.

the following derivatives:

$$\left.\frac{\partial F}{\partial \xi^i}\right|_y = \sum_{\zeta \in V_y} g_i\left(y,\zeta\right) F\left(\zeta\right), \quad i = 1, ..., q, \tag{2.14}$$

are available at each point y. Here, $g_i\left(y,\zeta\right)$ are some coefficients and they are dependent on the chosen approximation. In our calculations, we often make use of second-order polynomials. We assume that (2.14) can be evaluated at each point of $\mathcal{G}$. We call such grids admissible and, in the sequel, we only deal with admissible grids. In this way, at any grid point y, the subspace, spanned by the q vectors 2.14, is the local tangent space T_y of the grid. Notice that the definition of a grid includes:

1. A discrete subset $\mathcal{G} \subset \boldsymbol{R}^q$.
2. A discrete mapping of $\mathcal{G}$ into the concentration space.
3. The differentiation formulas (2.14) with given coefficients $g_i\left(y,\zeta\right)$.

Moreover, such a grid is defined invariant (with respect to the equations (2.1)) when, at any point y, the vector field $\boldsymbol{f}\left(F\left(y\right)\right)$ belongs to the tangent space T_y. Here, It is important to stress that the construction of the thermodynamic projector (2.13) can be carried out, at any grid node (and only there), without a need of a global parametrization. Indeed, the

tangent space T_y can be found at any y, via (2.14), by only using a local mapping of $V_y \subset \mathcal{G}$ into the phase space. Let us now discuss some properties of the thermodynamic projector. Those special features make that operator particularly useful for model reduction.

The thermodynamic projector (as well as any other projector appearing in the invariance condition (2.3)) is characterized by its image and null-space. In general, both those linear subspaces are dependent on the grid point y where $\boldsymbol{P}$ is constructed, thus, the thermodynamic projector is an affine projector. By construction, the image of such operators spans the tangent subspace T_y of the grid at y, and that is certainly the case for the thermodynamic projector, too. Nevertheless, the null-space of (2.13) is special. Let the system (2.1) be stiff. We expect that any solution trajectory in the phase space, after a fast initial transient, is attracted to a low-dimensional manifold $\boldsymbol{\Omega}$, and then it slowly move along it, towards the steady state. It is known that a good approximation of fast motions close to a SIM point $\boldsymbol{c}^*$, are given by the eigenvectors of the Jacobian $\boldsymbol{J} = [\partial \boldsymbol{f}(i)/\partial c_j]$ corresponding to eigenvalues with the largest absolute real part (see, e.g., [47]). Let us consider an invariant grid $\mathcal{G}_{inv}$. That grid is a discrete analog of the SIM, and its mapped points $F(y)$ in the phase space are expected to be located close to the SIM. The thermodynamic projector is constructed in such a way that, at any invariant grid node $F(y)$, the null space of (2.13) is "almost" spanned by the fast directions at that point, e.g., the fast eigenvectors of $\boldsymbol{J}\,(F\,(y))$.

In order to illustrate this important feature, we consider the following four-step three-component reaction, considered in a more detail in section 5.4 (kindly suggested by A.N. Gorban):

$$\begin{array}{l} 1.x_A \rightleftharpoons x_B, \quad k_1^+ = 1, \\ 2.x_B \rightleftharpoons x_C, \quad k_2^+ = 1, \\ 3.x_C \rightleftharpoons x_D, \quad k_3^+ = 1, \\ 4.x_A + x_B \rightleftharpoons 2x_C, \quad k_4^+ = 50. \end{array} \tag{2.15}$$

The atom balance has the form:

$$c_A + c_B + c_C = 1, \tag{2.16}$$

and the equilibrium point is chosen such that: $c_A^{ss} = 0.1$, $c_B^{ss} = 0.5$, $c_C^{ss} = 0.4$. Because of the constraint (2.16), the system is effectively two-dimensional. As shown in Fig. 2.3 (a), any solution trajectory, after a rapid initial dynamics, is attracted to a curve and along it reaches the equilibrium point. The system is closed and the reaction (2.15) takes place under

constant volume and temperature, so that here the Lyapunov function is (2.8). An one-dimensional invariant grid, parametrized by the concentration c_B, was considered (diamonds in Fig. 2.3 (a)). At any grid node, the Jacobian matrix $\boldsymbol{J}$ was evaluated. Through spectral decomposition of $\boldsymbol{J}$, it was possible to estimate the fast direction $\boldsymbol{a}_f$ (eigenvector corresponding to the eigenvalue with the largest absolute value) and the slow direction $\boldsymbol{a}_s$ (eigenvector corresponding to the eigenvalue with the smallest absolute value). Both eigenvectors were projected, by means of the thermodynamic projector (2.13), at each node. In Fig. 2.3 (b), the Euclidean norm of those projections $\|\boldsymbol{P}\boldsymbol{a}_i\|$ is plotted versus the grid parameter c_B, and the eigenvectors were chosen such that $\|\boldsymbol{a}_f\| = \|\boldsymbol{a}_s\| = 1$.

Fig. 2.4 shows the geometrical meaning and relevance of the thermodynamic projector to the slow-fast decomposition: the fast component of any trajectory "almost" lies in the affine subspace $\boldsymbol{c}^* + \ker(\boldsymbol{P})$, where $\boldsymbol{c}^*$ is an invariant grid node, while $\ker(\boldsymbol{P})$ is the null space of (2.13) constructed at $\boldsymbol{c}^*$. Notice that, although the thermodynamic projector can be constructed whenever an admissible grid is available, the previous result only applies to invariant grids. Therefore, the model reduction problem is split in two subsequent steps:

1. construction of the slow invariant manifold,
2. reconstruction of the fast subspace.

The thermodynamic projector plays a different role in each of those steps. First, it is used for computing the invariance defect in the iterative procedure of next sections 2.3.4–2.3.5. Second, once the invariant grid (slow subspace) is evaluated, also the fast subspace can be reconstructed via null space of (2.13) at the invariant grid nodes. In this sense, an initial condition of the system (2.1), off the slow invariant grid $\mathcal{G}_{inv}$, can be "projected" onto it along the kernel of thermodynamic projector evaluated on $\mathcal{G}_{inv}$ (see Fig. 2.4).

2.3.4. Newton method with incomplete linearization

When MIG method is applied, not a manifold is searched as a solution, but an admissible grid $\mathcal{G}_{inv}$ whose defect of invariance is sufficiently small. MIG is an iterative procedure, that is, at the beginning, only an initial approximation $\mathcal{G}_0$ is available. In general, $\mathcal{G}_0$ does not respect the invariance condition (2.3) satisfactorily. For this reason the position of $\boldsymbol{c}_0 \in \mathcal{G}_0$ must be refined.

Here, the leading idea is to shift $\boldsymbol{c}_0$, and compute a new node, $\boldsymbol{c}_0+\delta\boldsymbol{c}$, with a smaller defect of invariance: $\boldsymbol{\Delta} = [\boldsymbol{I}-\boldsymbol{P}]\boldsymbol{f}(\boldsymbol{c}_0+\delta\boldsymbol{c})$. If the initial node is "not far" from the invariant manifold, a reasonable way to evaluate the node correction $\delta\boldsymbol{c}$ is given by solving the linearized invariance equation, where the vector field $\boldsymbol{f}$ is expanded to first order and the projector $\boldsymbol{P}$ to zeroth order:

$$[\boldsymbol{I}-\boldsymbol{P}][\boldsymbol{f}(\boldsymbol{c})+\boldsymbol{J}(\boldsymbol{c})\delta\boldsymbol{c}] = 0. \tag{2.17}$$

The Newton method with incomplete linearization consists of the equation (2.17) supplied with the solvability condition [27]:

$$\boldsymbol{P}\delta\boldsymbol{c} = 0. \tag{2.18}$$

The additional condition (2.18) and the atom constraints (1.11) automatically can be taken into account by choosing a basis $\{\boldsymbol{b}_i\}$ in the subspace $\boldsymbol{S} = \ker(\boldsymbol{P}) \cap \ker(\boldsymbol{D})$. Let $\hat{h} = \dim(\boldsymbol{S})$ be the dimension of $\boldsymbol{S}$, the correction can be cast in the form $\delta\boldsymbol{c} = \sum_{i=1}^{\hat{h}} \delta_i \boldsymbol{b}_i$, so that the linearized invariance equation (2.17) becomes the linear algebraic system in terms of δ_i:

$$\sum\nolimits_{i=1}^{\hat{h}} \delta_i \boldsymbol{b}_k \left(\boldsymbol{J}\boldsymbol{b}_i^T - \boldsymbol{P}\boldsymbol{J}\boldsymbol{b}_i^T\right) = \boldsymbol{b}_k \left(\boldsymbol{P}\boldsymbol{f} - \boldsymbol{f}\right), \quad k = 1, ..., \hat{h}. \tag{2.19}$$

Remark. Here, the components of the left-hand side of (2.17), with respect to the basis vectors $\{\boldsymbol{b}_i\}$, are obtained by using the usual inner product. Nevertheless, a different scalar product can be also adopted, without a loss of generality.

In fact, in the case of the thermodynamic projector, it proves convenient to choose the basis $\{\boldsymbol{b}_i\}$ orthonormal with respect to the entropic scalar product (2.4) and write eq. (2.19) as:

$$\sum\nolimits_{i=1}^{\hat{h}} \delta_i \left\langle (\boldsymbol{I}-\boldsymbol{P})\boldsymbol{J}\boldsymbol{b}_i, \boldsymbol{b}_k \right\rangle = -\left\langle (\boldsymbol{I}-\boldsymbol{P})\boldsymbol{f}, \boldsymbol{b}_k \right\rangle, \qquad k = 1, ..., \hat{h}. \tag{2.20}$$

The projector (2.13) is "almost $\langle , \rangle$ −orthogonal", that is,

$$\langle \mathrm{im}(\boldsymbol{P}), \ker(\boldsymbol{P}) \rangle \cong 0, \tag{2.21}$$

close to the SIM. Because of the latter feature, equation (2.20) can be approximated and simplified as follows:

$$\sum\nolimits_{i=1}^{\hat{h}} \delta_i \left\langle \boldsymbol{J}\boldsymbol{b}_i, \boldsymbol{b}_k \right\rangle = -\left\langle \boldsymbol{f}, \boldsymbol{b}_k \right\rangle, \qquad k = 1, ..., \hat{h}. \tag{2.22}$$

Note that, generally the orthogonality condition (2.21) is not exact, and iterations carried out by (2.22) leave a residual invariance defect at the

grid nodes which cannot be completely annihilated. Therefore, when a higher accuracy in the SIM description is required, equation (2.19) is recommended.

2.3.5. Relaxation methods

Alternative approaches, for refining an initial (non invariant) manifold, are based on the relaxation of the film equation (2.5), hence they are named *relaxation methods*. A simple implementation is represented by an explicit first order Euler scheme. Namely, the correction step can be explicitly written at the current grid node $\boldsymbol{c}_0$ as follows:

$$\boldsymbol{c} = \boldsymbol{c}_0 + \delta t \boldsymbol{\Delta}(\boldsymbol{c}_0). \tag{2.23}$$

An estimate of the integration time stepping δt can obtained by imposing that the linearized vector field of (2.17) at the new point $\boldsymbol{c}$ is orthogonal (in the entropic sense) to the invariance defect, at the initial point $\boldsymbol{c}_0$:

$$\langle \boldsymbol{\Delta}, [\boldsymbol{I} - \boldsymbol{P}][\boldsymbol{f}(\boldsymbol{c}_0) + \delta t \boldsymbol{J}\boldsymbol{\Delta}(\boldsymbol{c}_0)] \rangle = 0,$$

and solving with respect to δt:

$$\delta t(\boldsymbol{c}_0) = -\frac{\langle \boldsymbol{\Delta}, \boldsymbol{\Delta} \rangle}{\langle \boldsymbol{\Delta}, \boldsymbol{J}\boldsymbol{\Delta} \rangle}. \tag{2.24}$$

Equations (2.23) and (2.24) adjust the node position acting only along the direction of the invariance defect $\boldsymbol{\Delta}(\boldsymbol{c}_0)$, and typically we expect it to be less efficient compared to the Newton method. On the other hand, this method is particularly easy to implement.

Because of the stiffness of the system (2.1), a first order Euler scheme might request a high number of iterations (2.23). In this case, for numerical integration of the film equation, it proves convenient to treat the vector field $\boldsymbol{f}$ in a semi-implicit manner, according to the scheme suggested in [49] and reviewed below. The film equation (2.5) is discretized as follows:

$$\frac{\boldsymbol{c} - \boldsymbol{c}_0}{\delta t} = \frac{\delta \boldsymbol{c}}{\delta t} = (\boldsymbol{I} - \boldsymbol{P})\, \boldsymbol{f}\,(\boldsymbol{c}) \cong (\boldsymbol{I} - \boldsymbol{P})\, (\boldsymbol{f}\,(\boldsymbol{c}_0) + \boldsymbol{J}\,(\boldsymbol{c}_0)\, \delta \boldsymbol{c})\,,$$

and solved with respect to the correction term $\delta \boldsymbol{c}$:

$$\delta \boldsymbol{c} = \delta t\, (\boldsymbol{f}\,(\boldsymbol{c}_0) + \boldsymbol{J}\,(\boldsymbol{c}_0)\, \delta \boldsymbol{c} - \boldsymbol{P}\boldsymbol{f}\,(\boldsymbol{c}_0) - \boldsymbol{P}\boldsymbol{J}\,(\boldsymbol{c}_0)\, \delta \boldsymbol{c})\,,$$

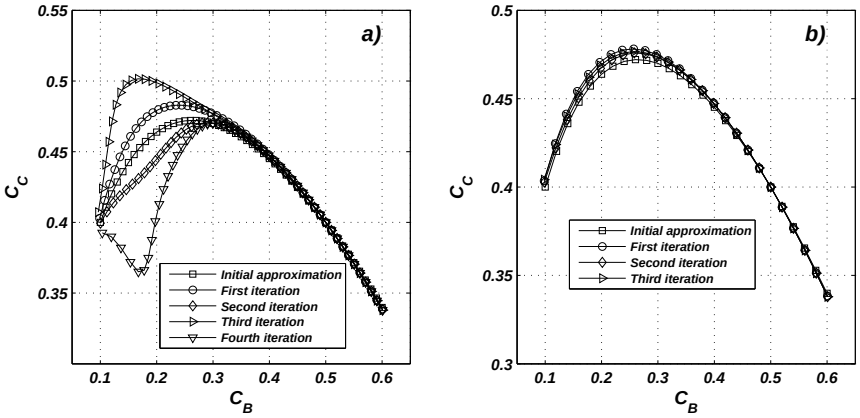

Figure 2.5.: Grid instability. For small grid steps approximations in the calculation of grid derivatives lead to the grid instability effect.

$$\delta \boldsymbol{c} = \delta t \left[\boldsymbol{I} - \delta t \left(\boldsymbol{J}\left(\boldsymbol{c}_0\right) - \boldsymbol{P}\boldsymbol{J}\left(\boldsymbol{c}_0\right) \right) \right]^{-1} \left(\boldsymbol{f}\left(\boldsymbol{c}_0\right) - \boldsymbol{P}\boldsymbol{f}\left(\boldsymbol{c}_0\right) \right). \tag{2.25}$$

Notice that, here the projector $\boldsymbol{P}$ is explicit, thus, as it will be discussed in section 2.3.6, the choice of δt is still restricted by the Courant instability.

Remark. Assume that $\mathcal{G}_{inv}$ is the invariant grid while $\mathcal{G}_0$ is its initial approximation. Let the thermodynamic projector (2.13) be constructed on $\mathcal{G}_0$. After the first iteration (e.g. through (2.19), (2.23) or (2.25)) every node of $\mathcal{G}_0$ is refined so that a new grid $\mathcal{G}_1$ is now available. Note that, in order to continue refining, the projector needs to be constructed on the new grid $\mathcal{G}_1$. In general, at any MIG iteration, the grid is refined, consequently the thermodynamic projector (2.13), also results updated at each iteration.

Finally, the MIG method makes use of the symmetric part (with respect to the entropic product (2.4)) of the Jacobian $\boldsymbol{J}'$, instead of the full matrix $\boldsymbol{J}$, in formulas (2.19), (2.22) and (2.24). The construction of $\boldsymbol{J}'$ is illustrated in the Appendix B.

2.3.6. Instability of fine Grids

When reducing the grid spacing during grid refinement, one can face the problem of the *Courant instability* [20]. Instead of converging, at every iteration the grid becomes more and more entangled.

Let us consider the three-species four-steps mechanism (2.15), where c_B is chosen as reduced variable. By referring to Fig. 2.5 a), in the range $c_B = [0.1, 0.6]$ the grid spacing on the initial approximation is uniformly chosen ($\Delta c_B = 0.01$) and the Newton iterations are not convergent. In Fig. 2.5 b), the grid spacing Δc_B is increased up to 0.02 and the stability recovered.

A way to avoid such instability is well known. This is decreasing the time step. In our problem, instead of a true time step, we have a shift in the Newtonian direction. Formally, we can assign the value $h = 1$ for one complete step in the Newtonian direction. Let us extend now the Newton method to arbitrary h. For this, let us find δ_i from (2.19), but update $\delta \boldsymbol{c}$ proportionally to h. Namely, the correction step is now equal to

$$\boldsymbol{c} = \boldsymbol{c}_0 + h\delta\boldsymbol{c}. \tag{2.26}$$

One way to choose the step value h is to make it adaptive, by controlling the average of the invariance defect $\|\boldsymbol{\Delta}\|$ at every step. Another way is the convergence control: then $\sum h_j$ plays a role of time. Elimination of the Courant instability for the relaxation methods can be done quite analogously. Everywhere the step h is maintained as large as it is possible without running into convergence problems.

3. The lattice Boltzmann method

3.1. Introduction

Traditional computational fluid dynamics (CFD) methods are generally based on the numerical solution of the Navier-Stokes (N-S) equations. In this case, CFD provides with a mathematical description of a fluid as a continuum, and aim at solving the conservation equations of macroscopic quantities (e.g., density, momentum, energy).

On the other hand, the lattice Boltzmann (LB) method is a relatively novel approach to numerical flow simulations, and it can be considered as a special discretization of the Boltzmann equation, which is known to be the governing equation of all fluid flows [64]. The LB method consists of discrete and explicit kinetic equations expressed in terms of the so-called particles distribution functions (populations, for short) and designed in such a way that the N-S equations are recovered in the hydrodynamic limit.

However, the kinetic nature of LB makes it suitable for fluid simulations at a more fundamental level. For instance, applications of LB to the micro-flow regime, where the continuity hypothesis breaks down and the N-S equations (and no-slip boundary conditions) can be no longer utilized, are found in the recent literature [2].

3.2. The lattice Boltzmann equation

In the following, we briefly review the LB algorithm for isothermal flows with the BGK [6] collision model. A single-component medium is described by a small set of populations, which can be regarded as microscopic properties of the fluid. On the contrary, macroscopic quantities such as density and momentum (energy for thermal cases) are given by different moments of those populations.

According to the standard terminology, LB schemes where N particles move on a M-dimensional lattice are referred to as $DMQN$ schemes. In Figures 3.1, 3.2 and 3.3 we show three popular schemes, where each distribution function is represented by its own peculiar velocity $\boldsymbol{e}_\alpha$.

In terms of pressure distribution functions p_α, the LB equation takes the following discrete form:

$$p_\alpha\left(\boldsymbol{x}+\boldsymbol{e}_\alpha, t+\delta t\right)=p_\alpha\left(\boldsymbol{x}, t\right)-\frac{1}{\tau_F}\left[p_\alpha\left(\boldsymbol{x}, t\right)-p_\alpha^{eq}\left(p, \boldsymbol{u}\right)\right], \tag{3.1}$$

and it is implemented by performing subsequently the collision and streaming steps at any lattice node $\boldsymbol{x}$:

- COLLISION

$$\tilde{p}_\alpha\left(\boldsymbol{x}, t\right)=p_\alpha\left(\boldsymbol{x}, t\right)-\frac{1}{\tau_F}\left[p_\alpha\left(\boldsymbol{x}, t\right)-p_\alpha^{eq}\left(p, \boldsymbol{u}\right)\right], \tag{3.2}$$

- STREAMING

$$p_\alpha\left(\boldsymbol{x}+\boldsymbol{e}_\alpha, t+\delta t\right)=\tilde{p}_\alpha\left(\boldsymbol{x}, t\right). \tag{3.3}$$

The equilibrium populations p_α^{eq} take the explicit form

$$p_\alpha^{eq}\left(p, \boldsymbol{u}\right)=w_\alpha p\left[1+3\left(\boldsymbol{e}_\alpha \boldsymbol{u}^T\right)+\frac{9}{2}\left(\boldsymbol{e}_\alpha \boldsymbol{u}^T\right)^2-\frac{3}{2}\boldsymbol{u}^2\right]. \tag{3.4}$$

The pressure p and the fluid velocity $\boldsymbol{u}$ read

$$p=\sum_\alpha p_\alpha, \quad \boldsymbol{u}=\frac{1}{p_0}\sum_\alpha \boldsymbol{e}_\alpha p_\alpha, \tag{3.5}$$

where the reference pressure p_0 is given by $p_0=\rho_0/3$, with ρ_0 denoting the constant reference density of the model in LB units. Let δt be the time step, the relaxation parameter τ_F is related to the kinematic viscosity ν by

$$\nu=\frac{2\tau_F-1}{6}\delta t. \tag{3.6}$$

Here, we make the assumption that all non-zero components of the discrete velocities $\boldsymbol{e}_\alpha$, along the spatial axes (x, y, z) have unity magnitude. In general, the discrete velocities can be regarded as the nodes of a Gauss-Hermite quadrature applied to the Maxwell-Boltzmann distribution function, and each of them is characterized by a proper weight w_α. Below we report the weights for the LB schemes shown in the Figures:

- $D1Q3$

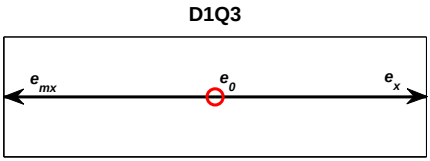

Figure 3.1.: 1-dimensional 3-velocities lattice.

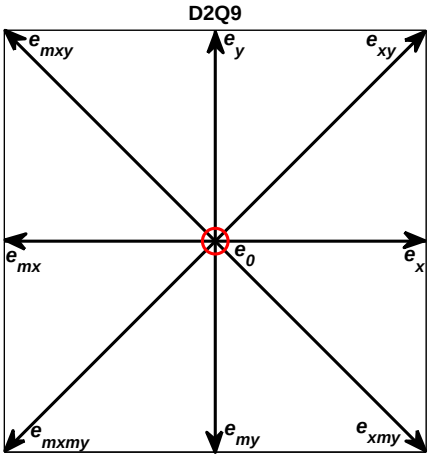

Figure 3.2.: 2-dimensional 9-velocities lattice.

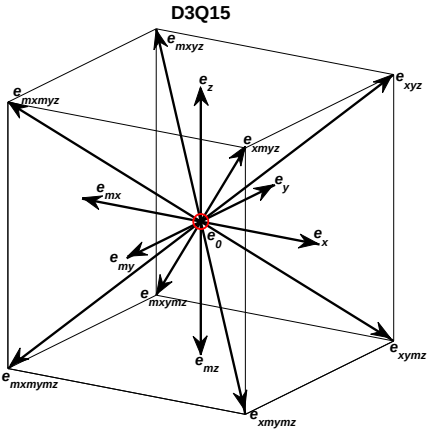

Figure 3.3.: 3-dimensional 15-velocities lattice.

$$w_\alpha = \begin{cases} 2/3, & \|\boldsymbol{e}_\alpha\| = 0, \\ 1/6, & \|\boldsymbol{e}_\alpha\| = 1, \end{cases} \tag{3.7}$$

- *D2Q9*

$$w_\alpha = \begin{cases} 4/9, & \|\boldsymbol{e}_\alpha\| = 0, \\ 1/9, & \|\boldsymbol{e}_\alpha\| = 1, \\ 1/36, & \|\boldsymbol{e}_\alpha\| = \sqrt{2}, \end{cases} \tag{3.8}$$

- *D3Q15*

$$w_\alpha = \begin{cases} 2/9, & \|\boldsymbol{e}_\alpha\| = 0, \\ 1/9, & \|\boldsymbol{e}_\alpha\| = 1, \\ 1/72, & \|\boldsymbol{e}_\alpha\| = \sqrt{3}. \end{cases} \tag{3.9}$$

3.3. Entropic lattice Boltzmann models

The entropic lattice Boltzmann models are a class of LB models, which differs from the classical LB formulation for a special construction of the equilibrium populations. In this case, instead of the discretized Maxwell-Boltzmann distribution function, a discretized form of the $\mathcal{H}$-function is considered, in terms of the density distribution functions f_α, as follows:

$$\mathcal{H} = \sum_\alpha f_\alpha \ln\left(\frac{f_\alpha}{w_\alpha}\right), \tag{3.10}$$

and the equilibrium populations f_α^{eq}, in the isothermal formulation, are regarded as the the minimum of (3.10) under local conserved quantities such as density $\bar{\rho}$ and momentum $\bar{\rho}\boldsymbol{u}$:

$$\begin{array}{ll} \min & \mathcal{H} = \sum_\alpha f_\alpha \ln\left(f_\alpha / w_\alpha\right), \\ s.t. & \sum_\alpha f_\alpha = \bar{\rho},\ \sum_\alpha \boldsymbol{e}_\alpha f_\alpha = \bar{\rho}\boldsymbol{u}. \end{array} \tag{3.11}$$

The entropic formulation is discussed in detail in [1] and [54], where both exact and approximate expressions for f_α^{eq} can be found. It is worth noticing here that, by construction the new populations do not violate the $\mathcal{H}$-theorem, hence the entropic models exhibit augmented stability properties during flow simulations.

3.4. Boundary conditions

Several boundary conditions have been suggested in the literature [12], [64] for simulating the discrete Boltzmann equation. Here, we only focus on the boundary conditions adopted in the sequel of the present thesis.

In order to simulate the interaction between the fluid and a wall, *bounce-back* conditions are used to set zero-slip velocity at a wall node, imposing that any incoming particles on the wall is reversed in the opposite direction. Referring to the notations introduced in Figures 3.1, 3.2 and 3.3 for the particles velocities, the bounce-back conditions can be implemented by logical negation of the populations subscript where, for the x axis, $mx \equiv not\,(x)$ and $x \equiv not\,(mx)$. For instance in the case of $D3Q15$ lattice, if p_{xmymz} is an outgoing population from the wall, the bounce-back condition reads as follows:

$$p_{xmymz} = p_{mxyz}.$$

In order to account for both a wall with no friction and a symmetry plane, different bounce-back conditions are used, where logical negation only applies to the axis orthogonal to the boundary wall. Those conditions are named *reflective bounce-back* (or mirror bounce-back), and can be implemented to the aforementioned population on a wall parallel to the $y-z$ plane as follows:

$$p_{xmymz} = p_{mxmymz}.$$

Moreover, equilibrium populations corresponding to imposed density and velocity can be used at the inlet boundary, whereas extrapolations schemes are generally adopted for simulating fully developed outlet boundary conditions. An examples is discussed in chapter 7.

4. Invariant manifolds for chemical kinetics

4.1. Introduction

In this chapter, we compare various methods aiming at constructing the SIM for a simple yet non-trivial test-case: a two-step four-component catalytic reaction (Michaelis-Menten mechanism). In particular, we deal with three different iterative algorithms:

1. *MIG approach* (based on the Newton method) [26, 28, 30],

2. *MIG approach* (based on the relaxation method) [26, 28, 30],

3. *CSP approach* [33, 42].

Every iterative procedure needs an initial approximation from which it starts a refinement. In general, the quality of this initial step is important for both the convergence towards the solution and for the method efficiency; that is why different initial approximations are considered, too. For our test-case, the following approximations were used:

1. *quasi equilibrium manifold* (QEM), [26, 30]

2. *spectral quasi equilibrium manifold* (SQEM),

3. *intrinsic low dimensional manifold* (ILDM) [9, 47],

4. *symmetric entropic intrinsic low dimensional manifold* (SEILDM) [26, 30].

4.2. Outline of the computational singular perturbation algorithm

The *computational singular perturbation* (CSP) method [33, 42] looks for a decomposition into fast and slow modes of the right-hand side of the system (2.1). If $\boldsymbol{a}_i^f$, $i = 1, \ldots, (n-q)$ are fast and $\boldsymbol{a}_i^s$, $i = 1, \ldots, q$ slow directions (assumed linearly independent), and if the dual basis $\boldsymbol{b}^i$ is fixed by the orthogonality relations,

$$\boldsymbol{b}^i \boldsymbol{a}_j = \delta_{ij}, \quad i, j = 1, ..., n, \tag{4.1}$$

then the vector field of the n-dimensional system (2.1) is written as

$$\boldsymbol{f} = \boldsymbol{A}_f(\boldsymbol{B}^f \boldsymbol{f}) + \boldsymbol{A}_s(\boldsymbol{B}^s \boldsymbol{f}). \tag{4.2}$$

$\boldsymbol{A}_f$, $\boldsymbol{A}_s$ are $n \times (n-q)$ and $n \times q$ column matrices respectively formed by the fast and slow $\boldsymbol{a}_i$ vectors, while $\boldsymbol{B}^f$, $\boldsymbol{B}^s$ are $(n-q)\times n$ and $q \times n$ matrices formed by $\boldsymbol{b}^i$ vectors. Two refinement algorithms are utilized [33, 42]. The first one regards $\boldsymbol{B}^f$:

$$\begin{aligned}
&\boldsymbol{B}^f(k_1+1, m_1) = \boldsymbol{\tau}(k_1, m_1)[\boldsymbol{B}^f(k_1, m_1)\boldsymbol{J} + \dot{\boldsymbol{B}}^f(k_1, m_1)],\\
&\boldsymbol{A}_f(k_1+1, m_1) = \boldsymbol{A}_f(k_1, m_1),\\
&\boldsymbol{B}^s(k_1+1, m_1) = \boldsymbol{B}^s(k_1, m_1),\\
&\boldsymbol{A}_s(k_1+1, m_1) = [\boldsymbol{I} - \boldsymbol{A}_f(k_1+1, m_1)\boldsymbol{B}^f(k_1+1, m_1)]\boldsymbol{A}_s(k_1, m_1),
\end{aligned} \tag{4.3}$$

while the second one is an $\boldsymbol{A}_f$-refinement:

$$\begin{aligned}
&\boldsymbol{B}^f(k_2, m_2+1) = \boldsymbol{B}^f(k_2, m_2),\\
&\boldsymbol{A}_f(k_2, m_2+1) = [\boldsymbol{J}\boldsymbol{A}_f(k_2, m_2) - \dot{\boldsymbol{A}}_f(k_2, m_2)]\boldsymbol{\tau}(k_2, m_2),\\
&\boldsymbol{B}^s(k_2, m_2+1) = \boldsymbol{B}^s(k_2, m_2)[\boldsymbol{I} - \boldsymbol{A}_f(k_2, m_2+1)\boldsymbol{B}^f(k_2, m_2+1)],\\
&\boldsymbol{A}_s(k_2, m_2+1) = \boldsymbol{A}_s(k_2, m_2),
\end{aligned} \tag{4.4}$$

where

$$\begin{aligned}
&\boldsymbol{\tau}(k_i, m_i) = \{[\boldsymbol{B}^f(k_i, m_i)\boldsymbol{J} + \dot{\boldsymbol{B}}^f(k_i, m_i)]\boldsymbol{A}_f(k_i, m_i)\}^{-1},\\
&\dot{\boldsymbol{B}}^f(k_1, m_1) = \sum\nolimits_{i=1}^{n} \frac{\partial \boldsymbol{B}^f(k_1, m_1)}{\partial c_i}\boldsymbol{f}(i),\\
&\dot{\boldsymbol{A}}_f(k_2, m_2) = \sum\nolimits_{i=1}^{n} \frac{\partial \boldsymbol{A}_f(k_2, m_2)}{\partial c_i}\boldsymbol{f}(i).
\end{aligned}$$

After a sufficient number of CSP refinements, the approximate SIM equations and the simplified system are written

$$\boldsymbol{B}^f \boldsymbol{f} = 0, \tag{4.5}$$

$$\dot{\boldsymbol{c}} = \boldsymbol{A}_s(\boldsymbol{B}^s \boldsymbol{f}). \tag{4.6}$$

The two refinement procedures described above are defined *independent* because each index (k or m) can be increased independently. In particular, iterations on k aim at improving the accuracy in the description of the SIM, while it is expected that the other ones make the simplified system (4.6) less and less stiff (cf. Refs. [33, 41, 42]).

Notice that, the orthogonality of the CSP vectors (4.1) always holds. In this chapter we are solely interested in the convergence of (4.5) to the SIM, and do not address the dynamics of the reduced system.

4.3. Initial approximation

4.3.1. Quasi equilibrium manifold

Equations (1.11) define the polytope of all concentration points which satisfy the atom balance constraints. Among those points, we can choose the ones which correspond to the minimum of the Lyapunov function G with respect to the system (2.1): such a set of states gives a manifold known as *quasi equilibrium manifold* (QEM). A QEM attempts to do a motions decomposition in fast - toward the QEM - and slow - along the QEM - inasmuch as G must decrease during the fast motions. In order to be more specific, let us consider a system of n species, it has $(n-d)$ degrees of freedom because of the (1.11). If $q < (n-d)$ is the dimension of the QEM, then the variables of reduced description are $\xi_1, ..., \xi_q$ so that:

$$\boldsymbol{m}_1 \boldsymbol{c}^T = \xi^1, ..., \boldsymbol{m}_q \boldsymbol{c}^T = \xi^q, \tag{4.7}$$

where $\boldsymbol{m}_i$ is a fixed n-dimensional vector. The solution of the variational problem which minimizes G, under constraints (1.11) and (4.7), represents the QEM. The notion of QEM is discussed in detail in chapter 5, and the rationale behind the slow-fast motion decomposition operated by a QEM is illustrated in section 5.9.

4.3.2. Spectral quasi equilibrium manifold

Various QE-manifolds can be obtained choosing different sets of vectors $\{\boldsymbol{m}_1, ..., \boldsymbol{m}_q\}$. On the other hand, a QEM is constructed only on the basis of G and atom balance constraints: therefore considering the eigenvectors of the Jacobian $\boldsymbol{J}$ might be a way to take into account some information about the vector field $\boldsymbol{f}$, as well. To this end, let us discuss further the Jacobian matrix calculated at the steady state $\boldsymbol{J}(\boldsymbol{c}^{ss})$. In general $\boldsymbol{J}$ can be regarded as the sum of $\boldsymbol{J}'$ and $\boldsymbol{J}''$, where the first matrix $\boldsymbol{J}'$ is symmetric with respect to the entropic scalar product (2.4), and respects the following condition: $\boldsymbol{J}'(\boldsymbol{c}^{ss}) = \boldsymbol{J}(\boldsymbol{c}^{ss})$ (see also the Appendix B). If we consider q left eigenvectors of $\boldsymbol{J}(\boldsymbol{c}^{ss})$, which correspond to the q smallest eigenvalues with absolute value (slowest motions), then we construct a special QEM, called *spectral quasi equilibrium manifold* (SQEM).

Same result is obtained by taking $\boldsymbol{m}_i = \boldsymbol{H}\boldsymbol{x}_i^T$, where $\boldsymbol{x}_i$ is one of the q slowest right eigenvector of $\boldsymbol{J}(\boldsymbol{c}^{ss})$, while $\boldsymbol{H}$ is the matrix of second derivatives of the Lyapunov function G at the steady state. Indeed, let $\boldsymbol{y} = \boldsymbol{H}\boldsymbol{x}^T$ be a left eigenvector of $\boldsymbol{J}'(\boldsymbol{c}^{ss})$, then:

$$\boldsymbol{J}'^T(\boldsymbol{c}^{ss})\boldsymbol{H}\boldsymbol{x}^T = \lambda \boldsymbol{H}\boldsymbol{x}^T,$$

where $\boldsymbol{x}$ must be a right eigenvector of matrix $\boldsymbol{H}^{-1}\boldsymbol{J}'^T(\boldsymbol{c}^{ss})\boldsymbol{H} = \boldsymbol{J}(\boldsymbol{c}^{ss})$.

4.3.3. Intrinsic low dimensional manifold

The notion of intrinsic low dimensional manifold (ILDM) (Maas & Pope et al. [47]-[9]) is based on the following separation of eigenvalues of the Jacobi matrix $\boldsymbol{J}$:

$$\begin{aligned} \max\{\mathrm{Re}[\lambda_i], i = 1, ..., (n-q)\} &<< \eta \\ &< \min\{\mathrm{Re}[\lambda_i], i = (n-q+1), ..., n\}, \quad \eta < 0. \end{aligned} \tag{4.8}$$

In that way it is possible to evaluate, at each point, the fast subspace E_y (spanned by eigenvectors which correspond to the first eigenvalues set of (4.8)), and the slow one T_y. Let us define the *transition matrix* $\boldsymbol{Q}$ as a column vectors matrix:

$$\boldsymbol{Q} = (\boldsymbol{v}_1, ..., \boldsymbol{v}_{n-q}, \boldsymbol{v}_{n-q+1}, , ..., \boldsymbol{v}_n), \tag{4.9}$$

where $\boldsymbol{v}_1$-$\boldsymbol{v}_{n-q}$ are the fast eigenvectors of $\boldsymbol{J}$, while $\boldsymbol{v}_{n-q+1}$-$\boldsymbol{v}_n$ the slow ones. If we consider the inverse matrix $\boldsymbol{Q}^{-1}$ as a row vectors matrix:

$$\boldsymbol{Q}^{-1} = \begin{pmatrix} \tilde{\boldsymbol{v}}_1 \\ \cdots \\ \tilde{\boldsymbol{v}}_{n-q} \\ \tilde{\boldsymbol{v}}_{n-q+1} \\ \cdots \\ \tilde{\boldsymbol{v}}_n \end{pmatrix} = \begin{pmatrix} \tilde{\boldsymbol{Q}}_f \\ \tilde{\boldsymbol{Q}}_s \end{pmatrix}, \tag{4.10}$$

with $\tilde{\boldsymbol{Q}}_f$ collecting the first $n-q$ rows of $\boldsymbol{Q}^{-1}$, then the ILDM equation reads:

$$\tilde{\boldsymbol{Q}}_f \boldsymbol{f} = 0. \tag{4.11}$$

It is useful to note that the operator $\tilde{\boldsymbol{Q}}_f$ is nothing but a spectral projector which can be constructed efficiently using, e.g., Schur decomposition [47]-[9]. In the illustrative examples below we shall not use this approach, because all eigenvectors will be evaluated explicitly. It is also worth to compare equations (4.5) and (4.11) and notice their similarity. The ILDM projector $\tilde{\boldsymbol{Q}}_f$ can be considered an approximation of the CSP-projector $\boldsymbol{B}^f$. In that case $\boldsymbol{B}^f$ is a matrix whose rows are the fast left eigenvectors of the Jacobian $\boldsymbol{J}$.

4.3.4. Symmetric entropic intrinsic low dimensional manifold

From a geometrical standpoint, the ILDM approach attempts to provide fast and slow directions approximation on the basis of Jacobian matrix eigenvectors. However, this may become computationally intensive when the phase space has a large dimensions. In order to obtain a considerable simplification, it was suggested [26] to use the spectral decomposition of the symmetrized part of $\boldsymbol{J}$, rather than $\boldsymbol{J}$ itself:

$$\boldsymbol{J}^{sym} = \frac{1}{2}(\boldsymbol{J} + \boldsymbol{H}^{-1}\boldsymbol{J}^T\boldsymbol{H}). \tag{4.12}$$

By definition $\boldsymbol{J}^{sym}$ results symmetric with respect to the entropic scalar product (2.4): the ILDM corresponding to (4.12) is termed *symmetric entropic intrinsic low dimensional manifold* (SEILDM). It is well known that spectral decomposition is much more viable for symmetric operators.

4.4. MIG and CSP method at work: a simple example

In the following, a constant volume and temperature system with three components x_1, x_3, x_4 and one catalyst x_2 will be taken as a test-case. Let us consider the two-step reaction:

$$x_1 + x_2 \rightleftharpoons x_3, \tag{4.13}$$

$$x_3 \rightleftharpoons x_2 + x_4, \tag{4.14}$$

so that the function (2.8) can be utilized as the global thermodynamic potential, while the kinetic equations, in terms of concentrations $\boldsymbol{c} = (c_1, c_2, c_3, c_4)$, take the form:

$$\dot{\boldsymbol{c}} = \boldsymbol{f}(\boldsymbol{c}) = \boldsymbol{\gamma}_1 \Omega_1 + \boldsymbol{\gamma}_2 \Omega_2. \tag{4.15}$$

Here subscripts $_{1,2}$ denote the steps (4.13) and (4.14) respectively, thus stoichiometric vectors and Ω_s functions read:

$$\begin{array}{ll} \boldsymbol{\gamma}_1 = (-1, -1, 1, 0), & \Omega_1 = \Omega_1^+ - \Omega_1^- = k_1^+ c_1 c_2 - k_1^- c_3, \\ \boldsymbol{\gamma}_2 = (0, 1, -1, 1), & \Omega_2 = \Omega_2^+ - \Omega_2^- = k_2^+ c_3 - k_2^- c_2 c_4. \end{array} \tag{4.16}$$

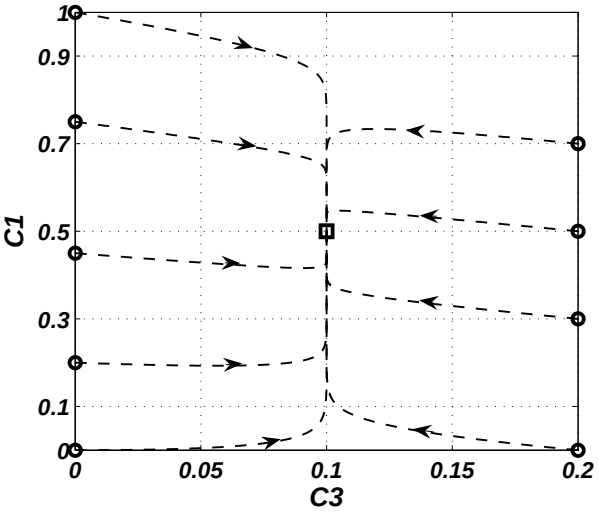

Figure 4.1.: Solutions trajectories with different initial conditions (circles) in $c_1 - c_3$ plane. The square denotes the steady state.

The system (4.15) has a 2×4 conservation law matrix $\boldsymbol{D}$ (from (1.11)):

$$\boldsymbol{D}\boldsymbol{c} = \begin{bmatrix} 1 & 0 & 1 & 1 \\ 0 & 1 & 1 & 0 \end{bmatrix} \begin{bmatrix} c_1 \\ c_2 \\ c_3 \\ c_4 \end{bmatrix} = \begin{bmatrix} const_1 \\ const_2 \end{bmatrix}. \tag{4.17}$$

Hence, the dimension of the phase space is two and we aim at attaining an one-dimensional reduced description. A more extended notation of (4.15) is:

$$\begin{bmatrix} \dot{c}_1 \\ \dot{c}_2 \\ \dot{c}_3 \\ \dot{c}_4 \end{bmatrix} = \begin{bmatrix} \boldsymbol{f}(1) \\ \boldsymbol{f}(2) \\ \boldsymbol{f}(3) \\ \boldsymbol{f}(4) \end{bmatrix} = \begin{bmatrix} k_1^- c_3 - k_1^+ c_1 c_2 \\ k_1^- c_3 - k_1^+ c_1 c_2 + k_2^+ c_3 - k_2^- c_2 c_4 \\ k_1^+ c_1 c_2 - k_1^- c_3 + k_2^- c_2 c_4 - k_2^+ c_3 \\ k_2^+ c_3 - k_2^- c_2 c_4 \end{bmatrix}, \tag{4.18}$$

so in this case the Jacobian matrix takes the explicit form:

$$\boldsymbol{J} = \begin{bmatrix} -k_1^+ c_2 & -k_1^+ c_1 & k_1^- & 0 \\ -k_1^+ c_2 & -k_1^+ c_1 - k_2^- c_4 & k_1^- + k_2^+ & -k_2^- c_2 \\ k_1^+ c_2 & k_1^+ c_1 + k_2^- c_4 & -k_1^- - k_2^+ & k_2^- c_2 \\ 0 & -k_2^- c_4 & k_2^+ & -k_2^- c_2 \end{bmatrix}, \tag{4.19}$$

while the gradient and second derivatives matrix of Lyapunov function G can be written as:

$$\boldsymbol{\nabla} G = \begin{bmatrix} \ln c_1 - \ln c_1^{ss} \\ \ln c_2 - \ln c_2^{ss} \\ \ln c_3 - \ln c_3^{ss} \\ \ln c_4 - \ln c_4^{ss} \end{bmatrix}, \quad \boldsymbol{H} = \begin{bmatrix} 1/c_1 & 0 & 0 & 0 \\ 0 & 1/c_2 & 0 & 0 \\ 0 & 0 & 1/c_3 & 0 \\ 0 & 0 & 0 & 1/c_4 \end{bmatrix}. \tag{4.20}$$

For our calculations the following set of parameters is used:

$$\begin{array}{llll} k_1^+ = 1, & k_1^- = 0.5, & k_2^+ = 0.4, & k_2^- = 1; \\ c_1^{ss} = 0.5, & c_2^{ss} = 0.1, & c_3^{ss} = 0.1, & c_4^{ss} = 0.4, \\ const_1 = 1, & const_2 = 0.2. & & \end{array}$$

The solution trajectories of the system (4.15) are shown in Fig. 4.1. In this case, the SIM is known, and its projection onto $c_1 - c_3$ plane is the line segment $c_3 = c_3^{ss} = 0.1$.

4.4.1. QEM on the example

In order to extract the invariant manifold of Fig. 4.1, we can construct an initial quasi equilibrium manifold with no special effort, and then refine it

using the MIG procedure. In our example $q = 1$ (one-dimensional reduced description). Thus, we need a four dimensional vector $\boldsymbol{m}$ which gives the reduced description variable ξ. It is chosen $\boldsymbol{m} = (1, 0, 0, 0)$, so that the QEM is solution of the following variational problem:

$$\begin{array}{ll} \min & G = \sum_{i=1}^{4} c_i[\ln(c_i/c_i^{ss}) - 1], \\ s.t. & \boldsymbol{m}\boldsymbol{c}^T = \xi, \quad \boldsymbol{D}\boldsymbol{c}^T = (const_1, const_2)^T. \end{array} \tag{4.21}$$

Note that the macroscopic parameter ξ, in this example, is the concentration of the component x_1: $\xi = c_1$. Let $\boldsymbol{c}_0$ be the solution of the problem (4.21), and let ϕ express the dependence of c_3 on c_1: $c_{03} = \phi(\xi)$. The

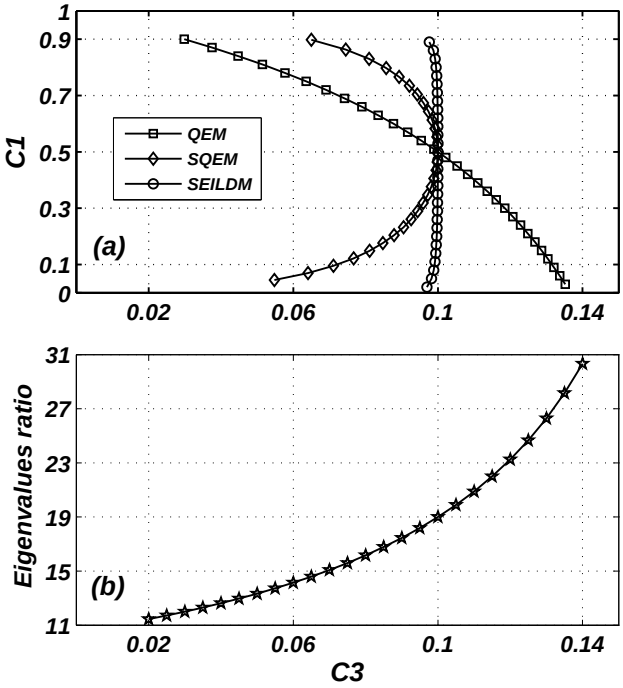

Figure 4.2.: (a) QEM, SQEM and SEILDM as initial approximations of SIM for the system (4.15). (b) Ratio between the second smallest and the smallest (by absolute value) nonzero eigenvalue of the Jacobian: in this case λ^f/λ^s depends only on c_3 (see (4.27)).

problem (4.21) takes the following more explicit form:

$$\begin{array}{l} c_{01} = \xi \\ c_{02} = const_2 - \phi(\xi) \\ c_{03} = \phi(\xi) \\ c_{04} = const_1 - \xi - \phi(\xi) \\ \frac{\partial G(\phi,\xi)}{\partial \phi} = 0, \frac{\partial^2 G(\phi,\xi)}{\partial \phi^2} > 0. \end{array} \tag{4.22}$$

The solution of (4.22) delivers a quadratic expression for $\phi(\xi)$:

$$\phi(\xi) = \Psi(\xi) - \sqrt{\Psi^2(\xi) - const_2(const_1 - \xi)},$$

where $\Psi(\xi) = (const_2(const_1 - c_1^{ss}) + c_3^{ss}(c_1^{ss} + c_3^{ss} - \xi))/(2c_3^{ss})$. The QEM results "quite far" from the invariant manifold (see Fig. 4.2(a)), namely its decomposition of fast and slow motions cannot be considered good, and must be corrected by MIG.

4.4.2. SQEM on the example

We can attempt to have a better accordance between the initial approximation and the SIM, at least in a neighborhood of the equilibrium point. That is what the SQEM aims at when $\boldsymbol{m}$ is taken, *not blindly*, but choosing the slowest left eigenvector $\boldsymbol{x}_l^s$ of matrix (4.19) calculated at $\boldsymbol{c}^{ss}$. In the following, subscripts l and r and superscripts f and s will denote left, right, fast and slow eigenvectors, respectively. Spectral analysis of Jacobian (4.19) at the equilibrium state provides two non-zero eigenvalues:

$$\begin{array}{ll} \lambda^f = -1.9, & \boldsymbol{x}_l^f = (1, 9, -9, 1), \\ \lambda^s = -0.1, & \boldsymbol{x}_l^s = (1, 0, 0, -1.25). \end{array}$$

This time the choice of the reduced description variable is unambiguous ($\boldsymbol{m} = \boldsymbol{x}_l^s \Rightarrow \xi = c_1 - 1.25c_4$), so the problem (4.21) becomes:

$$\begin{array}{l} c_{01} = 1.25\phi(\xi) + \xi \\ c_{02} = const_2 - const_1 + \xi + 2.25\phi(\xi) \\ c_{03} = const_1 - \xi - 2.25\phi(\xi) \\ c_{04} = \phi(\xi) \\ \frac{\partial G(\phi,\xi)}{\partial \phi} = 0, \frac{\partial^2 G(\phi,\xi)}{\partial^2 \phi} > 0, \end{array} \tag{4.23}$$

and the function ϕ for the SQE-manifold reads:

$$\left(\frac{\xi + 1.25\phi}{c_1^{ss}}\right)^{1.25} \left(\frac{c_3^{ss}}{c_2^{ss}} \frac{\xi + 2.25\phi - 0.8}{-\xi - 2.25\phi + 1}\right)^{2.25} \frac{\phi}{c_4^{ss}} - 1 = 0. \tag{4.24}$$

As expected, the SQEM provides a much better SIM approximation close to the steady state $\boldsymbol{c}^{ss}$ (see Fig. 4.2(a)).

4.4.3. ILDM and SEILDM

An easier way to study the system (4.18) is to reduce the dimension from four to two by adding the two conservation laws (4.17). The ODEs system, governing the time evolution of c_3 and c_1, becomes:

$$\begin{aligned} \dot{c}_3 &= c_3^2 - 2.1c_3 + 0.2 \\ \dot{c}_1 &= 0.5c_3 + c_1c_3 - 0.2c_1. \end{aligned} \tag{4.25}$$

Here, the Jacobian matrix takes the simple form:

$$\boldsymbol{J}(c_3, c_1) = \begin{bmatrix} 2c_3 - 2.1 & 0 \\ 0.5 + c_1 & c_3 - 0.2 \end{bmatrix}, \tag{4.26}$$

and the spectral analysis of that operator gives the following eigenvalues:

$$\lambda^f = 2c_3 - 2.1, \qquad \lambda^s = c_3 - 0.2. \tag{4.27}$$

Their ratio, which can be regarded as an estimate of time scales separation, is reported in Fig. 4.2(b) for the domain of the phase space of interest. The right and left eigenvectors are:

$$\boldsymbol{x}_r^f = (c_3 - 1.9, 0.5 + c_1)^T, \qquad \boldsymbol{x}_r^s = (0, 1)^T, \tag{4.28}$$

$$\boldsymbol{x}_l^f = (1, 0), \qquad \boldsymbol{x}_l^s = (0.5 + c_1, 1.9 - c_3). \tag{4.29}$$

According to the procedure described in section 4.3.3, being $(n - q) = 1$, $\boldsymbol{v}_1 = \boldsymbol{x}_r^f$ and $\boldsymbol{v}_2 = \boldsymbol{x}_r^s$, we obtain:

$$\boldsymbol{Q}^{-1} = \frac{1}{c_3 - 1.9} \begin{bmatrix} 1 & 0 \\ -0.5 - c_1 & c_3 - 1.9 \end{bmatrix} \tag{4.30}$$

and one of the solutions of ILDM equation (4.11) for that case ($c_3^2 - 2.1c_3 + 0.2 = 0$) gives exactly the SIM.

Let us consider here the symmetrized part $\boldsymbol{J}^{sym}$ of Jacobian (4.19) calcu-

lated according to (4.12):

$$\boldsymbol{J}^{sym} = \frac{1}{2}\begin{bmatrix} -2k_1^+c_2 & -2k_1^+c_1 & \left(k_1^- + \frac{k_1^+c_1c_2}{c_3}\right) & 0 \\ -2k_1^+c_2 & -2k_1^+c_1 - 2k_2^-c_4 & k_1^- + \frac{(k_1^+c_1+k_2^-c_4)c_2}{c_3} + k_2^+ & -2k_2^-c_2 \\ \left(\frac{k_1^-c_3}{c_1} + k_1^+c_2\right) & \left(k_1^+c_1 + k_2^-c_4 + \frac{(k_1^-+k_2^+)c_3}{c_2}\right) & -2k_1^- - 2k_2^+ & k_2^-c_2 + \frac{k_2^+c_3}{c_4} \\ 0 & -2k_2^-c_4 & \left(\frac{k_2^-c_2c_4}{c_3} + k_2^+\right) & -2k_2^-c_2 \end{bmatrix}. \quad (4.31)$$

Notice that, $\boldsymbol{J}^{sym}$ is symmetric with respect to the entropic scalar product (2.4). The ILDM procedure, carried out with $\boldsymbol{J}^{sym}$ instead of $\boldsymbol{J}$, delivers the SEILDM approximation. The one-dimensional grid in Fig. 4.2(a) was found by solving the equation (4.11), node by node, as described in the following. Let $\boldsymbol{c}^j$ and $\xi(j)$ be a generic node of the SEILDM grid and its correspondent reduced description variable (in our case $\xi = c_1$), respectively. Equation (4.11) takes the form:

$$\boldsymbol{x}_l^f \boldsymbol{f} = 0, \quad (4.32)$$

where $\boldsymbol{x}_l^f$ is the fastest left eigenvector of $\boldsymbol{J}^{sym}(\boldsymbol{c}^j)$. Once the discretization step on the grid ($\Delta\xi$) is defined, the grid node $\boldsymbol{c}^{j\pm1}$ can be evaluated by solving equation (4.32) and imposing that the macroscopic parameter $\xi(j \pm 1) = \xi(j) \pm \Delta\xi$. The latter algorithm, starting from the equilibrium point ($\boldsymbol{c}^1 = \boldsymbol{c}^{ss}$), was performed twice choosing $\Delta\xi = 0.03$: the first time to compute the upper branch of the SEILDM grid, the second time to compute the other one.

4.4.4. MIG iterations

Let us write the thermodynamic projector (2.13) for the case (4.18). Here the tangent subspace T_y is a line spanned by the the vector $\hat{\boldsymbol{u}}_1$. Let $\boldsymbol{u}_1$ be a tangent vector at the kth grid point $\boldsymbol{c}^k$, approximated by second order finite differences as follows:

$$\boldsymbol{u} = \left(c_1^{k+1} - c_1^{k-1}, c_2^{k+1} - c_2^{k-1}, c_3^{k+1} - c_3^{k-1}, c_4^{k+1} - c_4^{k-1}\right). \quad (4.33)$$

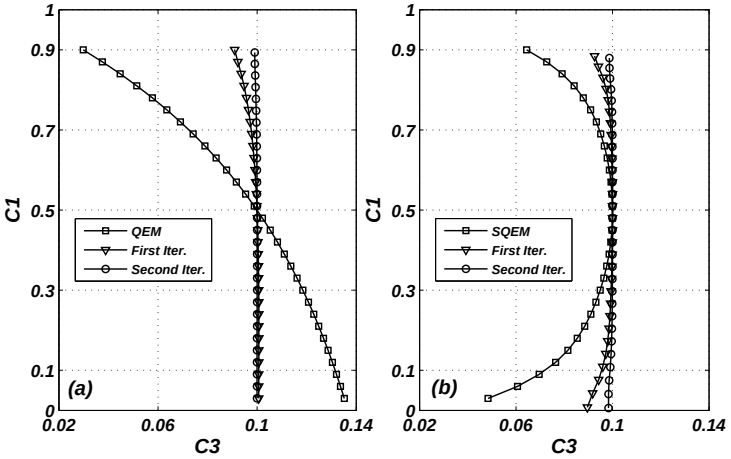

Figure 4.3.: Newton method with incomplete linearization: (a) two iterations starting from the QEM approximation; (b) two iterations starting from the SQEM approximation.

The one-dimensional thermodynamic projector takes the form:

$$\hat{\boldsymbol{u}}_1 = \frac{1}{\boldsymbol{\nabla} G \boldsymbol{u}_1^T} \boldsymbol{u}_1, \quad \boldsymbol{P}(i,j) = \frac{\partial G}{\partial c_j} \hat{u}_{1i}, \tag{4.34}$$

so that the null space of $\boldsymbol{P}$ is the orthogonal (in the usual sense) hyperplane to the gradient $\boldsymbol{\nabla} G$. Let $\boldsymbol{b}_1$ be a vector spanning the one-dimensional space $\ker(\boldsymbol{P}) \cap \ker(\boldsymbol{D})$. When a set of concentration points is available (initial approximation of SIM), at each point $\boldsymbol{c}_0$, the Newton method provides with a correction ($\boldsymbol{c} = \boldsymbol{c}_0 + \delta\boldsymbol{c} : \delta\boldsymbol{c} = \delta_1 \boldsymbol{b}_1$). Here, the system (2.19) is recast into a simple form:

$$\delta_1 = \frac{\boldsymbol{b}_1 \left(\boldsymbol{P}\boldsymbol{f} - \boldsymbol{f} \right)}{\boldsymbol{b}_1 \left(\boldsymbol{J}\boldsymbol{b}_1^T - \boldsymbol{P}\boldsymbol{J}\boldsymbol{b}_1^T \right)}. \tag{4.35}$$

Figures 4.3 (a) and (b) show two initial grids taken on the QEM and SQEM respectively, composed by 30 grid-nodes, whose location is refined using (4.35): results after the first and the second iteration are reported. Those initial grids were also refined by the relaxation method (2.23) and (2.24) where the projector (4.34) is used to calculate the invariance defect. In general, the relaxation method is expected to require a higher number of iterations than the Newton method to achieve a result of comparable accuracy. Nevertheless, this time because of the dimensionality

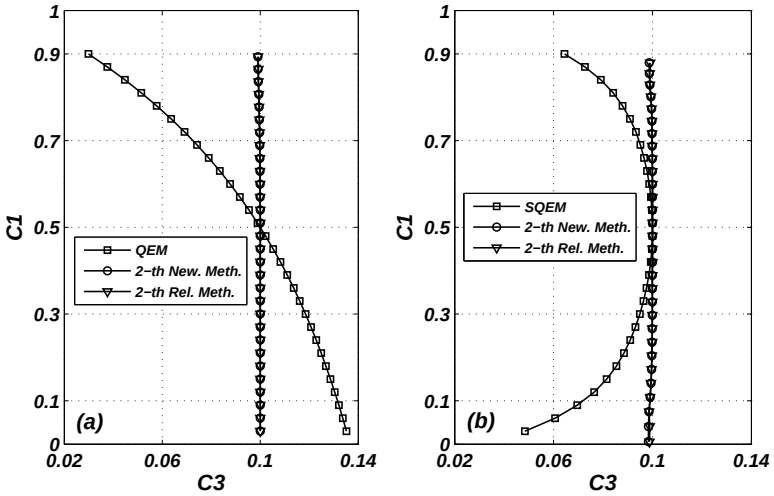

Figure 4.4.: Newton method and relaxation method: (a) two iterations starting from the QEM approximation; (b) two iterations starting from the SQEM approximation.

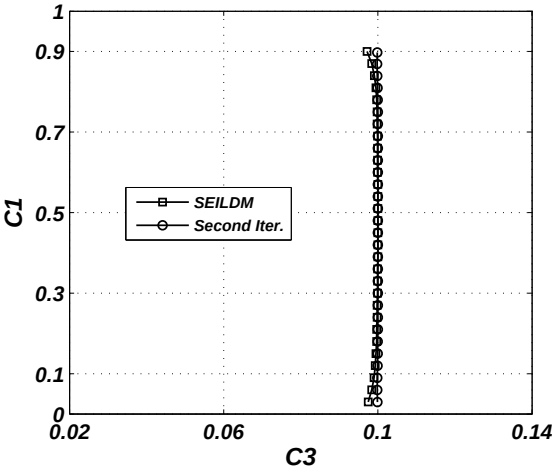

Figure 4.5.: Newton method with incomplete linearization: two iterations starting from the SEILDM approximation.

of the problem the efficiency, as shown by Fig. 4.4, is very similar. Two Newton iterations were also performed starting from the SEILDM, here approximated by 30 nodes (see Fig. 4.5).

4.4.5. Comparison

It is here instructive to compare the efficiency of the methods described above, by introducing procedures able to estimate the "distance" of the refined grid, at each iteration, from the invariant one. This was achieved utilizing two procedures. The first is based on the normalized Hausdorff distance (see also [32]) between two sets of points, while the second one on the Euclidean norm of the invariance defect array. In particular, let $\mathcal{X}, \mathcal{Y}$ be the current set of grid points and the fully refined one, if $d(\boldsymbol{x}, \boldsymbol{y})$ denotes the standard Euclidean metric between two points, by definition the Hausdorff distance between $\mathcal{X}$ and $\mathcal{Y}$ is:

$$\delta_H = \frac{d_H}{D_H} 100\%, \tag{4.36}$$

where

$$\begin{aligned} d_H &= \max \left\{ \max_{\boldsymbol{x} \in \mathcal{X}} \min_{\boldsymbol{y} \in \mathcal{Y}} d(\boldsymbol{x}, \boldsymbol{y}), \max_{\boldsymbol{y} \in \mathcal{Y}} \min_{\boldsymbol{x} \in \hat{X}} d(\boldsymbol{x}, \boldsymbol{y}) \right\} \\ D_H &= \max_{\boldsymbol{x}, \boldsymbol{y} \in \mathcal{X} \cup \mathcal{Y}} d(\boldsymbol{x}, \boldsymbol{y}). \end{aligned} \tag{4.37}$$

Another way to evaluate the accuracy of an invariant grid can be obtained considering the Euclidean norm of an array collecting, at each grid point, the following measure of the invariance defect: $\sqrt{(\boldsymbol{\Delta}^T \boldsymbol{\Delta})/(\boldsymbol{f}^T \boldsymbol{f})}$. In the continuation, the latter quantity will be referred as to *Error*. The comparison between the two Figures 4.6(a) and 4.6(b) shows that both those methods give compatible results. Here, we also observe that if two initial grids are considered, the less accurate one (e.g. in terms of Hausdorff distance) might convergence faster (see QEM vs SQEM in Fig. 4.6). However, as a general rule, a closer initial grid to the invariant manifold gives better guarantees for the convergence of equations (2.19) and (2.23).

It is worth noting that all the grids found above (first approximation and refined ones) respect the thermodynamic requirement: in fact, if they are traced from any point toward the steady state, the entropy $(-G)$ increases (Fig. 4.7), thereby confirming the thermodynamic consistency of the projector (4.34).

Fig. 4.7 also provides the geometrical interpretation of a quasi equilibrium manifold: the tangent spaces to entropy level-curves, at the intersection points with the QEM, have constant inclination. The latter idea can be exploited for constructing grid-based approximations of such manifolds, and it will be illustrated in more detail in chapter 5.

4.4.6. CSP refinements

Also the refinement algorithms (4.3)-(4.4) were used to extract the SIM. This time we need to choose a set of vectors as initial approximation ($\boldsymbol{B}^{f,s}(0,0)$ and $\boldsymbol{A}_{f,s}(0,0)$ matrices). For the system (4.25), the follow-

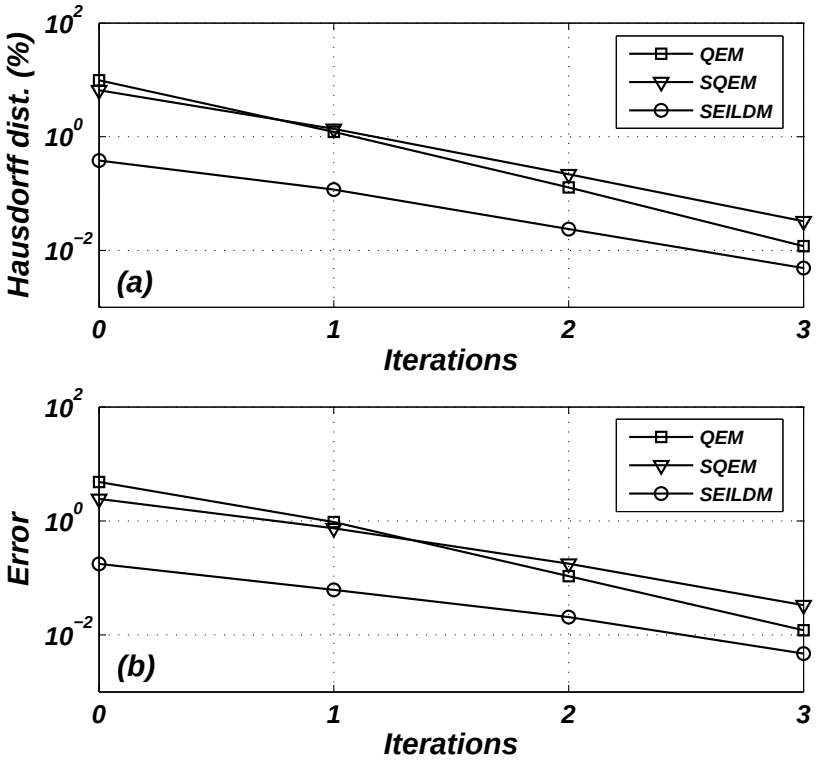

Figure 4.6.: Newton method: (a) Hausdorff distance between refined grid and the invariant one; (b) refined grid Error.

ing vectors were chosen at the step $(k = 0, m = 0)$:

$$\boldsymbol{A}_f(0,0) = \left(\frac{\sqrt{2}}{2}, \frac{\sqrt{2}}{2}\right)^T, \qquad \boldsymbol{A}_s(0,0) = \left(-\frac{\sqrt{2}}{2}, \frac{\sqrt{2}}{2}\right)^T, \tag{4.38}$$

$$\boldsymbol{B}^f(0,0) = \left(\frac{\sqrt{2}}{2}, \frac{\sqrt{2}}{2}\right), \qquad \boldsymbol{B}^s(0,0) = \left(-\frac{\sqrt{2}}{2}, \frac{\sqrt{2}}{2}\right). \tag{4.39}$$

In order to save notation, it proves convenient to introduce the functions:

$$\begin{aligned}
&\mathcal{U} = -3c_3^2 + 0.9c_3 - 4c_3c_1 + 1.5c_1 - c_1^2 + 0.54,\\
&\mathcal{V} = 5c_3^2 - 7.3c_3 + 3c_3c_1 - 2.3c_1 + 3.3,\\
&\mathcal{Z} = 6c_3^2 - 9.9c_3 + 2c_3c_1 - 2.1c_1 + 3.78,\\
&\mathcal{M} = 1.7c_3^2 - 2.62c_3 + 1.7c_3c_1 - 0.16c_1 + 0.24,\\
&\mathcal{T} = 3c_3 + c_1 - 1.8.
\end{aligned}$$

Then the $\boldsymbol{B}^f$-$\boldsymbol{A}_f$-refinements can be written (see (4.3)-(4.4)):

$$\begin{aligned}
&\boldsymbol{A}_f(1,1) = \frac{1}{\sqrt{2}}\left(\frac{\mathcal{Z}}{\mathcal{V}}, -\frac{\mathcal{U}}{\mathcal{V}}\right)^T,\\
&\boldsymbol{A}_s(1,1) = \sqrt{2}\left(\frac{0.2 - c_3}{\mathcal{T}}, \frac{2c_3 + c_1 - 1.6}{\mathcal{T}}\right)^T,
\end{aligned}$$

$$\begin{aligned}
&\boldsymbol{B}^f(1,1) = \sqrt{2}\left(\frac{2c_3 + c_1 - 1.6}{\mathcal{T}}, \frac{c_3 - 0.2}{\mathcal{T}}\right),\\
&\boldsymbol{B}^s(1,1) = \frac{1}{\sqrt{2}}\left(\frac{\mathcal{U}}{\mathcal{V}}, \frac{\mathcal{Z}}{\mathcal{V}}\right),
\end{aligned}$$

$$\begin{aligned}
&\dot{\boldsymbol{B}}^f(0,0) = \dot{\boldsymbol{A}}_f(0,0) = \dot{\boldsymbol{A}}_f(1,0) = \boldsymbol{0},\\
&\dot{\boldsymbol{B}}^f(1,0) = \dot{\boldsymbol{B}}^f(1,1) = \sqrt{2}\left(\frac{\mathcal{M}}{\mathcal{T}^2}, -\frac{\mathcal{M}}{\mathcal{T}^2}\right).
\end{aligned} \tag{4.40}$$

The approximate SIM is found from equation (4.5) which takes, at the step $(1,0)$, the form:

$$2c_3^3 - 5.3c_3^2 + 2c_3^2c_1 - 2.5c_3c_1 + 3.66c_3 + 0.24c_1 - 0.32 = 0. \tag{4.41}$$

Equation (4.41) provides three solutions and Fig. 4.8 reports only the relevant root (only one root is positive and real, and respects the balance

condition (1.11)). Moreover, the manifolds associated with the vectors $\boldsymbol{B}^f(0,0)$ and $\boldsymbol{B}^f(2,1)$ are also shown. Referring to the latter manifold, we want to stress that now equation (4.5) gives one physically acceptable root among seven possible.

Here the initial approximation coincides with the QEM, so it can be useful to compare MIG results with CSP ones on the basis of the Error (see Fig. 4.9). The derivatives (4.40) show that the CSP procedure can become computationally intensive in few iterations even for a very simple example. Finally it is worth to comment Fig. 4.9 (b): since every $\boldsymbol{A}_f$ iteration does not increase the accuracy of $\boldsymbol{B}^f$ vectors, the manifold, after the step $(1,1)$, remains not refined.

4.5. Conclusion

In this chapter, the method of invariant grids is utilized for reducing the kinetics of a simple two-dimensional system in order to obtain an one-dimensional description. Different initial approximations have been calculated and refined. It has been shown that the rate of convergence depends also, but not only, on the accuracy (distance from the invariant manifold) of initial approximations. Moreover, the SQEM proves to be a convenient (for convergence) way to initialize the MIG method: it is particularly accurate nearby the steady state. In general, we found that the QEM construction is a very promising procedure to choose the initial manifold, and its efficient construction, in a larger dimension, will be addressed in chapter 5. As expected, the SEILDM approximation provides a manifold very close to the SIM without facing the full Jacobian matrix (ILDM), but considering its symmetrized part. It was shown that the Newton method and the relaxation methods give, when an one-dimensional invariant grid is searched, comparable results. Nevertheless, in a general case, the Newton method is expected to be more efficient, whereas the relaxation methods require a lesser computational load. The CSP algorithm is utilized too and, although that method and MIG are based on completely different approaches, the comparison shows very similar results in terms of accuracy of SIM description and convergence.

Here, we focused on the geometry of the model reduction, that is, construction of slow invariant manifolds (grids). Dynamic equations of the reduced system using the grid approach will be studied in the next chapters.

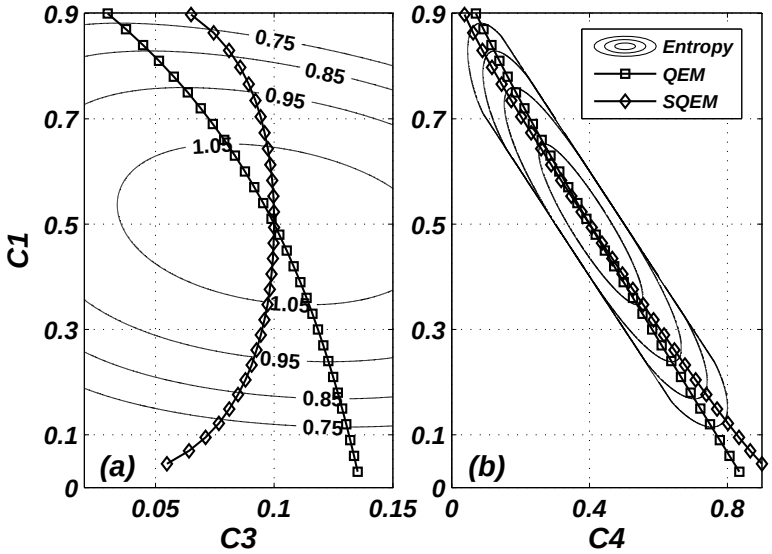

Figure 4.7.: Entropy (-G) level curves: (a) QEM and SQEM in $c_3 - c_1$ plane; (b) QEM and SQEM in $c_4 - c_1$ plane.

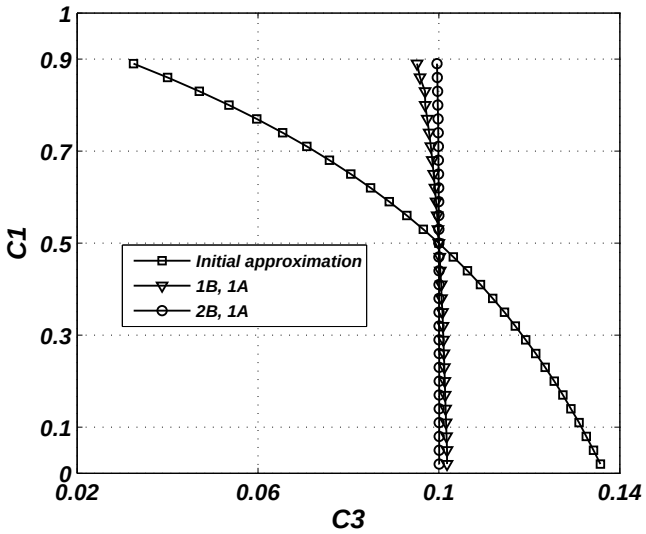

Figure 4.8.: CSP refinement procedure.

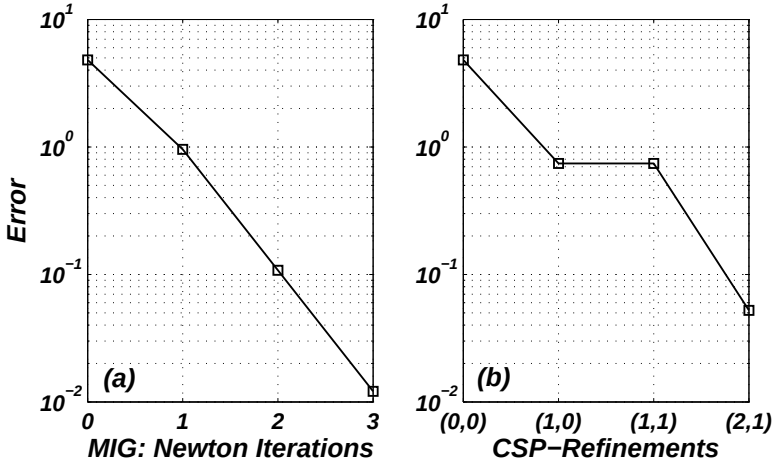

Figure 4.9.: Error evolution during the iterations for (a) MIG and (b) CSP methods starting from the QEM approximation.

5. Quasi equilibrium grids

5.1. Introduction

The definition of a convex Lyapunov function G (whenever a complex system supports such a function) proves to be helpful in model reduction [27, 28]. This is, in particular, the case of chemical reactions in a closed system addressed below. Indeed, it was shown that through a G function accurate approximations of the SIM can be found, for instance by constructing the spectral quasi equilibrium manifold - SQEM - or the symmetric entropic intrinsic low dimensional manifold - SEILDM (see chapter 4), and refined by efficient MIG iterations.

Moreover, the notion of QEM is also useful in different fields. For instance, it can be used for evaluating equilibrium populations in the entropic lattice Boltzmann method [3, 37]. Construction of a QEM is addressed by minimizing G under linear constraints, hence the *Lagrange multipliers method* may be adopted. However, in the following the Lagrange multipliers method is not discussed, and the interested reader can find details about it e.g. in the classical work of Rockafellar [61]. On the contrary, the notion of quasi equilibrium grid (QEG) is introduced, as a discrete analog of QEM, and a constructive algorithm is suggested.

The present chapter is organized as follows. In section 5.2, the QEM definition and its geometrical interpretation are reviewed, while in section 5.3 the one-dimensional quasi equilibrium grid algorithm is presented, and illustrated by means of an example in section 5.4. The extension of that algorithm to multi-dimensional grids is developed in section 5.5. Two possible extension strategies are analyzed: the *straightforward extension* (section 5.5.1) and, following the general idea given in [30], the *flag extension* (section 5.5.2). The notions of *Guided-QEG* and *Symmetric Entropic Guided-QEG* are introduced in section 5.5.3. Further details about the construction of a quasi equilibrium grid are given in section 5.6. An illustrative example, in section 5.7, shows how those extension techniques

work in practice. In order to find out how accurate is their SIM description, they are also compared on the basis of the invariance defect (section 5.7.3). Finally, results are summarized in section 5.10.

5.2. Quasi equilibrium manifold

Any iterative procedure, such as MIG, needs to be supplied with an initial approximation, which plays an important role for both convergence and efficiency. Therefore, the initial approximation must be carefully chosen, and a reasonable way for initializing the MIG, is given by quasi equilibrium manifolds (QEM) (see chapter 4). For the sake of clarity, in the following, we discuss further the notion of QEM introduced in section 4.3.1.

5.2.1. QEM definition

All solution trajectories move orthogonal to the rows of matrix $\boldsymbol{D}$, in order to satisfy the set of atom balances (1.11). Let us consider q additional linear constraints. Among all the states that fulfill the full set of constraints (atom balances + extra constraint), we can choose those points which also minimize the Lyapunov function G of the system we are dealing with. Such points lie on a manifold that is called the quasi equilibrium manifold (QEM).

Let the ODEs system (2.1) be stiff. In other words, we assume that the Jacobi matrix has eigenvalues with different orders of magnitude. In this case, we expect that a solution trajectory in the phase space, after a short transient, reaches a low-dimensional surface (slow invariant manifold), since the fast motions are exhausted and they restrain the solution on that surface. If the slow invariant manifold exists, the QEM can be taken as a reasonable approximation of it. In the case of a chemical system with n reactive species, the degrees of freedom are $(n-d)$ due to the atom balances (1.11). If $q < (n-d)$ is the dimension of the QEM, then the variables for its macroscopic description are $(\xi^1, ..., \xi^q)$ so that: $\boldsymbol{m}_1\boldsymbol{c}^T = \xi^1, ..., \boldsymbol{m}_q\boldsymbol{c}^T = \xi^q$. From a mathematical standpoint, the solution of a variational problem:

$$\begin{array}{ll} min & G \\ s.t. & \boldsymbol{D}\boldsymbol{c}^T = \boldsymbol{const}, \quad \boldsymbol{m}_i\boldsymbol{c}^T = \xi^i, \quad \forall i = 1, ..., q, \end{array} \tag{5.1}$$

represents the QEM corresponding to the vector set $\{\boldsymbol{m}_i\}$. Here, we want to stress that there is no general recipe for choosing the set $\{\boldsymbol{m}_i\}$. Nevertheless, in this thesis we work out some suggestions (see, e.g., the SQEG below or the GQEG construction in section 5.5.3). Similarly, the dimension q is considered an input for the problem (5.1).

The geometrical interpretation of a QEM is illustrated in Fig. 5.1 for a two dimensional phase space (c_{A_i}, c_{A_j}). Let us consider the points where G level curves (convex curves in Figures 5.1 (a)-(b)) are cut by the QE-manifolds (bold curves): at those points the inclination of the tangent space to the G-level curves (dashed lines) remains constant. Different QEM can be obtained by choosing different vector sets $\{\boldsymbol{m}_i\}$.

In particular, as discussed in section 4.3.2, the spectral quasi equilibrium manifold is constructed when $\{\boldsymbol{m}_1, ..., \boldsymbol{m}_q\}$ are the q left eigenvectors of the Jacobi matrix $\boldsymbol{J}(\boldsymbol{c}^{ss})$ corresponding to the q eigenvalues with smallest absolute value.

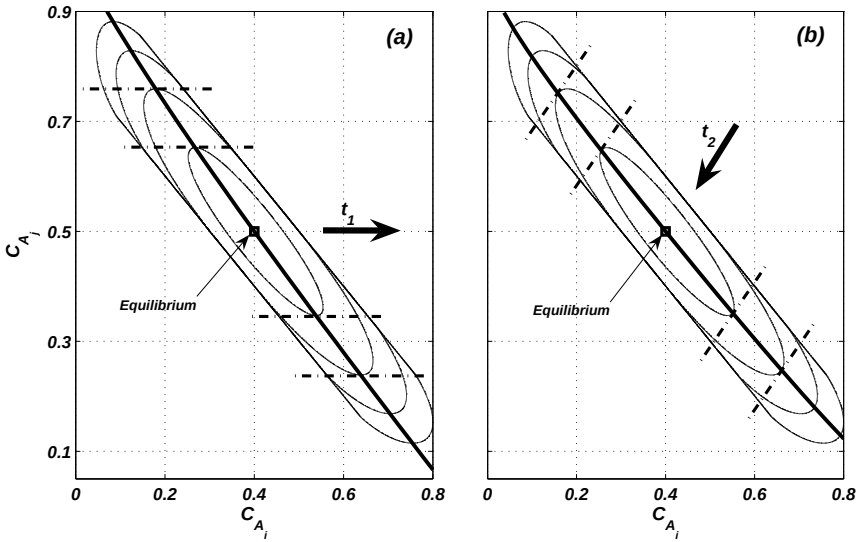

Figure 5.1.: Quasi equilibrium manifold: the geometrical interpretation. Two different QE-manifolds (bold lines in (a) and (b)) corresponding to two different sets of linear constraints in the problem (5.1).

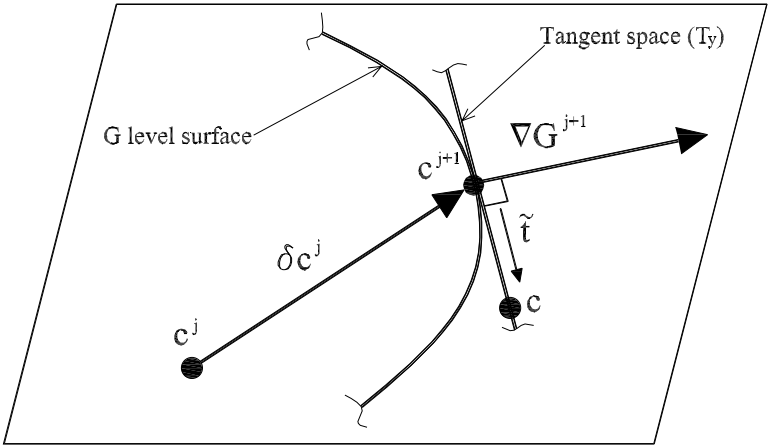

Figure 5.2.: Quasi equilibrium grid: the basic idea. The state $\boldsymbol{c}^j$ belongs to a QEM, and we search for a new point, $\boldsymbol{c}^{j+1} = \boldsymbol{c}^j + \hat{\delta}\boldsymbol{c}^j$, which belongs to the same QEM.

5.2.2. Quasi equilibrium manifold in practice

The exact solution to the minimization problem (5.1) can be found by the method of Lagrange multipliers. However, it is also known that, when the number of constraints and variables increases, such a method may become computationally intensive (see, e.g., [53]).

In this chapter, a novel procedure to compute a discrete and approximate solution to (5.1), in the phase space is presented. To this end, an algorithm (*quasi equilibrium grid algorithm*), based on the QEM geometrical construction, is developed.

5.3. 1D quasi equilibrium grid construction

Let us consider one-dimensional quasi equilibrium manifolds, that is, the set $\{\boldsymbol{m}_i\}$ consists of one vector $\boldsymbol{m}$. Let us assume that a state $\boldsymbol{c}^0$ belongs to such a manifold. One may now look for a new node $\boldsymbol{c}^1$ which belongs to the same manifold. In general, the point $\boldsymbol{c}^1$ can be obtained from $\boldsymbol{c}^0$ by shifting: $\boldsymbol{c}^1 = \boldsymbol{c}^0 + \hat{\delta}\boldsymbol{c}^0$. This idea is general and applicable whenever

a QEM node $\boldsymbol{c}^j$ is known and a new one $\boldsymbol{c}^{j+1}$ must be found (see Fig. 5.2):

$$\boldsymbol{c}^{j+1} = \boldsymbol{c}^j + \hat{\delta}\boldsymbol{c}^j. \tag{5.2}$$

First of all, any node $\boldsymbol{c}^j$ has to fulfill the conservation of elements (1.11). Let $\{\boldsymbol{\rho}_i\}$ be a basis spanning the null space of matrix $\boldsymbol{D}$. A convenient way to take the conservation laws (1.11) automatically into account is to express any shift $\hat{\delta}\boldsymbol{c}^j$ as a linear combination of vectors $\boldsymbol{\rho}_i$:

$$\hat{\delta}\boldsymbol{c}^j = \sum\nolimits_{i=1}^{z} \mu_i \boldsymbol{\rho}_i, \tag{5.3}$$

where $z = n - d$ is the dimension of the basis $\{\boldsymbol{\rho}_i\}$. By referring to Fig. 5.2, let us now discuss further the tangent space T_y to the G level surface at an arbitrary quasi equilibrium point $\boldsymbol{c}^{j+1}$. The space T_y geometrically represents the linear constraints of the problem (5.1). Therefore, any point $\boldsymbol{c}$ of T_y satisfies that constraint, but only $\boldsymbol{c}^{j+1}$ minimizes the G function. The line l, passing through both $\boldsymbol{c}^{j+1}$ and $\boldsymbol{c}$, has the parametric form $\boldsymbol{c} = \varphi\tilde{\boldsymbol{t}} + \boldsymbol{c}^{j+1}$, where $\tilde{\boldsymbol{t}}$ is a vector of T_y spanning l, while φ is the parameter. In general, the linear constraints of the problem (5.1) can be also written as:

$$\begin{aligned} \boldsymbol{m}\boldsymbol{c}^T &= \varphi\boldsymbol{m}\tilde{\boldsymbol{t}}^T + \boldsymbol{c}^{j+1}\boldsymbol{m}^T \quad \Rightarrow \quad \boldsymbol{m}\tilde{\boldsymbol{t}}^T = 0, \quad \forall\tilde{\boldsymbol{t}} \\ \boldsymbol{d}_i\boldsymbol{c}^T &= \varphi\boldsymbol{d}_i\tilde{\boldsymbol{t}}^T + \boldsymbol{c}^{j+1}\boldsymbol{d}_i^T \quad \Rightarrow \quad \boldsymbol{d}_i\tilde{\boldsymbol{t}}^T = 0, \quad \forall\tilde{\boldsymbol{t}} \end{aligned} \tag{5.4}$$

where $\boldsymbol{m}$ and $\boldsymbol{d}_i$ are the reduced variable vector ($q = 1$) and the generic row of matrix $\boldsymbol{D}$, respectively. In general, the vector $\tilde{\boldsymbol{t}}$, that respects (5.4), can be written as a linear combination of some vectors $\boldsymbol{t}_k$, where $\{\boldsymbol{t}_k\}$ denotes a basis in the null space of that matrix $\boldsymbol{E}$, whose first row is given by $\boldsymbol{m}$ and the rest by the rows of $\boldsymbol{D}$:

$$\boldsymbol{E} = \begin{bmatrix} \boldsymbol{m} \\ \boldsymbol{D} \end{bmatrix}. \tag{5.5}$$

Note that the dimension of $\{\boldsymbol{t}_k\}$ is $z-1$. The *quasi equilibrium requirement* simply becomes the orthogonality condition:

$$\tilde{\boldsymbol{t}}\boldsymbol{\nabla}G(\boldsymbol{c}^{j+1})^T = 0, \quad \forall\tilde{\boldsymbol{t}} \in T_y \tag{5.6}$$

which also implies:

$$\boldsymbol{t}_k\boldsymbol{\nabla}G(\boldsymbol{c}^{j+1})^T = 0, \quad \forall k = 1, ..., z-1. \tag{5.7}$$

The quasi equilibrium grid algorithm is based on the system (5.7) and two further assumptions. First, we assume that the known node $\boldsymbol{c}^j$ is

close to the QEM, although it does not necessarily belong to it. Secondly, the vector $\hat{\delta}\boldsymbol{c}^j$ is small enough, so that the gradient $\boldsymbol{\nabla} G(\boldsymbol{c}^{j+1})$ can be approximated as follows:

$$\boldsymbol{\nabla} G(\boldsymbol{c}^{j+1}) \cong \boldsymbol{\nabla} G(\boldsymbol{c}^j) + \boldsymbol{H}(\boldsymbol{c}^j)\hat{\delta}\boldsymbol{c}^j, \tag{5.8}$$

where the matrix $\boldsymbol{H}(\boldsymbol{c}^j)$ is evaluated at the point $\boldsymbol{c}^j$. Upon substitution of equations (5.8) and (5.3) in (5.7), we obtain:

$$\sum_{i=1}^{z} \boldsymbol{t}_k \boldsymbol{H}(\boldsymbol{c}^j)\boldsymbol{\rho}_i^T \mu_i = -\boldsymbol{t}_k \boldsymbol{\nabla} G(\boldsymbol{c}^j)^T, \quad \forall k = 1, ..., z-1 \ . \tag{5.9}$$

By using the entropic scalar product (2.4), equations (5.9) can be cast into the form:

$$\sum_{i=1}^{z} \langle \boldsymbol{t}_k, \boldsymbol{\rho}_i \rangle \mu_i = -\boldsymbol{t}_k \boldsymbol{\nabla} G^T, \quad \forall k = 1, ..., z-1 \ . \tag{5.10}$$

Both the matrix $\boldsymbol{H}$ and the gradient $\boldsymbol{\nabla} G$ are calculated at the known node $\boldsymbol{c}^j$. Note that the right-hand side of (5.10) vanishes if the state $\boldsymbol{c}^j$ is exact solution of the problem (5.1). A collection of nodes, subsequently evaluated solving (5.10), will be referred to as *quasi equilibrium grid* (QEG).

5.3.1. Closure using the spacing condition

Note, however, that the system (5.10) is not closed (z unknowns μ_i, but $z-1$ equations) because it lacks an additional information about the grid spacing. In fact, a reasonable closure can be achieved by fixing the grid spacing (e.g. in Euclidean sense),

$$\begin{array}{l} \sum_{i=1}^{z} \langle \boldsymbol{t}_k, \boldsymbol{\rho}_i \rangle \, \mu_i = -\boldsymbol{t}_k \boldsymbol{\nabla} G^T, \quad \forall j = 1, ..., z-1 \\ \left\| \hat{\delta}\boldsymbol{c}^j \right\| = \varepsilon, \end{array} \tag{5.11}$$

where ε is a fixed small parameter, and $\left\| \hat{\delta}\boldsymbol{c}^j \right\|$ denotes the Euclidean norm of the vector $\hat{\delta}\boldsymbol{c}^j$. The smaller ε is chosen, the more accurate the expression (5.8) is. As it will be shown below, for small ε accurate descriptions of the quasi equilibrium manifold can be obtained. The additional condition makes (5.11) a non-linear algebraic system, and a possible way to solve it just follows. We may search for the general solution of the linear system (5.10), and then choose the one which also fulfills the non-linear condition in (5.11). Let the basis $\{\boldsymbol{\rho}_i\}$ be orthonormal (in Euclidean sense). That

is not crucial, but it proves to be convenient in the following analysis. Indeed, the non linear system (5.11) now is cast in the following form:

$$\begin{array}{l} \sum_{i=1}^{z} \langle \boldsymbol{t}_k, \boldsymbol{\rho}_i \rangle \, \mu_i = -\boldsymbol{t}_k \boldsymbol{\nabla} G^T, \quad \forall j = 1, ..., z-1 \\ \sum_{i=1}^{z} \mu_i^2 = \varepsilon^2. \end{array} \tag{5.12}$$

A general solution of (5.10) can always be written as:

$$\begin{bmatrix} \mu_1 \\ \vdots \\ \mu_z \end{bmatrix} = w \begin{bmatrix} \tilde{\nu}_1 \\ \vdots \\ \tilde{\nu}_z \end{bmatrix} + \begin{bmatrix} \tilde{p}_1 \\ \vdots \\ \tilde{p}_z \end{bmatrix}, \tag{5.13}$$

where w is an arbitrary parameter, while $\tilde{\boldsymbol{\nu}} = [\tilde{\nu}_1, ..., \tilde{\nu}_z]$ and $\tilde{\boldsymbol{p}} = [\tilde{p}_1, ..., \tilde{p}_z]$ are the solution of the homogeneous problem and a special solution of (5.10), respectively. Without any restriction, we assume $\tilde{\boldsymbol{\nu}} \tilde{\boldsymbol{\nu}}^T = 1$. Once $\boldsymbol{\nu}$ and $\boldsymbol{p}$ are computed, the non-linear condition in (5.12) can be written, in terms of w, as:

$$w^2 + 2\tilde{\boldsymbol{\nu}} \tilde{\boldsymbol{p}}^T w + \tilde{\boldsymbol{p}} \tilde{\boldsymbol{p}}^T - \varepsilon^2 = 0. \tag{5.14}$$

If the solvability condition is satisfied,

$$\left(\tilde{\boldsymbol{\nu}} \tilde{\boldsymbol{p}}^T\right)^2 - \left(\tilde{\boldsymbol{p}} \tilde{\boldsymbol{p}}^T\right) + \varepsilon^2 > 0, \tag{5.15}$$

the two real valued solutions of (5.14) (w_I, w_{II}), upon substitution into (5.13), provide with two possible arrays $[\mu_1, ..., \mu_z]$. Therefore, by using (5.2) and (5.3), two new nodes, $\boldsymbol{c}_I^{j+1}$ and $\boldsymbol{c}_{II}^{j+1}$ (both close to the quasi equilibrium manifold) can be evaluated from the previous node $\boldsymbol{c}^j$ (see Fig. 5.3). A suitable criterion to choose between these two solutions depends on the phase space zone where the grid needs to be constructed, and it will be clarified in section 5.6. Usually, the steady state is expected to be a good starting node (*seed*) for the QEG procedure: $\boldsymbol{c}^0 = \boldsymbol{c}^{ss}$.

Remark. The QEG-equations (5.10) can be generalized as follows:

$$\sum_{i=1}^{z} \langle \boldsymbol{t}_k, \boldsymbol{\rho}_i \rangle \mu_i = -\eta (\boldsymbol{t}_k \boldsymbol{\nabla} G^T), \quad \forall k = 1, ..., z-1, \tag{5.16}$$

where the parameter η is such that $0 \leq \eta \leq 1$. When $\eta = 1$, (5.10) is recovered. On the other hand, if the QEG-nodes are close to the QEM, then the non-homogeneous terms can be neglected (they vanish on the QEM). Therefore, a reasonable approximation of the system (5.10) is given when $\eta = 0$. In the latter case, the solvability condition (5.15) is fulfilled. If $\eta = 1$ and (5.15) does not hold, that parameter can be adjusted in such a way that the solvability condition is satisfied. In the following, if not otherwise stated, it is assumed $\eta = 1$.

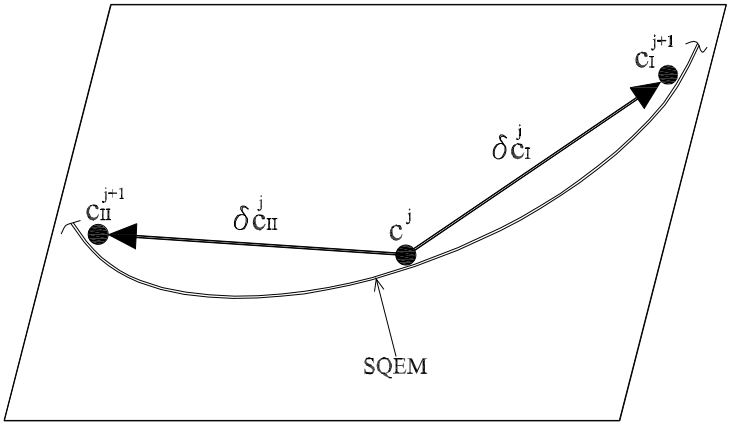

Figure 5.3.: Two solutions for the 1D QEG algorithm.

5.4. Example of 1D SQEG algorithm

In this section, an example will be considered in order to illustrate how the above algorithm works for finding one dimensional SQE-grids. Toward this end, we consider the reaction mechanism (2.15) (obeying a two-dimensional ODE system), compute the SQE-grid and compare it with the corresponding SQE-manifold. In this case, a three component vector $\boldsymbol{m}$ has to be chosen, and the QEM is constructed by solving the variational problem (5.1):

$$\begin{array}{ll} \min & G \\ s.t. & c_A + c_B + c_C = 1, \quad \boldsymbol{m}\boldsymbol{c}^T = \xi. \end{array} \tag{5.17}$$

More specifically, let $\boldsymbol{J}$ and $\boldsymbol{x}_l^s$ be the Jacobian matrix at the steady state and its slowest left eigenvector, respectively

$$\begin{array}{l} \boldsymbol{J}(\boldsymbol{c}^{ss}) = \left[\begin{array}{ccc} -30 & -4.8 & 13.5 \\ -24 & -6.2 & 13.75 \\ 54 & 11 & -27.25 \end{array} \right], \\ \boldsymbol{x}_l^s = \left[\begin{array}{ccc} 0.8807, & -0.3905, & 0.2681 \end{array} \right]. \end{array} \tag{5.18}$$

Solution to the problem (5.17), with the choice $\boldsymbol{m} = \boldsymbol{x}_l^s$, delivers the one-dimensional SQE-manifold for the case shown in Fig. 2.3 (a). Let us

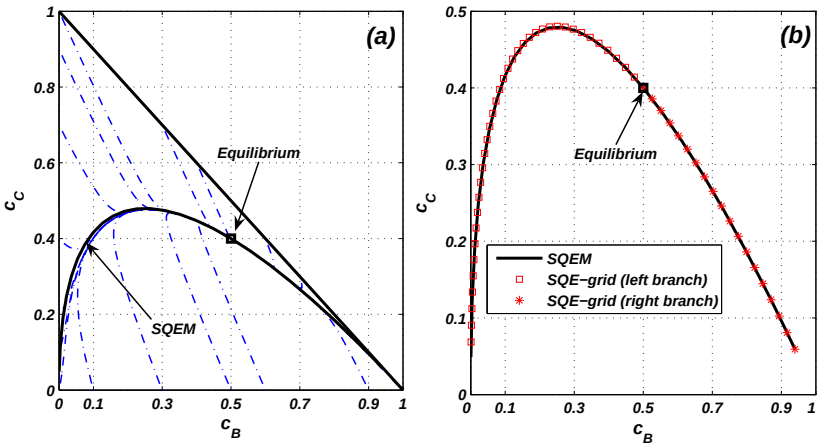

Figure 5.4.: (a) The bold curve is the SQE-manifold which was analytically evaluated by solving the (5.20). In that case the SQEM represents a very good approximation of the invariant manifold. (b) The SQE-manifold is compared with the SQE-grid, $\varepsilon^2 = 10^{-3}$.

rewrite (5.17) in the more explicit form:

$$\begin{aligned} c_{0A} &= 0.3072 + 0.7867\xi - 0.5180\phi(\xi) \\ c_{0B} &= 0.6928 - 0.7867\xi - 0.4820\phi(\xi) \\ c_{0C} &= \phi(\xi) \\ \tfrac{\partial G(\phi,\xi)}{\partial \phi} &= 0, \qquad \tfrac{\partial^2 G(\phi,\xi)}{\partial \phi^2} > 0, \end{aligned} \tag{5.19}$$

where $\boldsymbol{c}_0 = [c_{0A}, c_{0B}, c_{0C}]$ is the solution of (5.17), while ϕ denotes the relation between c_{0C} and the reduced variable ξ. Making use of the G function (2.8), the problem (5.19) is equivalent to the equation

$$\left(\frac{0.31 + 0.79\xi - 0.52\phi}{0.1}\right)^{-0.52} \left(\frac{0.69 - 0.79\xi - 0.48\phi}{0.5}\right)^{-0.48} \left(\frac{\phi}{0.4}\right) - 1 = 0. \tag{5.20}$$

The solution of (5.20) and (5.19), gives the SQEM shown in Fig. 5.4(a). We may now use the QEG-algorithm described above, in order to make a comparison with the analytic solution just found. An orthonormal basis

$\{\boldsymbol{\rho}_i\}$ in the null space of the matrix $\boldsymbol{D} = \begin{bmatrix} 1 & 1 & 1 \end{bmatrix}$ has dimension $z = 2$ and can be chosen as follows:

$$\boldsymbol{\rho}_1 = [-0.5774, 0.7887, -0.2113],\ \boldsymbol{\rho}_2 = [-0.5774, -0.2113, 0.7887]. \quad (5.21)$$

The matrix $\boldsymbol{E}$ has the form:

$$\boldsymbol{E} = \begin{bmatrix} 0.8807 & -0.3905 & 0.2680 \\ 1 & 1 & 1 \end{bmatrix}, \quad (5.22)$$

and a vector $\boldsymbol{t}$ spanning the null space $\ker(\boldsymbol{E})$ is:

$$\boldsymbol{t} = [-0.4229, -0.3934, 0.8163].$$

The system (5.12), in this example, simply reads:

$$\begin{aligned} &\langle \boldsymbol{t}, \boldsymbol{\rho}_1 \rangle \mu_1 + \langle \boldsymbol{t}, \boldsymbol{\rho}_2 \rangle \mu_2 = -\boldsymbol{t} \boldsymbol{\nabla} G^T \\ &\mu_1^2 + \mu_2^2 = \varepsilon^2. \end{aligned} \quad (5.23)$$

After solving (5.23) at an arbitrary QEG-node $\boldsymbol{c}^j$, the shift vector $\hat{\delta}\boldsymbol{c}^j = \mu_1 \boldsymbol{\rho}_1 + \mu_2 \boldsymbol{\rho}_2$ enables to evaluate the new QEG node $\boldsymbol{c}^{j+1} = \boldsymbol{c}^j + \hat{\delta}\boldsymbol{c}^j$. The QEG procedure, starting from the equilibrium point $\boldsymbol{c}^{ss} = \boldsymbol{c}^0$, was performed twice, keeping uniform parameter $\varepsilon^2 = 10^{-3}$. The first time, by choosing the solution in such a way that $c_B^{j+1} < c_B^j$, the left branch of the SQE-grid was obtained; then, by imposing $c_B^{j+1} > c_B^j$, the right branch was computed. The algorithm was terminated as soon as at least one component of the new node $\boldsymbol{c}^{j+1}$ becomes negative. The result, shown in Fig. 5.4(b), proves that the SQE-grid is in excellent agreement with the analytical curve (SQEM).

Remark. Notice an "a priori" assumption that the SQEG can be uniquely parameterized by the variable c_B. Indeed, the choice between the two possible solutions of the problem (5.23) is done by checking the positivity of $\Delta c_B = c_B^{j+1} - c_B^j$. Such an approach might not work if the chosen parameter is not suitable for that purpose. For example, in the case of Fig. 5.4 (b), the variable c_C cannot be used because of a turning point. The latter aspect will be discussed in section 5.6 in more detail.

5.4.1. Grid spacing choice

There is no need to stress the importance of the grid spacing parameter ε for the QEG accuracy. In the case of section 5.4, the SQEG was computed

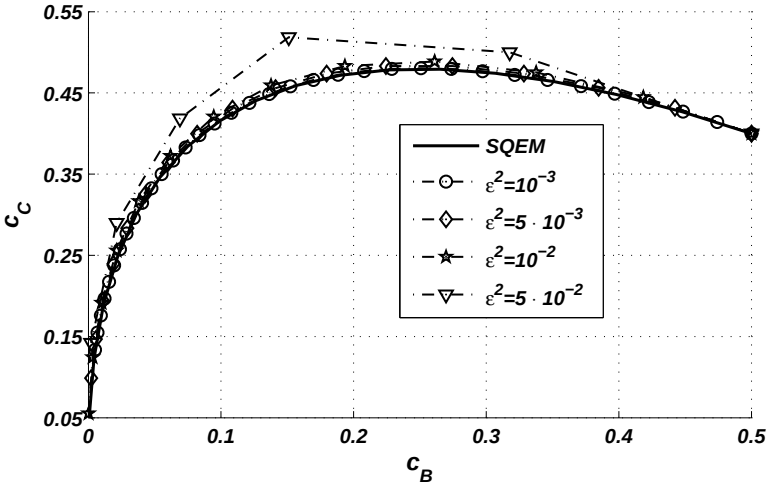

Figure 5.5.: SQEG Left branch of the case in Fig. 5.4 (b). Different approximations compared with the analytical solution (SQEM). Each grid is calculated by using a different parameter ε.

several times with different values of ε. The QEG algorithm is based on the linear approximation (5.8). Therefore, the smaller is $\left\|\hat{\delta}\boldsymbol{c}^j\right\| = \varepsilon$ the more accurate is the QEM description by means of the QEG. Nevertheless, the smaller is ε the larger is the number of times that the system (5.11) must be solved to have a grid of a fixed size. For this reason, we need to keep ε as large as possible. We estimated (at least the order of magnitude) the upper limit of spacing (ε_u) which gives a QEG "not far" from the relative QEM. From our numerical experiments, a reasonable value for that was $\varepsilon_u \cong 10^{-1}$. As Fig. 5.5 shows, the QEG is not far from the QEM even for a quite coarse grid ($\varepsilon > \varepsilon_u$).

5.5. Generalization to multi dimensional grids

The QEG algorithm, which has been developed for one dimensional grids, can be modified in order to construct multi dimensional grids. From all reasonable extension strategies, two of them will be analyzed in the following: a *straightforward extension* and a *flag extension* (the flag extension,

for invariant grids, was introduced in Ref. [30]). In the first case, the algorithm of section 5.3 and the equation system (5.12) are tuned for a q-dimensional grid calculation.

Here, the implicit assumption is that the grid dimension q is fixed and uniform everywhere in the phase space (like for the QEM construction itself). However, the second and more flexible approach, suitable for spectral quasi equilibrium grid construction, is suggested, too. In that case the grid dimension can be varied at will.

5.5.1. The straightforward extension

According to the straightforward extension, if a node $\boldsymbol{c}^j$ close to the q-dimensional QEM is known, then a new node $\boldsymbol{c}^{j+1}$ can be added to the QE-grid by shifting $\boldsymbol{c}^j$:

$$\boldsymbol{c}^{j+1} = \boldsymbol{c}^j + \hat{\delta}\boldsymbol{c}^j, \quad \hat{\delta}\boldsymbol{c}^j = \sum\nolimits_{i=1}^{z} \mu_i \boldsymbol{\rho}_i, \tag{5.24}$$

where $\{\boldsymbol{\rho}_i\}$ is a basis in the null space of matrix $\boldsymbol{D}$. The linear constraints of the problem (5.1) define the tangent space T_y to the G level surfaces in the new node $\boldsymbol{c}^{j+1}$. Let $\boldsymbol{c}$ be a generic point of T_y, the line l passing through $\boldsymbol{c}^{j+1}$ and $\boldsymbol{c}$ has the parametric form: $\boldsymbol{c} = \varphi\tilde{\boldsymbol{t}} + \boldsymbol{c}^{j+1}$, where $\tilde{\boldsymbol{t}}$ is the vector of T_y which spans l and φ is the parameter. The generalized form of the relations (5.4) is:

$$\begin{aligned}
&\boldsymbol{m}_1\boldsymbol{c}^T = \varphi\boldsymbol{m}_1\tilde{\boldsymbol{t}}^T + \boldsymbol{c}^{j+1}\boldsymbol{m}_1^T \Rightarrow \boldsymbol{m}_1\tilde{\boldsymbol{t}}^T = 0, \quad \forall\tilde{\boldsymbol{t}} \in T_y \\
&\vdots \\
&\boldsymbol{m}_q\boldsymbol{c}^T = \varphi\boldsymbol{m}_q\tilde{\boldsymbol{t}}^T + \boldsymbol{c}^{j+1}\boldsymbol{m}_q^T \Rightarrow \boldsymbol{m}_q\tilde{\boldsymbol{t}}^T = 0, \quad \forall\tilde{\boldsymbol{t}} \in T_y \\
&\boldsymbol{d}_i\boldsymbol{c}^T = \varphi\boldsymbol{d}_i\tilde{\boldsymbol{t}}^T + \boldsymbol{c}^{j+1}\boldsymbol{d}_i^T \Rightarrow \boldsymbol{d}_i\tilde{\boldsymbol{t}}^T = 0, \quad \forall\tilde{\boldsymbol{t}} \in T_y,
\end{aligned} \tag{5.25}$$

which implies that the vector $\tilde{\boldsymbol{t}}$ belongs to the null space of the matrix $\boldsymbol{E}$ ($\ker(\boldsymbol{E})$):

$$\boldsymbol{E} = \begin{bmatrix} \boldsymbol{m}_1 \\ \vdots \\ \boldsymbol{m}_q \\ \boldsymbol{D} \end{bmatrix}. \tag{5.26}$$

The dimension of the basis $\{\boldsymbol{t}_k\}$ in $\ker(\boldsymbol{E})$ is $z - q$. Since the quasi equilibrium condition requires that, among all the points $\boldsymbol{c}$ of T_y, $\boldsymbol{c}^{j+1}$ has the

minimal value of G, the following orthogonality conditions hold:

$$\boldsymbol{t}_k \boldsymbol{\nabla} G(\boldsymbol{c}^{j+1})^T = 0, \quad \forall k = 1, ..., z-q. \tag{5.27}$$

For small vector $\hat{\delta}\boldsymbol{c}^j$, the approximation (5.8) can be used, so that the (5.27) become:

$$\sum\nolimits_{i=1}^{z} \langle \boldsymbol{t}_k, \boldsymbol{\rho}_i \rangle \, \mu_i = -\boldsymbol{t}_k \boldsymbol{\nabla} G(\boldsymbol{c}^j)^T, \quad \forall k = 1, ..., z-q. \tag{5.28}$$

As shown by the system (5.28), the larger is the QEM dimension (q) the smaller is the set of "mere" quasi equilibrium equations available, while the number of unknowns remains constant (z). The closure of the rectangular system (5.28) requires q more equations and has only to do with the geometric structure which we want to endow the grid with (e.g. grid spacing, shift vector orientation in the phase-space, etc).

In general, the geometric structure of the grid under construction can be chosen at will: therefore there is no unique geometric closure for that system. However, one possible condition could be imposed, like in (5.11), by fixing the Euclidean norm of shift vector: $\left\| \hat{\delta}\boldsymbol{c}^j \right\| = \varepsilon$. Nevertheless, $(q-1)$ geometric constraints are still missing. In order to illustrate how the geometric closure issue can be overcome, the case $q = 2$ will be considered below. For this case, a possible closure, which can be easily generalized, will be presented. When a two-dimensional QEG is to be constructed, only one extra equation is needed to close the system:

$$\begin{array}{l} \sum_{i=1}^{z} \langle \boldsymbol{t}_k, \boldsymbol{\rho}_i \rangle \, \mu_i = -\boldsymbol{t}_k \boldsymbol{\nabla} G^T, \quad \forall k = 1, ..., z-2 \\ \left\| \hat{\delta}\boldsymbol{c}^j \right\| = \varepsilon. \end{array} \tag{5.29}$$

Fig. 5.6 shows that all the possible solutions of (5.29) are located, "crown-wise", in a neighborhood of the QEM. A way to choose only two of them can be achieved by introducing a new fixed vector $\tilde{\boldsymbol{m}}$ and imposing a given angle ϑ between $\tilde{\boldsymbol{m}}$ and $\hat{\delta}\boldsymbol{c}^j$:

$$\sum\nolimits_{i=1}^{z} \left(\tilde{\boldsymbol{m}} \boldsymbol{\rho}_i^T \right) \mu_i = \left\| \hat{\delta}\boldsymbol{c}^j \right\| \cdot \| \tilde{\boldsymbol{m}} \| \cos \vartheta. \tag{5.30}$$

The choice $\vartheta = \pi/2$ proves to be particularly convenient, as (5.30) becomes:

$$\sum\nolimits_{i=1}^{z} \left(\tilde{\boldsymbol{m}} \boldsymbol{\rho}_i^T \right) \mu_i = 0. \tag{5.31}$$

Eq. (5.31) enables to write a closed system:

$$\begin{array}{l} \sum_{i=1}^{z} \left\langle \boldsymbol{t}_k, \boldsymbol{\rho}_i^T \right\rangle \mu_i = -\boldsymbol{t}_k \boldsymbol{\nabla} G^T, \quad \forall k = 1, ..., z-2 \\ \sum_{i=1}^{z} \left(\tilde{\boldsymbol{m}} \boldsymbol{\rho}_i^T \right) \mu_i = 0 \\ \left\| \hat{\delta}\boldsymbol{c}^j \right\| = \varepsilon, \end{array} \tag{5.32}$$

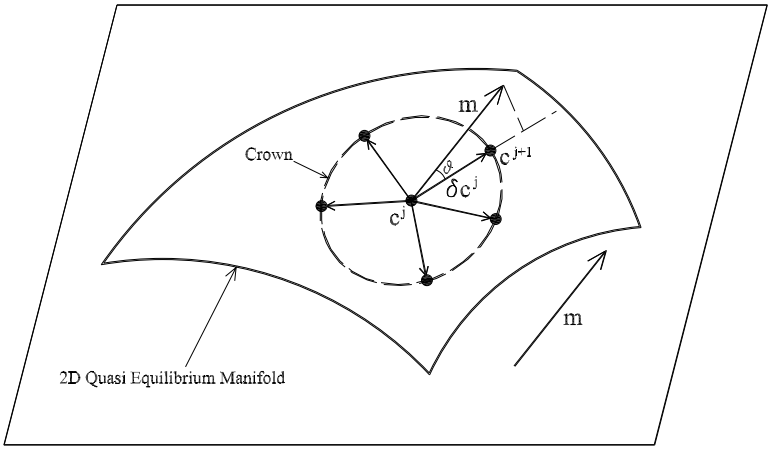

Figure 5.6.: 2D quasi equilibrium manifold. Location of solutions of the system (5.29) in the phase space.

where the extra information, through ε and $\tilde{\boldsymbol{m}}$, concern the grid spacing and the phase space zone of interest where the grid is constructed. In general, the geometric closure of (5.28) can be achieved when $(q-1)$ independent vectors $\{\tilde{\boldsymbol{m}}_k\}$ and the parameter ε are fixed.

Here, we present an approach which allows to get a rectangular structured grid. The general form of (5.32) is:

$$\begin{array}{l} \sum_{i=1}^{z} \langle \boldsymbol{t}_k, \boldsymbol{\rho}_i \rangle \mu_i = -\boldsymbol{t}_k \boldsymbol{\nabla} G^T, \quad \forall k = 1, ..., z-q \\ \sum_{i=1}^{z} \left(\tilde{\boldsymbol{m}}_k \boldsymbol{\rho}_i^T \right) \mu_i = 0, \quad \forall k = 1, ..., q-1 \\ \left\| \hat{\delta} \boldsymbol{c}^j \right\| = \varepsilon. \end{array} \tag{5.33}$$

The q-dimensional grid construction is split in q subsequent steps. Starting from the steady state $\boldsymbol{c}^{ss}$, (5.33) is solved by choosing $(q-1)$ $\boldsymbol{m}_k$ vectors among the q available and imposing: $\tilde{\boldsymbol{m}}_k = \boldsymbol{m}_k \quad \forall k = 1, ..., q-1$. In this way, a first set of QEG nodes is attained as soon as ε is fixed. Starting from each of these points, the system (5.33), by using a different combination of $\boldsymbol{m}_k$ vectors, gives some more nodes. The procedure ends (q-th step) when all the possible different combinations of $(q-1)$ vectors $\{\boldsymbol{m}_k\}$ are exhausted. In section 5.7, this method will be explained by means of an illustrative example.

5.5.2. The flag extension

A flag extension can be utilized when constructing a spectral quasi equilibrium grid. This procedure is based on the algorithm presented in section 5.3 and it naturally leads to a rectangular structured grid. Let us assume that q is the grid dimension and the q SQE-vectors $\{\boldsymbol{m}_1, ..., \boldsymbol{m}_q\}$ are fixed, such that $\boldsymbol{m}_1$ is the slowest eigenvector (corresponding to the smallest eigenvalue by absolute value), $\boldsymbol{m}_2$ the second slowest and so forth. The grid construction is achieved in q subsequent steps. At each step one more dimension is added to the grid. At the beginning, by using $\boldsymbol{m} = \boldsymbol{m}_1$, the algorithm in section 5.3 provides an one-dimensional (1D) quasi equilibrium grid. Starting from any node $\boldsymbol{c}^*$ of the latter grid, a new 1D QEG is constructed where $\boldsymbol{m} = \boldsymbol{m}_2$. In this case, the second QEG represents a trajectory on the 2D-manifold attracted to the slowest 1D-manifold in the node $\boldsymbol{c}^*$, once the fast dynamics is exhausted (see Fig. 5.7).

Notice that, G depends on the steady state $\boldsymbol{c}^{ss}$: $G = G(\boldsymbol{c}, \boldsymbol{c}^{ss})$. Since $\boldsymbol{c}^*$ can be considered as a "local equilibrium" for the fast motion, the second 1D grid is obtained by minimizing $G = G(\boldsymbol{c}, \boldsymbol{c}^*)$. Upon completion of the latter step, the grid can be extended in the third dimension by adding, at each node $\boldsymbol{c}^{'}$ of the new 2D grid, a 1D QEG where $\boldsymbol{m} = \boldsymbol{m}_3$ and $G = G(\boldsymbol{c}, \boldsymbol{c}^{'})$. In this way, the procedure is performed up to a q-dimensional grid. By a partial extension, it becomes now possible to construct grids whose dimension is different in different phase space zones.

It is worth mentioning that, the straightforward and the flag extension deliver two different objects: the first one just gives the quasi equilibrium grid "brute force", while the second one is its convenient "approximation" which has some useful features as it will be illustrated in the sequel. First of all, the flag grid does not demand any extra vector for the geometric closure and the grid dimension can be easily varied in different phase-space zones. Secondly, when a grid refinement procedure (e.g. MIG) is adopted in order to construct invariant grids, the flag extension becomes a useful tool for improving the accuracy. Indeed, let us assume that a multi dimensional invariant grid is required in order to reduce a given model. A possible strategy might be given by a "hybrid procedure" where the QEG algorithm and the MIG method are alternatively used according to the sequence:

- 1D quasi equilibrium grid construction (slowest grid);
- MIG refinements until the 1D invariant grid is obtained;

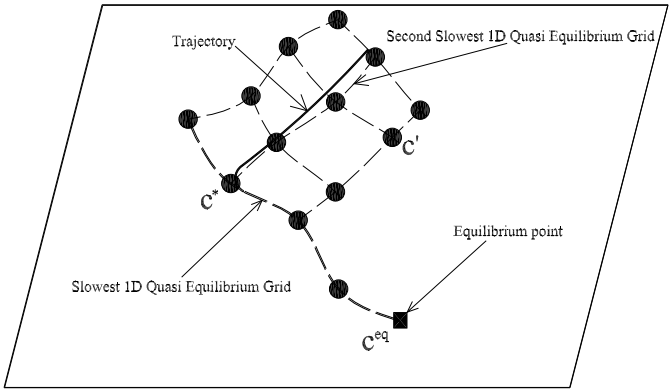

Figure 5.7.: A 2D flag. Once the 1D quasi equilibrium grid is found, from each node $\boldsymbol{c}^*$, new 1D quasi equilibrium grids are added. The second slowest 1D grid represents that trajectory collected by the first 1D quasi equilibrium grid in the node $\boldsymbol{c}^*$.

- flag extension from 1D invariant grid to 2D quasi equilibrium grid;
- MIG refinements until the 2D invariant grid is obtained;
- flag extension from 2D invariant grid to 3D quasi equilibrium grid;
- MIG refinements...

5.5.3. Beyond SQEG: GQEG and SEGQEG

The latter suggestion sheds light on one more option which, when implemented along with the flag extension, enables to improve further the accuracy of a spectral quasi equilibrium grid. Let us assume that the hybrid procedure of section 5.5.2 is employed and a k-dimensional invariant grid (let $\boldsymbol{c}^*$ be its generic node) has to be extended to a $(k+1)$-dimensional grid. This grid approximates the $(k+1)$-dimensional invariant grid better than the SQEG does, if at each invariant grid node $\boldsymbol{c}^*$ the vector $\boldsymbol{m}$ is chosen as the $(k+1)$-th slowest left eigenvector of the Jacobi matrix $\boldsymbol{J}(\boldsymbol{c}^*)$.

According to [26], here a considerable simplification can be achieved by replacing the full Jacobian $\boldsymbol{J}(\boldsymbol{c}^*)$ with:

$$\boldsymbol{J}^{sym}(\boldsymbol{c}^*) = \frac{1}{2}\left(\boldsymbol{J}(\boldsymbol{c}^*) + \boldsymbol{H}^{-1}\boldsymbol{J}^T(\boldsymbol{c}^*)\boldsymbol{H}\right), \tag{5.34}$$

where the matrix $\boldsymbol{H}$ is evaluated at the point $\boldsymbol{c}^*$. The matrix $\boldsymbol{J}^{sym}$ is symmetric with respect to the entropic scalar product (2.4), and for this reason the spectral decomposition will be much more viable. Those two new approximations will be named: *Guided Quasi Equilibrium Grid* (GQEG) when the full Jacobian $\boldsymbol{J}(\boldsymbol{c}^*)$ is used, while *Symmetric Entropic Guided Quasi Equilibrium Grid* (SEGQEG) if $\boldsymbol{J}^{sym}$ replaces the full matrix.

In order to have an idea about the effort needed, for example in a SEGQEG construction, let us consider a two dimensional grid. In this case, the spectral decomposition of a symmetric operator is performed only over the nodes of an one-dimensional grid. Moreover, also a criterion, for constructing multi dimensional grids, naturally applies: if at the node $\boldsymbol{c}^*$ of the k-dimensional invariant grid, the ratio $|\lambda_{k+1}|/|\lambda_k|$ (between eigenvalues of $\boldsymbol{J}$ or $\boldsymbol{J}^{sym}$, respectively) is not larger than a fixed threshold, the $(k+1)$-dimensional grid will not be extended at that point. In this way, the grid dimension is generally not uniform in the phase space.

The various techniques suggested above are only some possible ones. The flexibility of the method proposed enables to set up different procedures, still based on the quasi equilibrium grid approach: the QEG system (5.28) supplied with a geometrical closure (see, e.g., the construction of regular Cartesian grids in section 5.8).

5.6. Grid construction

The construction of a QEG is entirely local. Without a loss of generality, we can refer to the algebraic system (5.11), which indeed only depends on the local gradient $\nabla G(\boldsymbol{c}^j)$ and second derivative matrix $\boldsymbol{H}(\boldsymbol{c}^j)$. For this reason, in order to compute the unknown vector $\hat{\delta}\boldsymbol{c}^j$, no "a priori" grid parameterization is requested. However, a criterion able to choose between the two solutions of (5.11), without getting into troubles in the case of turning points, is needed. We may overcome that problem with the help of a proper parameterization, as suggested in section 5.4.

In general, a QEG has a natural parameterization which is given by the variables ξ^i in (5.1). Let us refer to the one dimensional construction

described in section 5.3. Here, taking the steady state $\boldsymbol{c}^{ss}$ as seed of the grid, the subsequent points can be chosen by imposing the positivity of the inner product $\hat{\delta}\boldsymbol{c}\boldsymbol{m}^T$. By extending the grid outwards from a zone of phase space close to the steady point, one reaches regions where the solution becomes unphysical (such as negative concentrations of some species). In that case, the evaluated node is cut off while the procedure starts again from $\boldsymbol{c}^{ss}$. Solutions $\hat{\delta}\boldsymbol{c}^j$ with $\hat{\delta}\boldsymbol{c}\boldsymbol{m}^T < 0$ are considered till non-negative concentrations are found.

Let n be the dimension of the phase space. The one dimensional grid is described as an ordered sequence of nodes. Those nodes can be collected in n one dimensional arrays, where in each of them a different species is stored. However, different criteria for choosing the solutions, not based on the grid parametrization, may be also used. Let $\boldsymbol{c}_I^1$ and $\boldsymbol{c}_{II}^1$ be the two solutions to (5.12) at $\boldsymbol{c}^0$, and assume that the second grid node is $\boldsymbol{c}^2 = \boldsymbol{c}_I^1$. The third grid node can be chosen such that the Euclidean distance $\left\|\boldsymbol{c}^3 - \boldsymbol{c}^0\right\|$ is maximum. Indeed, one of the two solutions evaluated at $\boldsymbol{c}^2$ is located close to $\boldsymbol{c}^0$: they would overlap if the quasi equilibrium grid nodes were exactly on the corresponding quasi equilibrium manifold. In this way, at any grid point $\boldsymbol{c}^j$, by choosing the solution which has the maximum distance $\left\|\boldsymbol{c}^{j+1} - \boldsymbol{c}^{j-1}\right\|$, the first branch of the grid is computed. Once the boundary is reached, the procedure is terminated. By means of the same criterion, the second grid branch is constructed starting from $\boldsymbol{c}^0$ and choosing the subsequent node as $\boldsymbol{c}^2 = \boldsymbol{c}_{II}^1$.

This strategy can be applied also for multi dimensional grids, if the flag extension is used. In fact, once the one dimensional grid is found, the procedure can be applied as described above. Starting from an arbitrary point of the latter grid, a two dimensional grid is built up. Here, the nodes are stored in n two dimensional arrays where the previous arrays are embedded as a single column. Similarly, the latter grid can be extended in the third dimension and so on.

5.7. Two dimensional grid example

Let us consider a model for hydrogen oxidation reaction where six species H_2 (hydrogen), O_2 (oxygen), H_2O (water), H, O, OH (radicals) are involved in six steps in a closed system under constant volume and tem-

perature (from Ref. [28], p. 291):

$$\begin{array}{l} 1.H_2 \rightleftharpoons 2H, \quad k_1^+ = 2, \\ 2.O_2 \rightleftharpoons 2O, \quad k_2^+ = 1, \\ 3.H_2O \rightleftharpoons H + OH, \quad k_3^+ = 1, \\ 4.H_2 + O \rightleftharpoons H + OH, \quad k_4^+ = 10^3, \\ 5.O_2 + H \rightleftharpoons O + OH, \quad k_5^+ = 10^3, \\ 6.H_2 + O \rightleftharpoons H_2O, \quad k_6^+ = 10^2. \end{array} \tag{5.35}$$

The atom conservation laws are:

$$\begin{array}{l} 2c_{H_2} + 2c_{H_2O} + c_H + c_{OH} = b_H = 2 \\ 2c_{O_2} + c_{H_2O} + c_O + c_{OH} = b_O = 1. \end{array} \tag{5.36}$$

The steady state is fixed as follows

$$\begin{array}{l} c_{H_2}^{ss} = 0.27,\ c_{O_2}^{ss} = 0.135,\ c_{H_2O}^{ss} = 0.7, \\ c_H^{ss} = 0.05,\ c_O^{ss} = 0.02,\ c_{OH}^{ss} = 0.01, \end{array} \tag{5.37}$$

an the rest of the rate constants k_i^- are calculated using the detailed balance principle (1.5). The system under consideration is fictitious in the sense that the subset of equations corresponds to the simplified picture of this chemical process and the rate constants reflect only orders of magnitude for relevant real wold systems. We assume that the Lyapunov function G has the ideal gas form (2.8):

$$G = \sum\nolimits_{i=1}^{6} c_i \left[\ln\left(\frac{c_i}{c_i^{ss}} \right) - 1 \right]. \tag{5.38}$$

Here, we are interested in the construction of a two dimensional (2D) SQEG. Spectral decomposition of Jacobian matrix $\boldsymbol{J}(\boldsymbol{c}^{ss})$ delivers:

$$\begin{array}{l} \boldsymbol{x}_l^{s1} = [-0.577, -0.568, 0.225, 0.0482, 0.0666, -0.536] \\ \boldsymbol{x}_l^{s2} = [0.00682, -0.00595, 0.0221, -0.7, -0.713, 0.423]\,, \end{array} \tag{5.39}$$

where $\boldsymbol{x}_l^{s1}$ and $\boldsymbol{x}_l^{s2}$ are the slowest and the second slowest eigenvectors of $\boldsymbol{J}$, respectively.

5.7.1. The two dimensional straightforward extension

In order to construct a 2D SQEG for the latter reaction mechanism, the straightforward extension was used as first strategy. Matrices $\boldsymbol{D}$ and $\boldsymbol{E}$

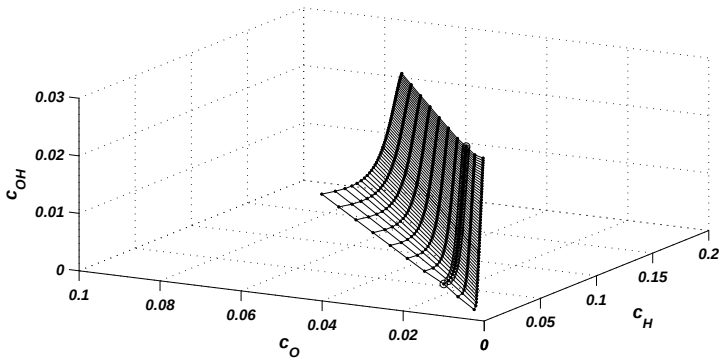

Figure 5.8.: The 2D SQEG constructed by using the straightforward extension with $\varepsilon^2 = 0.5 \cdot 10^{-3}$: projection into the phase-subspace (c_H, c_O, c_{OH}).

take now the form:

$$\boldsymbol{D} = \begin{bmatrix} 2 & 0 & 2 & 1 & 0 & 1 \\ 0 & 2 & 1 & 0 & 1 & 1 \end{bmatrix}, \tag{5.40}$$

$$\boldsymbol{E} = \begin{bmatrix} -0.577 & -0.568 & 0.225 & 0.0482 & -0.0666 & -0.536 \\ 0.00682 & -0.00595 & 0.0221 & -0.7 & -0.713 & 0.423 \\ 2 & 0 & 2 & 1 & 0 & 1 \\ 0 & 2 & 1 & 0 & 1 & 1 \end{bmatrix}. \tag{5.41}$$

As suggested in the end of section 5.5.1, the procedure has been started from the equilibrium point and it was split in two subsequent steps. At the beginning, the system (5.32) was solved by imposing $\varepsilon^2 = 0.5 \cdot 10^{-3}$ and $\tilde{\boldsymbol{m}} = \boldsymbol{x}_l^{s2}$: in this way the grid nodes, denoted by circles in Fig. 5.8, were obtained. During the second step, (5.32) was solved by starting from any circle: this time, the geometric constraints were chosen such that $\varepsilon^2 = 0.5 \cdot 10^{-3}$ and $\tilde{\boldsymbol{m}} = \boldsymbol{x}_l^{s1}$. During this step, the transversal dots of Fig. 5.8, corresponding to each circle, were computed.

5.7.2. The two dimensional flag extension

Here we intend to apply the flag extension technique to the above example, and thus we first construct the 1D spectral quasi equilibrium grid. Toward

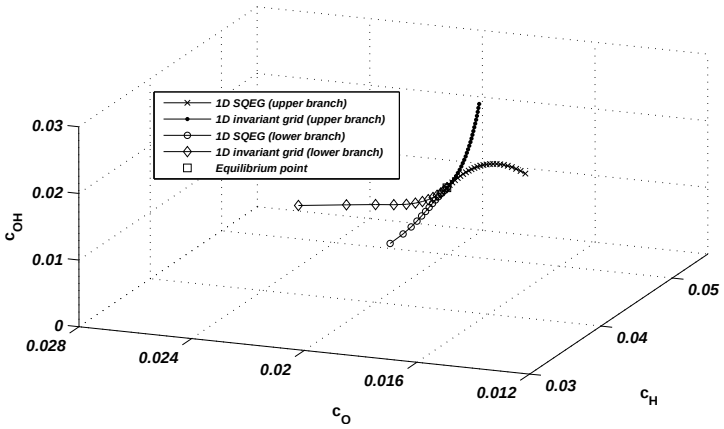

Figure 5.9.: 1D spectral quasi equilibrium grid with $\varepsilon^2 = 1 \cdot 10^{-3}$ compared to the 1D invariant grid obtained by MIG refinements.

this end, matrices $\boldsymbol{D}$ and $\boldsymbol{E}$ are computed as follows

$$\boldsymbol{D} = \begin{bmatrix} 2 & 0 & 2 & 1 & 0 & 1 \\ 0 & 2 & 1 & 0 & 1 & 1 \end{bmatrix}, \tag{5.42}$$

$$\boldsymbol{E} = \begin{bmatrix} -0.577 & -0.568 & 0.225 & 0.0482 & 0.0666 & -0.536 \\ 2 & 0 & 2 & 1 & 0 & 1 \\ 0 & 2 & 1 & 0 & 1 & 1 \end{bmatrix}. \tag{5.43}$$

Starting from the steady state $\boldsymbol{c}^{ss}$, the 1D grid is constructed by solving the system (5.12) with $\varepsilon^2 = 1 \cdot 10^{-3}$ (see Fig. 5.9), and the technique described in section 5.5.2 was used to extend the latter grid into the second dimension. In particular, now a new matrix $\boldsymbol{E}$ is to be considered:

$$\boldsymbol{E} = \begin{bmatrix} 0.00682 & -0.00595 & 0.0221 & -0.7 & -0.713 & 0.423 \\ 2 & 0 & 2 & 1 & 0 & 1 \\ 0 & 2 & 1 & 0 & 1 & 1 \end{bmatrix},$$

while the Lyapunov function G has the form:

$$G = \sum\nolimits_{i=1}^{6} c_i \left[\ln\left(\frac{c_i}{c_i^*}\right) - 1 \right], \tag{5.44}$$

where $\boldsymbol{c}^* = (c_1^*, ..., c_6^*)$ is a generic node of the 1D grid, which is extended into the second dimension (see Fig. 5.7). Figures 5.10(a)-(b) show two

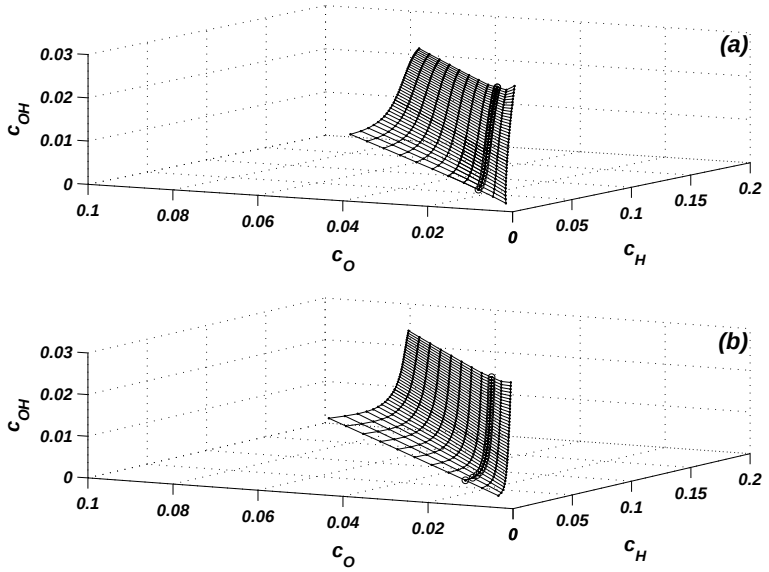

Figure 5.10.: The flag extension. (a) 2D SQEG (dots) extended from the 1D SQEG with $\varepsilon^2 = 1 \cdot 10^{-3}$ (circles). (b) 2D SQEG (dots) extended from the 1D invariant grid (circles). In the second dimension $\varepsilon^2 = 0.5 \cdot 10^{-3}$.

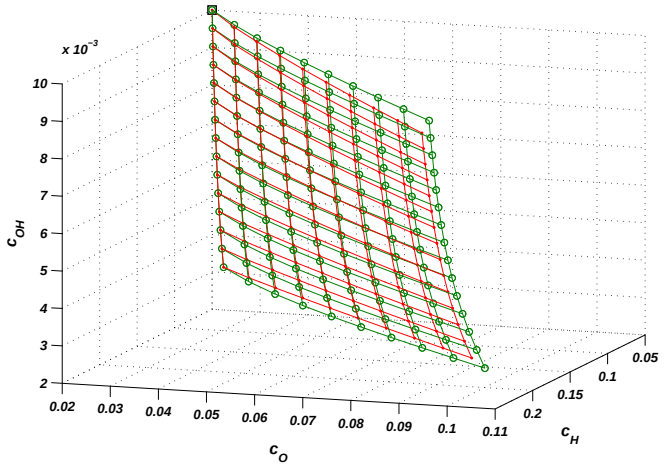

Figure 5.11.: Case 1: $k_1^+ = 2$, $k_2^+ = 1$, $k_3^+ = 1$, $k_4^+ = 10^3$, $k_5^+ = 10^3$, $k_6^+ = 10^2$, $\varepsilon^2 = 0.45 \cdot 10^3$. Two grids formed by 10×15 nodes. A 2D GQEG (dots) and a 2D invariant grid (circles) are reported. The grids are partially extended below the steady state (square).

different 2D SQE-grids: the first one is obtained by extending the 1D SQE-grid, while in the second case the 1D invariant grid is adopted. In other words, the latter result was attained by the "hybrid procedure" QEGA + MIG suggested in the end of section 5.5.2. For both cases, in the second dimension, the grid spacing was $\varepsilon^2 = 0.5 \cdot 10^{-3}$.

5.7.3. The two dimensional GQEG and SEGQEG

Finally, the GQEG and SEGQEG approximations are computed for the hydrogen oxidation reaction (5.35) (case 1). The grid spacing was kept uniform, $\varepsilon^2 = 0.45 \cdot 10^{-3}$. Each grid has 10×15 nodes and it is compared to both the SQEG (straightforward extension) of similar size (check Table 5.1) and the invariant grid. The invariant grid was obtained by refining the approximations via MIG in the form of Newton iterations. All those grids lie quite close to each other. However, a "more pathological" case 2 was also analyzed. In this case, the SQEG, far from the steady state, presents a remarkable deviation from the invariant grid: now the rate

constant set is taken as $k_1^+ = 20$, $k_2^+ = 1$, $k_3^+ = 1$, $k_4^+ = 10^3$, $k_5^+ = 10^3$, $k_6^+ = 10^2$, while the steady state coordinates are still given by (5.37). Now, the SQEG, GQEG and SEGQEG were constructed by choosing the grid spacing and size as for the previous case 1. Note that all the grids were partially extended only below the steady state in the phase space zone, where they present the largest deviation from the invariant grid. This time, those three approximations have a low invariance defect only near the steady state. In order to estimate how far each grid is from the invariant one, the following procedure is implemented. A 10×15 array, collecting at any grid node an invariance defect measure, is constructed. As suggested in [16], that local measure may be $\sqrt{\left(\boldsymbol{\Delta}^T \boldsymbol{\Delta}\right) / \left(\boldsymbol{f}^T \boldsymbol{f}\right)}$, where $\boldsymbol{\Delta}$ and $\boldsymbol{f}$ are the invariance defect and the vector field, respectively. $\boldsymbol{\Delta}$ is evaluated by using the thermodynamic projector (2.13). By averaging over all the invariance defect measures, the mean invariance defect is computed: results for both cases are condensed in Table 5.1. Note that the adopted invariance defect measure is dimensionless, as it compares the invariance defect with the vector field. Calculations prove that the GQEG is better than the SQEG (straightforwardly extended); nevertheless the SEGQEG construction, since it requires a much lower computational effort and still has an error similar to the GQEG, is recommended when the SQEG is considered not satisfactory (e.g. large mean defect).

5.8. Regular Cartesian grids

As discussed in the Appendix C, when using interpolation for analytical continuation of the manifold from the grid, it may prove convenient to perform the construction directly on a regular Cartesian grid in terms of the grid parameters ξ^i. To this end, we consider the following special closure of the quasi equilibrium equations (5.28), which can be regarded as a sub-case of the straightforward extension:

$$\begin{array}{l} \sum_{i=1}^{z} \langle \boldsymbol{t}_k, \boldsymbol{\rho}_i \rangle \, \delta_i = -\boldsymbol{t}_k \boldsymbol{\nabla} G^T, \quad k = 1, ..., z-q \\ \sum_{i=1}^{z} \left(\boldsymbol{m}_1 \boldsymbol{\rho}_i^T \right) \delta_i = 0, \\ \vdots \\ \sum_{i=1}^{z} \left(\boldsymbol{m}_j \boldsymbol{\rho}_i^T \right) \delta_i = \varepsilon_j, \\ \vdots \\ \sum_{i=1}^{z} \left(\boldsymbol{m}_q \boldsymbol{\rho}_i^T \right) \delta_i = 0. \end{array} \tag{5.45}$$

The new QEG point

$$\boldsymbol{c}^{j+1} = \boldsymbol{c}^{j} + \sum\nolimits_{i=1}^{z} \delta_i \boldsymbol{\rho}_i,$$

computed by using the (5.45) lies on a regular Cartesian grid in the space $\left\{\xi^1, ..., \xi^q\right\}$, with the fixed parameter ε_j defining the grid step along the macroscopic variable ξ^j. The interested reader can find in the Appendix E an application of the quasi-equilibrium algorithm in the form (5.45).

5.9. Discussion of the method

The presented methodology is implicitly based on the hypothesis of connected slow invariant manifolds, but this is not necessarily the case. Further aspects of the applicability of quasi equilibrium approximations can be found in Refs [16, 26, 28, 30]. Nevertheless, when that hypothesis is valid, the rationale behind the fact that quasi equilibrium manifolds provide approximations for slow invariant manifolds, in the case of fast and slow motion decomposition (i.e. gap in the eigenvalues of the Jacobi matrix) and existence of a Lyapunov function G, is schematically illustrated in Fig. 2.2. For such systems, a solution trajectory that approaches the slow invariant manifold, during the initial fast transient, only moves (approximately) in the fast subspace L. Since G is decreasing in the course of the fast motions, points $\boldsymbol{c}^*$ which minimize G on the affine space $(\boldsymbol{c}^* + L)$ are expected to be located close to the slow invariant manifold. However, when the construction of the slow invariant manifold needs to be addressed, the subspace L is not known "a priori" and it generally depends on the point $\boldsymbol{c}^*$. Hence, for constructing the quasi equilibrium approximation, a guess of L is needed. Here, it is important to discuss some connections with the work of other authors. It is known for thermodynamics that for some closed reactive systems, the Lyapunov function is given by thermodynamic potentials (e.g. Gibbs free energy if temperature and pressure are constant, entropy if energy and density are constant, etc...).

Notice that the very first use of entropy maximization has to be referred to the classical work of Gibbs [25] and later addressed to Jaynes [36]. More generally, the quasi equilibrium approach constitutes an attempt in statistical mechanics to link microscopic models to the macroscopic ones providing the latter with a closure. For example, in [29] and [35], equations describing quasi equilibrium dynamics for polymer are presented. Referring to chemical kinetics, also the method of Rate Controlled

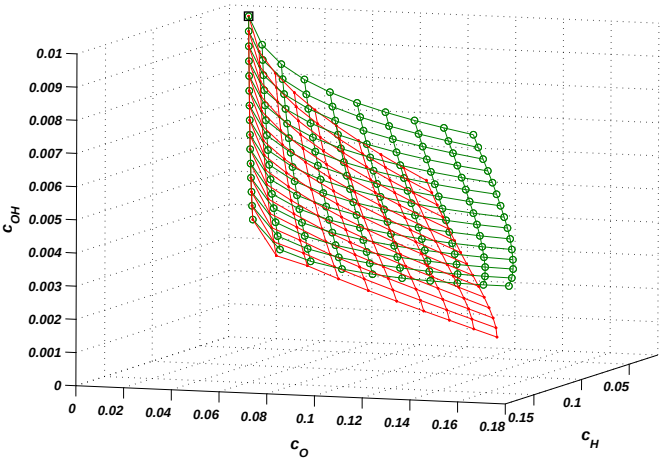

Figure 5.12.: Case 2: $k_1^+ = 20$, $k_2^+ = 1$, $k_3^+ = 1$, $k_4^+ = 10^3$, $k_5^+ = 10^3$, $k_6^+ = 10^2$, $\varepsilon^2 = 0.45 \cdot 10^3$. Two grids formed by 10×15 nodes. A 2D GQEG (dots) and a 2D invariant grid (circles) are reported. The grids are partially extended below the steady state (square).

Constrained Equilibrium (RCCE), introduced by Keck & Gillespie [39], reviewed by Keck (1990) and further developed in the recent literature [7, 34], can be related to the quasi equilibrium approximation. An interesting geometric viewpoint of RCCE is given by Tang & Pope [65]. After choosing a set of constraints, RCCE method makes use of the assumption that chemical systems evolve according to a sequence of quasi equilibrium states which are function of the instantaneous values of such constraints. Those constraints are related to the unknown fast subspace L and need to be chosen. In general, some variable constraints (total moles, active valences, etc...), in addition to elemental fixed constraints (total number of atom moles), are imposed for minimizing the thermodynamic potential and evaluating the species constrained composition.

In order to evaluate a constrained equilibrium state, the Lagrange multipliers problem can be iteratively solved via available routines (see e.g. STANJAN [59]). Nevertheless, some differences between the two approaches need to be stressed. The QEGA is not an iterative procedure. Provided that the steady state (or any other point close to such a QE-manifold)

Approximation	1.case	2.case
SQEG	0.318	0.645
GQEG	0.238	0.460
SEGQEG	0.303	0.491

Table 5.1.: Mean invariance defect (dimensionless): three approximations of the invariant grid under comparison for the hydrogen oxidation reaction.

is known, it aims at computing a set of nodes in the phase space (QEG) approximating the quasi equilibrium manifold. Since the latter grid is generally not invariant [65] (see also table 5.1), it has to be tabulated and used only as first approximation in the MIG procedure described in sections 2.3.4 and 2.3.5. Moreover, the suggested construction uses a special choice of the constraints, based on spectral decomposition of Jacobian at few points, for constructing SQEG, GQEG and SEGQEG. As the above examples show, such approximate grids are accurate only in a neighborhood of the steady state. However, here we are not interested in the quasi equilibrium dynamics *per se*. For that reason, once a grid is constructed by the QEGA, it needs to be refined via MIG iterations. Only the fixed point of the MIG method (invariant grid) is considered for integrating the reduced system.

As stated at the beginning of this chapter, the classical approach to the problem of minimization of convex functions subject to constraints is the Lagrange multipliers method. When the number of species becomes large enough, a non-linear system needs to be solved through Newton-Raphson iterations for each chemical constrained equilibrium point. Alternatively, the chemical composition of ideal gas mixtures may be evaluated, through the more stable Gibbs function continuation method, by integrating a set of ODEs [53]. However, here we suggest a grid-based approach to that problem. In fact, the quasi equilibrium algorithm is a tool that aims at extending automatically a grid around a given point in the phase space. Although such a procedure is based on the geometry behind the Lagrange multipliers method, as explained in sections 5.5.2 and 5.5.3 it may also deliver approximations of the slow invariant manifold even more accurate than a quasi equilibrium grid itself (see Table 5.1). Indeed, a multi dimensional GQEG (or SEGQEG) is not only based on the minimization of a thermodynamic potential, but it also takes into account information from the Jacobi matrix evaluated at a few points. Therefore, a GQEG is not a "pure" quasi equilibrium approximation any longer. In that case, the flag

extension allows both the construction of objects of varying dimension and implementation of hybrid procedure: QEGA+MIG.

On the other hand, in such a flexible grid-based approach, in order to compute an uniform grid the number of points scales as ε^{-q}. Where q is the grid dimension, while ε is the small grid parameter. In general, ε is not kept constant. For instance, during a hierarchical construction (flag extension), it is convenient to use a coarser grid for describing the lowest-dimensional manifolds.

In our calculations, the criterion used to end the grid was based on non-negative concentrations. As soon as the evaluated grid point leaves the admissible phase space, it is cut and the procedure terminated (see also section 5.6). That may seem inefficient, but it is worth to point out that the construction of the quasi equilibrium grid is done only once, and then tabulated for a later use in MIG procedure.

5.10. Conclusions

In this chapter, the problem of grid-based approximation of quasi equilibrium manifolds is addressed. To this end, the notion of quasi equilibrium grid (QEG) is introduced, and an algorithm for constructing QE-grids is worked out (QEGA). The QEGA is a completely numerical procedure, and it has been demonstrated that it provides with accurate enough approximations of slow invariant manifolds (SIM), which reveal thus particularly suitable for initializing the MIG procedure.

Moreover, it has been illustrated that some hybrid procedures, where both methods QEGA and MIG are alternatively used, enable to obtain even more accurate approximations. In particular, It was proved that two of such procedures deliver enhanced approximations of SIM: the *Guided Quasi Equilibrium Grid* and the *Symmetric Entropic Guided Quasi Equilibrium Grid*.

Here, it is worth stressing the major advantage of the proposed method. It is a numerical algorithm which only deals with sets of nodes in the concentration space, and it is based on a fully local construction. Namely, the computation of a new node $\boldsymbol{c}^{j+1}$, which has to be added to the grid, only depends on the previous neighbor $\boldsymbol{c}^{j}$: those aspects make the QEG construction suitable for numerical applications and parallel realizations.

Finally, it is not excluded that the QEGA is applicable not only for model reduction, but in different fields, too. Indeed, it was mentioned that the QEM notion already is exploited for some applications in the lattice Boltzmann method simulations (see also the Appendix E). More generally, the QEGA is a numerical tool which can be used to find a grid-based approximation for the locus of minima of a convex function under some linear constraints.

6. Invariant grids for combustion

6.1. Introduction

Constructing slow invariant manifolds enables to establish a simplified description of complex phenomena, such as combustion, by extracting only the slow dynamics and neglecting the fast one. As a result, a detailed large set of equations can be reduced to a much smaller and less stiff system without a significant loss of accuracy.

In this chapter, the method of invariant grids (MIG) is utilized to study a combustion problem (see also [17]). The quasi equilibrium grid algorithm is adopted to obtain a first approximation of SIM, which is afterwards refined via MIG iterations. The data delivered by this procedure is stored in tables and used to integrate a less stiff reduced system. Results obtained with the reduced system are compared with the detailed one, and excellent agreement is found for the dynamics of all species, including the radicals, and of the temperature.

6.2. Thermodynamic Lyapunov function

In the following, we deal with a reactive closed system under constant volume V (hence constant mixture density $\bar{\rho}$) and mixture-averaged internal energy $\bar{U}$, so that the kinetic system (1.7) describes the evolution of such a chemical system towards a unique steady state. Furthermore, we assume that there exists a strictly convex function only dependent on the state vector, that decreases monotonically in time under the dynamics of the system (1.7). Such a function $\tilde{G}$ is a global Lyapunov function of the system, and it reaches the global minimum at the steady state.

In a closed system under constant internal energy $\bar{U}$ and density $\bar{\rho}$, the value of specific mixture-averaged entropy $\bar{s}$ (per unit mass) must increase

monotonically starting from any initial condition. Therefore, the function $\tilde{G} = -\bar{s}$

$$\tilde{G} = \frac{-\sum_{i=1}^{n} \left[s_i(T) - \mathcal{R} \ln(X_i) - \mathcal{R} \ln\left(\frac{p}{p_{ref}}\right) \right] X_i}{\bar{W}}, \tag{6.1}$$

is a Lyapunov function with respect to (1.7), where $\bar{W}$ is the mean molecular weight, s_i and X_i are the entropy and the mole fraction of species i, respectively, $\mathcal{R}$ is the universal gas constant while p and p_{ref} are the mixture total pressure and a given reference pressure, respectively. Specific entropy s_i, according to [40], is assumed to have the following dependence on the temperature T

$$s_i(T) = R\left(a_{i1} \ln T + a_{i2} T + \frac{a_{i3}}{2} T^2 + \frac{a_{i4}}{3} T^3 + \frac{a_{i5}}{4} T^4 + a_{i7}\right). \tag{6.2}$$

An another Lyapunov function can be constructed as follows:

$$G = \tilde{G} + \sum_{k=1}^{d} \left(\lambda_k \sum_{i=1}^{n} \mu_{ki} c_i \right) + \lambda \sum_{i=1}^{n} W_i c_i, \tag{6.3}$$

where d is the number of chemical elements involved in the reaction, μ_{ki} represents the number of atoms of the k-th chemical element in species i and W_i is the molecular weight of species i. The Lagrange multipliers λ_k and λ are now chosen by imposing $\boldsymbol{\nabla} G|_{\bar{U}} = \mathbf{0}$ at the steady state, where the function G is differentiated with respect to the molar concentrations c_i under fixed $\bar{U}$. Because of the conservation of atoms and density, the time derivative of (6.3) is non-positive:

$$\frac{dG}{dt} = \frac{d\tilde{G}}{dt} \leq 0, \quad \frac{dN_k}{dt} = 0, \quad \frac{d\bar{\rho}}{dt} = 0,$$

where the conserved atom mole numbers N_k and the density $\bar{\rho}$ read as follows:

$$N_k = \sum\nolimits_{i=1}^{n} \mu_{ki} c_i, \quad \bar{\rho} = \sum\nolimits_{i=1}^{n} W_i c_i. \tag{6.4}$$

Notice that, the entropy function $\tilde{G}$ (6.1) is still a thermodynamic Lyapunov function with respect to the temporal dynamics of an homogeneous reactor under fixed pressure p and mixture-averaged enthalpy $\bar{h}$. However, in the latter case, the G function is constructed as follows:

$$G = \tilde{G} + \sum_{k=1}^{d} \left(\lambda_k \sum_{i=1}^{n} \frac{\mu_{ik}}{W_i} Y_i \right), \tag{6.5}$$

where the Lagrange multipliers λ_k are chosen in such a way that $\boldsymbol{\nabla} G|_{p,\bar{h}} = \mathbf{0}$ at the steady state, with the gradient of G computed under fixed p and $\bar{h}$. This time, the conserved atom mole numbers N_k can be expressed as

$$N_k = \sum_{i=1}^{n} \frac{\mu_{ik}}{W_i} Y_i, \quad k = 1, \ldots, d, \tag{6.6}$$

where Y_i denotes the mass fraction of species i. More details are given in the Appendix A.

6.3. Reduction of a detailed hydrogen mechanism

In the following, a H_2-air system reacting according to the nine-species, 21-step detailed mechanism of Li et al. [44] (reported in the Appendix D) is studied. An adiabatic constant volume reactor with H_2-air mixture in stoichiometric proportions is considered, where the density and the mixture-averaged specific energy are chosen as $\bar{\rho} = 4.58\ kg/m^3$ and $\bar{U} = 1.28\ MJ/kg$, respectively (corresponding to the temperature $T = 1540$ K of the unburned mixture). The one- and two-dimensional slow invariant manifolds are described by constructing the pertinent invariant grids, which are utilized to integrate the reduced system. Here, the concentration of species k is expressed in terms of the *specific mole numbers*: $\phi_k = c_k/\bar{\rho}$.

6.3.1. 1D and 2D thermodynamic projector

In this section, we specifically discuss the construction of thermodynamic projector for 1D and 2D grids, in the nine-dimensional concentration space. Let a generic 1D grid $\mathcal{G}$ be given as a collection of states in the concentration space. Assuming that a parameter ξ is uniquely associated with each grid point, the tangent vector $\hat{\boldsymbol{u}} = (dc_1/d\xi, ..., dc_9/d\xi)$, at any internal grid node $\boldsymbol{c}^j$, can be approximated by central finite differences

$$\frac{dc_i}{d\xi} \cong \frac{c_i^{j+1} - c_i^{j-1}}{2\Delta\xi},$$

with $\Delta\xi$ denoting the grid spacing of the parameter ξ, whereas for boundary nodes a first order finite difference (backward or forward) can be used.

The thermodynamic projector is a 9×9 matrix, whose generic component is:

$$\boldsymbol{P}(i,j) = \frac{1}{\boldsymbol{\nabla} G \hat{\boldsymbol{u}}^T} \left(\boldsymbol{\nabla} G_j \hat{\boldsymbol{u}}_i \right). \tag{6.7}$$

For a 2D grid, two parameters ξ^1 and ξ^2 are associated with each point, so that two tangent vectors $\boldsymbol{u}_1$ and $\boldsymbol{u}_2$ can be evaluated at any grid node $\boldsymbol{c}^{j,k}$ as follows

$$\boldsymbol{u}_{1i} = \frac{\partial c_i}{\partial \xi^1} \cong \frac{c_i^{j+1,k} - c_i^{j-1,k}}{2\Delta\xi^1}, \quad \boldsymbol{u}_{2i} = \frac{\partial c_i}{\partial \xi^2} \cong \frac{c_i^{j,k+1} - c_i^{j,k-1}}{2\Delta\xi^2}.$$

In order to construct the 2D thermodynamic projector, it is convenient to introduce the 10×11 block matrix

$$\begin{bmatrix} 0 & 0 & \boldsymbol{\nabla} G \\ \boldsymbol{u}_1^T & \boldsymbol{u}_2^T & -\boldsymbol{I} \end{bmatrix}, \tag{6.8}$$

with $\boldsymbol{I}$ denoting the identity matrix. Let us assume that the matrix (6.8) is of full rank, and $\hat{\boldsymbol{u}}_2$ is formed by the first nine components of a vector spanning the null space of (6.8). According to the notations introduced in section 2.3.2, let T_y indicate the tangent hyperplane spanned by $\boldsymbol{u}_1$ and $\boldsymbol{u}_2$. The intersection $T_{0y} = T_y \cap \ker(\boldsymbol{\nabla}\mathrm{G})$ is one dimensional and $\hat{\boldsymbol{u}}_2$ is a basis of T_{0y}, that is, the 2D thermodynamic projector matrix takes the form:

$$\boldsymbol{P}(i,j) = \frac{1}{\boldsymbol{\nabla} G \hat{\boldsymbol{u}}_1^T} \left(\boldsymbol{\nabla} G_j \hat{\boldsymbol{u}}_{1i} \right) + \frac{1}{\hat{\boldsymbol{u}}_2 \boldsymbol{H} \hat{\boldsymbol{u}}_2^T} \left(\boldsymbol{H} \hat{\boldsymbol{u}}_2^T \right)_j \hat{\boldsymbol{u}}_{2i}, \tag{6.9}$$

where the vector $\hat{\boldsymbol{u}}_1$ is parallel to the hyperplane T_y, such that $\hat{\boldsymbol{u}}_1 \boldsymbol{H} \hat{\boldsymbol{u}}_2^T = 0$. If (6.8) is not of full rank, we take $\hat{\boldsymbol{u}}_2 = \boldsymbol{u}_2$ and $\hat{\boldsymbol{u}}_1$ parallel to T_y with $\hat{\boldsymbol{u}}_1 \boldsymbol{H} \hat{\boldsymbol{u}}_2^T = 0$.

6.3.2. Invariant grids by Newton method

For the case under study, a 1D QE-grid was constructed as first approximation of the one dimensional slow invariant manifold, where the vector $\boldsymbol{m}_1$ appearing in (5.1) was taken as the left eigenvector of the Jacobian $\boldsymbol{J}$ corresponding to the eigenvalue with the smallest absolute value at the steady state. Namely, the 1D spectral quasi equilibrium grid was computed.

The initial grid, as well as any subsequent grid, is parametrized by $\xi = \sum_{i=1}^{9} \boldsymbol{m}_{1i} c_i$. With the reference to the detailed system (1.7), the 1D SQEG was refined via the Newton method with incomplete linearization (2.19),

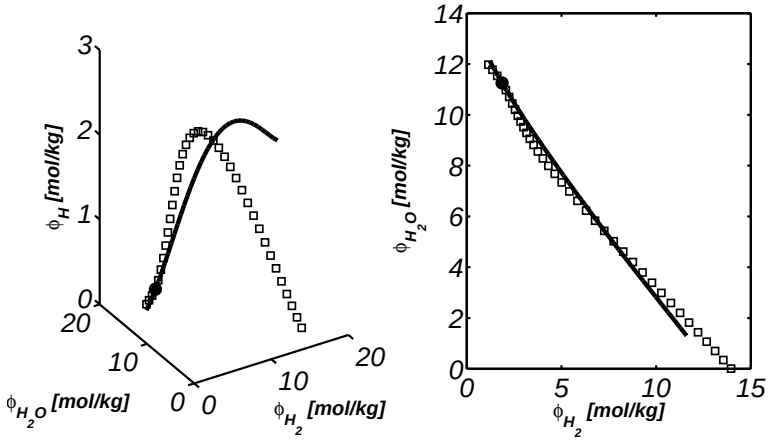

Figure 6.1.: Starting from the equilibrium point (filled circle), the 1D SQEG (bold line) was constructed via QEGA and refined via MIG to obtain the 1D invariant grid (squares).

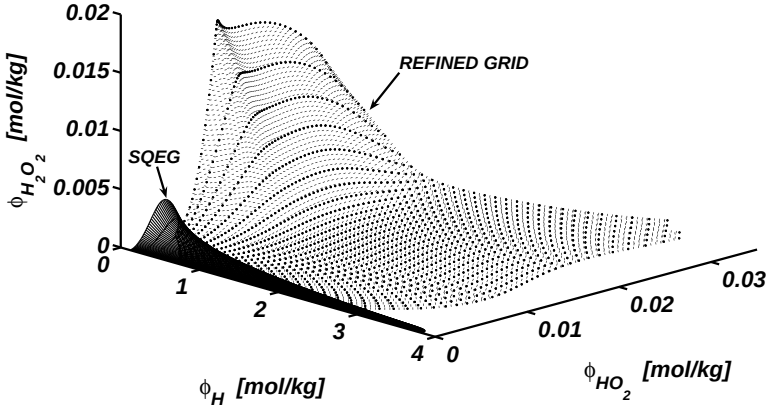

Figure 6.2.: The 2D SQEG (continuous lines) is constructed and refined via MIG iterations. A projection of an intermediate refined grid (dots) is shown.

till the dimensionless ratio between the Euclidean norm of the defect of invariance and the vector field $\|\boldsymbol{\Delta}\|/\|\boldsymbol{f}\|$ became smaller than 0.001 at every grid node. The results are shown in Fig. 6.1. Here, it is worth mentioning that the SQEG and the invariant grid are in a good agreement in the neighborhood of the steady state. Moreover, the SQEG also proves to be a good approximation with respect to the major species in the full concentration space (as can be seen by its projection in the ϕ_{H_2}-ϕ_{H_2O} subspace, Fig. 6.1).

A 2D SQEG was also constructed, implementing the straightforward extension of section 5.5.1, where the two vectors $\boldsymbol{m}_1$ and $\boldsymbol{m}_2$ were chosen as the two left eigenvectors of the Jacobian matrix corresponding to the two smallest eigenvalues (in absolute value) evaluated at the equilibrium point. The two reduced variables associated with the grid nodes were $\xi^1 = \sum_{i=1}^{9} \boldsymbol{m}_{1i} c_i$ and $\xi^2 = \sum_{i=1}^{9} \boldsymbol{m}_{2i} c_i$. The 2D SQEG was again refined using (2.19) until the threshold value 0.001 for the ratio $\|\boldsymbol{\Delta}\|/\|\boldsymbol{f}\|$ was reached. If the defect of invariance at a refined node kept increasing after five iterations, the new node was discarded. The 2D SQEG accurately describes the invariant grid only near the equilibrium point, and thirty Newton iterations were required during the refinement process.

Figure 6.2 shows both the initial SQEG grid (solid lines) and its refinement after three iterations. Finally, the projection of the final 2D invariant grid onto the ϕ_H-ϕ_{HO_2}-$\phi_{H_2O_2}$ subspace is shown in Fig. 6.3.

6.3.3. Reduced system

Once the invariant grid is obtained, it can be stored in tables and used for the time integration of the reduced system. Indeed, let us assume that the 1D invariant grid $\mathcal{G}_{inv}$ is constructed and the vector $\boldsymbol{m}$ is chosen in such a way that the parameter $\xi = \sum_{i=1}^{9} \boldsymbol{m}_i c_i$ is uniquely associated with every point of $\mathcal{G}_{inv}$. The original system (1.7) reduces to a single equation:

$$\frac{d\xi}{dt} = \boldsymbol{m}\boldsymbol{P}\boldsymbol{f}\left(\xi\right). \tag{6.10}$$

When a 2D reduced description is adopted, two vectors are introduced ($\boldsymbol{m}_1$, $\boldsymbol{m}_2$) so that the new variables are $\xi^1 = \sum_{i=1}^{9} \boldsymbol{m}_{1i} c_i, \xi^2 = \sum_{i=1}^{9} \boldsymbol{m}_{2i} c_i$ and the reduced system reads:

$$\begin{aligned} d\xi^1/dt &= \boldsymbol{m}_1\boldsymbol{P}\boldsymbol{f}\left(\xi^1, \xi^2\right), \\ d\xi^2/dt &= \boldsymbol{m}_2\boldsymbol{P}\boldsymbol{f}\left(\xi^1, \xi^2\right). \end{aligned} \tag{6.11}$$

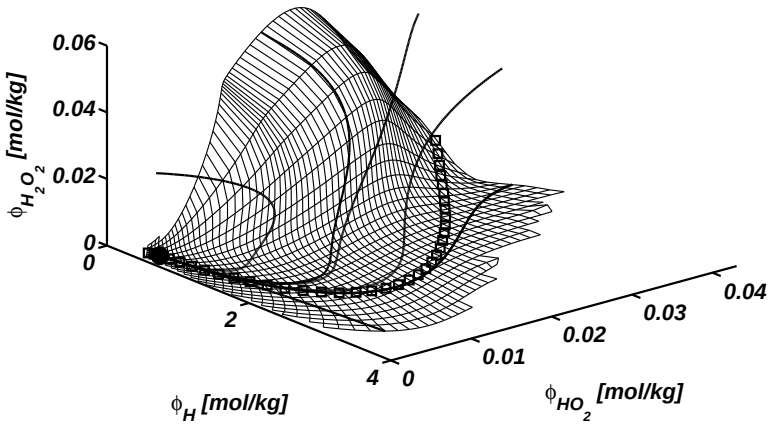

Figure 6.3.: The 2D invariant grid (thin lines) computed by refining the 2D SQEG. The 1D invariant grid (squares) and sample solution trajectories (bold lines) are reported.

Notice that, for the dependence of the right-hand side of the above system on the reduced variables is not explicitly known, a proper look-up table is needed during time integration of (6.10) or (6.11). In other words, a continuation procedure of the approximate invariant manifold from the discrete grid has to be implemented. In the case under study, the reduced variables of the 2D invariant grid were chosen according to the SQEG parameterization, and the continuation of the invariant manifold from a generic 4-node cell of the invariant grid $\mathcal{G}_{inv}$ was obtained by linear interpolation.

Since the chosen parameterization of $\mathcal{G}_{inv}$ leads to a non-regular Cartesian grid in the parameter space, the 4-node cell was mapped to a standard square where a bi-variate linear interpolation was used to reconstruct the point on the SIM. The system (6.11) was solved by an explicit 4-th order Runge-Kutta scheme with the time step $\delta t = 10^{-8}$ s. Results were compared with the solution of the detailed system (1.7), obtained with the same ODE solver. However, in the latter case the time step needed was one order of magnitude smaller due to the stiffness of the original system. The comparison, shown in Fig. 6.4, indicates both that (6.11) is less stiff than (1.7) and that a linear interpolation on the 2D invariant grid in Fig.

6.3 delivers an excellent approximation of the corresponding slow invariant manifold. The reduction in stiffness can be also observed in Fig. 6.5, where the six non-trivial eigenvalues of the Jacobian along the solution trajectory are reported: since the inverse of the eigenvalues provides an estimate of the timescales of the chemical process, in our case the fastest dynamics presents a characteristic time of the order of 10^{-9} s.

Results in Fig. 6.4 were compared on the basis of the relative deviation of the reduced solution from the detailed one averaged over the integration interval. The maximum error was found to be around 2% for the evolution of $\phi_{H_2O_2}$, while for the remaining species the mean relative deviation was below 1%.

6.3.4. Summary of MIG

In this section, we summarize and further illustrate all the steps involved in the application of the presented methodology. Implementation of the MIG proceeds following four steps: construction of the initial grid; grid refinement; parameterization and tabulation; integration of the reduced system.

As illustrated in chapter 5, the initial grid is constructed by using the QEG-algorithm (QEGA), which provides a q-dimensional array for each species involved in the detailed mechanism, where q denotes the dimension of the manifold of the reduced description. For the case considered in this chapter, the 2D initial grid (SQEG) is stored in nine 2D-arrays $\boldsymbol{X}_1, \ldots, \boldsymbol{X}_9$ collecting the different components at each grid point. In other words, a given node $\boldsymbol{c}$ of a 2D grid is identified by a pair of indexes (j, k) such that $\boldsymbol{c} = (\boldsymbol{X}_1(i,j), \ldots \boldsymbol{X}_9(i,j))$.

During the second step, those arrays are iteratively updated by solving the system (2.19) at each grid node, where the Jacobian matrix $\boldsymbol{J}$ is computed as shown in the Appendix B, and the projector $\boldsymbol{P}$ takes the form (6.9) with the tangent vectors $\boldsymbol{u}_1$ and $\boldsymbol{u}_2$ approximated via finite differences. For instance, in the case of second order finite differences, the i-th components of $\boldsymbol{u}_1$ and $\boldsymbol{u}_2$ read $(\boldsymbol{X}_i(j+1,k) - \boldsymbol{X}_i(j-1,k))/2\Delta\xi^1$ and $(\boldsymbol{X}_i(j,k+1) - \boldsymbol{X}_i(j,k-1))/2\Delta\xi^2$, respectively. The grid refinement is terminated when the Euclidean norm of the defect of invariance, compared to the norm of the vector field, at every node is less than a given threshold. For the sake of clarity, we report the general algorithm below:

1. *Start from full system (1.7) of dimension n*

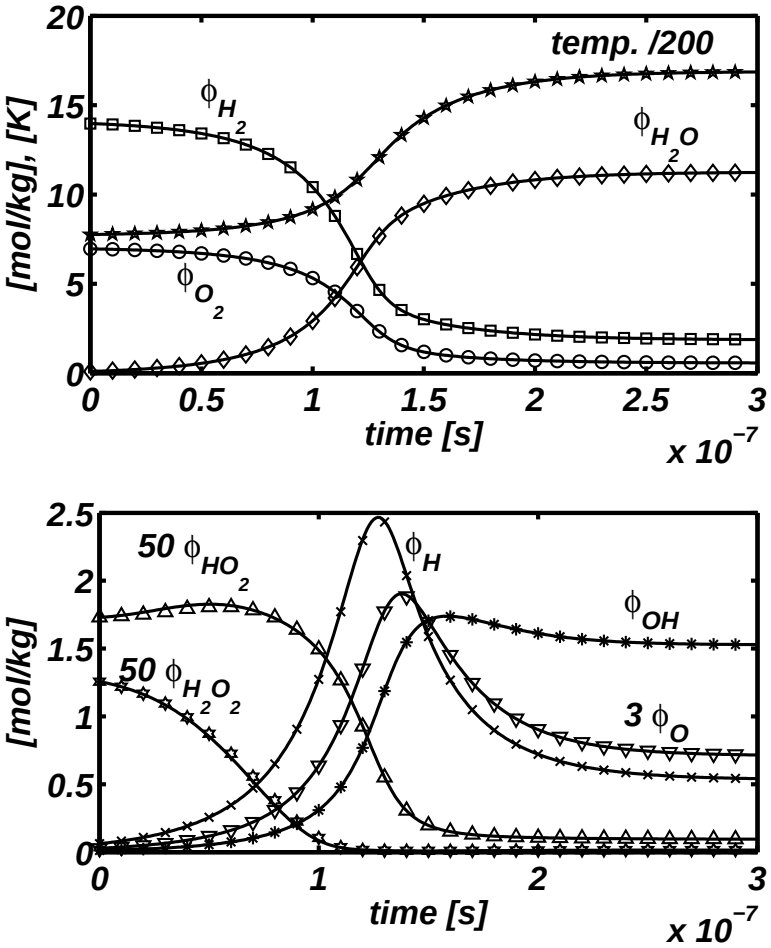

Figure 6.4.: Starting from a point located on the 2D invariant grid, the reduced system was integrated by using an explicit Runge-Kutta 4-th order scheme with a fixed time step $\delta t = 10^{-8}$ s (symbols). Continuous lines represent the solution of the detailed model.

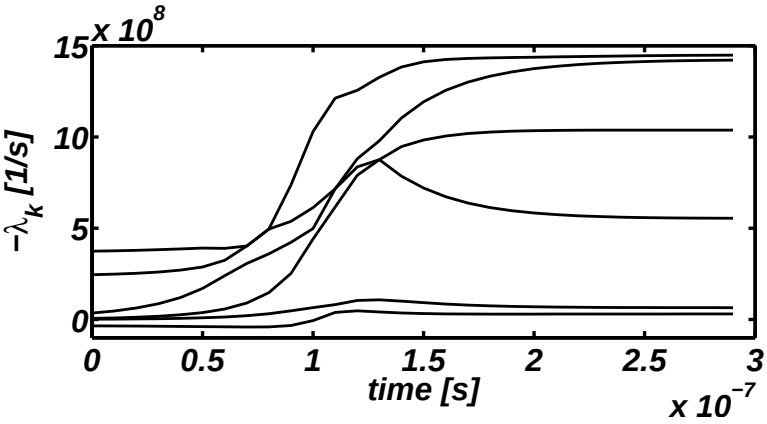

Figure 6.5.: Six eigenvalues of Jacobian along the solution trajectory illustrated in Fig. 6.4.

2. *Find steady state and the two slowest left eigenvectors of* $\boldsymbol{J}$ *at steady state*
3. *Construct initial grid (SQEG) according to algorithm of chapter 5*
4. *Compute* $\{\boldsymbol{u}_1, \boldsymbol{u}_2\}$, $\boldsymbol{\nabla} G$, $\boldsymbol{H}$, $\boldsymbol{J}$, $\boldsymbol{f}$ *and vectors* $\{\boldsymbol{b}_i\}$ *at each node (section (2.3.4))*
5. *Construct thermodynamic projector from (6.9)*
6. *Correct each node* $\boldsymbol{c}$ *solving (2.19) for* δ_i*:* $\boldsymbol{c}^{corr} = \boldsymbol{c} + \delta\boldsymbol{c}$, $\delta\boldsymbol{c} = \sum \delta_i \boldsymbol{b}_i$
7. *Compare norm of invariance defect vs vector field:* $\|\boldsymbol{\Delta}\|/\|\boldsymbol{f}\|$
8. *if* $\|\boldsymbol{\Delta}\|/\|\boldsymbol{f}\|$ *is larger than a threshold then go to (4).*

The 2D invariant grid is stored in the updated arrays, and it can be parameterized by introducing two additional 2D-arrays $\boldsymbol{\xi}^1$, $\boldsymbol{\xi}^2$ such that:

$$\boldsymbol{\xi}^1 = \sum\nolimits_{i=1}^{9} \boldsymbol{m}_{1i} \boldsymbol{X}_i, \quad \boldsymbol{\xi}^2 = \sum\nolimits_{i=1}^{9} \boldsymbol{m}_{2i} \boldsymbol{X}_i, \tag{6.12}$$

where the two vectors $\boldsymbol{m}_1$ and $\boldsymbol{m}_2$ define a parameterization of the invariant grid. Generally, the pre-computed look up tables do not lay on a regular Cartesian grid. In other words, the four points

$$A \equiv \left[\xi^1(j,k), \xi^2(j,k)\right], \quad B \equiv \left[\xi^1(j+1,k+1), \xi^2(j+1,k+1)\right],$$
$$C \equiv \left[\xi^1(j,k+1), \xi^2(j,k+1)\right], \quad D \equiv \left[\xi^1(j+1,k), \xi^2(j+1,k)\right],$$

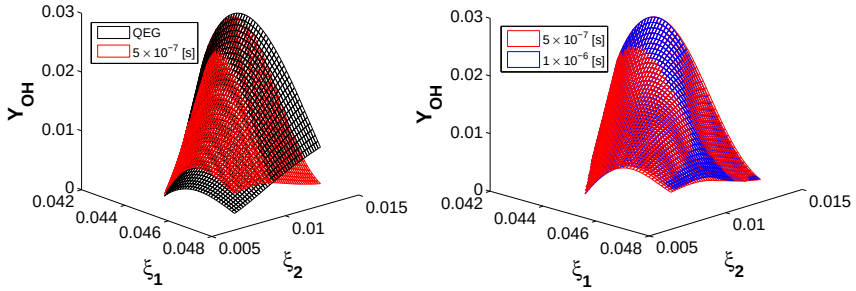

Figure 6.6.: Y_{OH} coordinate: refinement of a quasi equilibrium grid via relaxation of the film equation.

are the corners of a trapezium in the plane of the reduced variables ξ^i. Points of the SIM corresponding to a pair of parameters (ξ^1, ξ^2) inside the latter trapezium can be reconstructed by a coordinate transformation which maps the trapezium into a square centered at the origin whose edge length is 2. Assume that $(\bar{\xi}^1, \bar{\xi}^2)$ is the transformed pair of parameters, bi-variate interpolation is straightforward by computing for each corner the weight:

$$\iota_i = \left(1 \pm \bar{\xi}^1\right)\left(1 \pm \bar{\xi}^2\right)/4, \quad i = A, B, C, D.$$

Any tabulated quantity $\mathcal{Q}$ associated with the parameter pair (ξ^1, ξ^2) is reconstructed as follows:

$$\mathcal{Q}\left(\xi^1, \xi^2\right) = \iota_A \mathcal{Q}_A + \iota_B \mathcal{Q}_B + \iota_C \mathcal{Q}_C + \iota_D \mathcal{Q}_D. \tag{6.13}$$

Notice that the right-hand side of the reduced system (6.11) is also pre-computed and stored in separate arrays. Therefore, during the last MIG step, the system (6.11) can be integrated with the help of the interpolation scheme (6.13).

Finally, it is worth pointing out the computational effort needed for the construction of the invariant grid. For the case under study, the initial 2D SQEG contains 1650 nodes. It was generated in 6 seconds and refined in about 10 minutes on a single processor 3 GHz using a Matlab code.

6.4. Relaxation methods

In section 6.3, making use of the Newton method presented in section 2.3.4, we construct a reduced description of an isolated homogeneous reactor. Below, we want to discuss further the construction of invariant grids via relaxation of the film equation (2.5), when starting from an initial non-invariant grid.

In other words, here we only focus on an alternative approach to the geometry of the model reduction (construction of the invariant grid by refinement), while the dynamics of the reduced system can be still treated as illustrated above in section 6.3.3.

In particular, we consider adiabatic hydrogen-air reacting mixtures, under fixed pressure $p = 1bar$ and mixture averaged enthalpy $h = 1[MJ/kg]$, at stoichiometric proportion and described by the detailed mechanism of the Appendix D.

To this end, a two-dimensional quasi equilibrium grid, corresponding to the vector pair $(\boldsymbol{m}_1, \boldsymbol{m}_2)$:

$$\begin{aligned} \boldsymbol{m}_1 &= \left(\tfrac{1}{W_{H_2}}, \tfrac{1}{W_{N_2}}, \tfrac{1}{W_H}, \tfrac{1}{W_O}, \tfrac{1}{W_{OH}}, \tfrac{1}{W_{O_2}}, \tfrac{1}{W_{H_2O}}, \tfrac{1}{W_{HO_2}}, \tfrac{1}{W_{H_2O_2}}\right), \\ \boldsymbol{m}_2 &= \left(0, 0, 0, \tfrac{1}{W_O}, \tfrac{1}{W_{OH}}, 0, \tfrac{1}{W_{H_2O}}, 0, 0\right), \end{aligned} \tag{6.14}$$

is chosen, and constructed on a regular Cartesian grid following the procedure of section 5.8, where the generic phase-space state $\boldsymbol{\psi}$ is expressed in terms of mass fractions Y_i. Details about the manifold parameterization given by (6.14) are discussed in section 7.4.1.

In Fig. 6.6, we show the relaxation of the film equation (2.5), starting from a two-dimensional quasi equilibrium grid (QEG), where (2.5) is solved using an explicit Runge-Kutta 4-th order scheme (RK4) with the time step $\delta t = 1 \times 10^{-8}[s]$. More explicitly, at a given time step the vector field $\boldsymbol{f}$ is approximated by the RK4 slope, and every grid node is shifted by the amount $(\boldsymbol{f} - \boldsymbol{P}\boldsymbol{f})\delta t$, where $\boldsymbol{P}$ is explicitly computed at the current time step.

6.4.1. Relaxation Redistribution method

The rationale behind the relaxation methods can be understood keeping in mind the picture reported in Fig. 6.7. Let an initial grid $\mathcal{G}_0$ be given as an

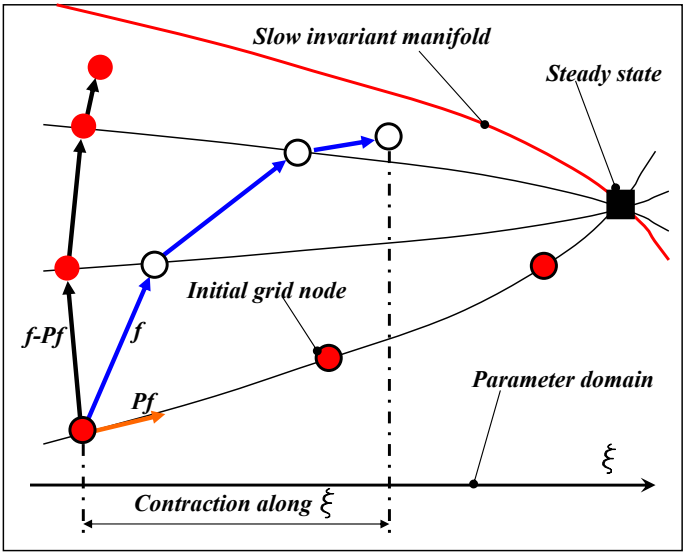

Figure 6.7.: Relaxation of the film equation of dynamics $\boldsymbol{f}$.

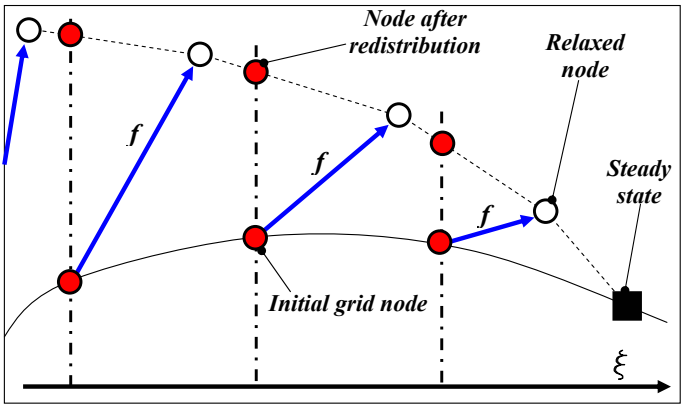

Figure 6.8.: One step of the relaxation redistribution method.

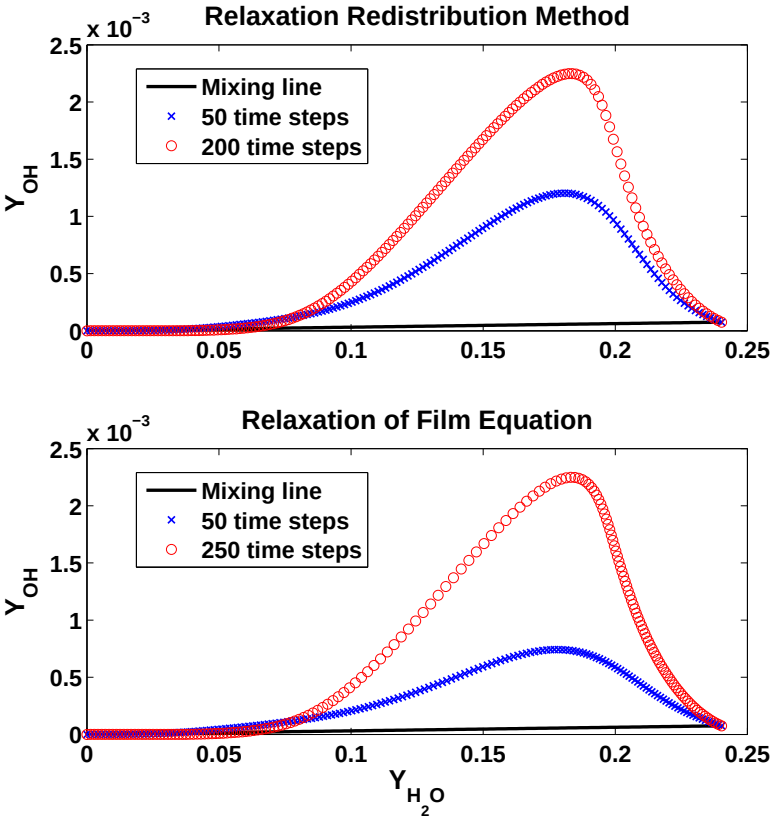

Figure 6.9.: Relaxation redistribution method using $\delta t = 8 \times 10^{-8}$. Relaxation of the film equation using $\delta t = 5 \times 10^{-8}$. The numerical solver is Runge-Kutta 4-th order in both cases.

approximation of the slow invariant manifold. If this grid is not invariant, an arbitrary node of $\mathcal{G}_0$ relaxes to the slow invariant manifold under the dynamics of the vector field of motion $\boldsymbol{f}$ (e.g. right-hand side of the kinetic equations (1.9)). Since we assume that the detailed system (1.9) naturally evolves towards a slow invariant manifold, a short time relaxation, from all nodes taken as initial conditions of (1.9), makes the entire grid move to a new configuration, which is expected to lie closer to the slow invariant manifold. In other words, the invariance defect is expected to decay in time at any grid node.

This procedure can be iterated in order to construct better approximations of the slow manifold. However, due to the presence of the slow dynamics, the grid constantly undergoes a contraction which, as time passes by, leads all nodes closer and closer to the steady state (see the open circles in Fig. 6.7).

On the other hand, defining a projector matrix $\boldsymbol{P}$, at a node of $\mathcal{G}_0$, enables us to split the motion vector $\boldsymbol{f}$ into a slow part $\boldsymbol{Pf}$ (along the grid) and its fast complement $\boldsymbol{f} - \boldsymbol{Pf}$ (transversal to the grid). Hence, relaxation of the initial grid $\mathcal{G}_0$, under the transversal movement $\boldsymbol{f} - \boldsymbol{Pf}$, prevents the nodes from collapsing on the steady state. Namely, a node refinement follows the black arrows in Fig. 6.7. Moreover, The slow invariant manifold is a fixed point of such a relaxation, which can be terminated as soon as the right-hand side of the film equation (2.5) becomes sufficiently small.

In the present work, we introduce an alternative relaxation method for grid refinements which can be also implemented as described in the following. For illustration purposes, we refer to the one-dimensional initial grid $\mathcal{G}_0$, schematically drawn in Fig. 6.8. Let $\mathcal{G}_0$ be chosen regular in terms of the parameter ξ. Moreover, we assume that $\mathcal{G}_0$, along with any further refined grid, can be expressed as a unique mapping of the parameter ξ, $F(\xi)$, and there exists the invariant manifold of slow motions.

Let a numerical scheme (Euler, Runge-Kutta, etc.) be chosen for solving the system of kinetic equations, and let all grid nodes relax towards the slow invariant manifold (SIM) under the detailed dynamics $\boldsymbol{f}$ during one time step. As pointed out above, the fast component of $\boldsymbol{f}$ brings a grid node closer to the SIM while, at the same time, the slow component causes a contraction towards the steady state. As a result, the grid becomes dense in a neighborhood of the steady state and coarse far from it, when keeping relaxing. Nevertheless, the slow motion can be neutralized by a node redistribution after the grid relaxation. In other words, as illustrated in Fig. 6.8, the relaxed states are redistributed on a regular grid in terms

of the parameter ξ via linear interpolation, which is preferred in order to fulfill automatically the linear atom constraints (1.11). Finally, if there is contraction at the grid boundary, a linear extrapolation can be performed whenever the extrapolated node belongs to the admissible phase-space (positive concentrations).

Notice that all intermediate grids are, by construction, regular in terms of ξ and, in the case of an invariant grid, the overall effect due to relaxation and redistribution is null. Therefore, a measure of the invariance defect is now given by the overall motion of a node (relaxation + redistribution) compared to the relaxation. An invariant grid represents the *stable* fixed solution of the described procedure, whose name is *relaxation redistribution method* (RRM).

It is worthy stressing that RRM does not make explicit use of a projector $\boldsymbol{P}$ on the tangent space of $\mathcal{G}_0$. On the contrary, since the role of $\boldsymbol{P}$ is now played by the redistribution sub-step after the relaxation, $\boldsymbol{P}$ can be considered implicit. Namely, unlike formulas (2.23) and (2.25), the choice of the time step for RRM is not restricted by the Courant instability discussed in section 2.3.6.

For illustration purposes, in Fig. 6.9 we consider the refinement of a fine one-dimensional grid (170 nodes), in the case of a homogeneous hydrogen-air mixture, under fixed pressure $p = 1bar$ and enthalpy $h = 2.8[kJ/kg]$. Here, every grid is parametrized in terms of the water mass fraction $\xi = Y_{H_2O}$. Starting from the one-dimensional linear manifold, connecting the unburned mixture state and the steady state (mixing line), RRM is implemented in combination with an explicit Runge-Kutta 4-th order solver (RK4), where the time step is chosen: $\delta t = 8 \times 10^{-8}[s]$. On the other hand, due to Courant instability, when refining the same grid by relaxation of the film equation and RK4, the time step must be decreased down to $\delta t = 5 \times 10^{-8}[s]$.

The two-dimensional quasi equilibrium grid, constructed under the conditions of section 6.4, is now refined using the relaxation redistribution method in combination with the RK4 scheme and $\delta t = 1 \times 10^{-8}[s]$ (see Fig. 6.10). On the basis of these preliminary results, we can argue that the RRM is consistent with other methods based on the explicit integration of the film equation.

Moreover, a different setup is also considered in Fig. 6.11. Here we still use an explicit RK4 scheme with $\delta t = 1 \times 10^{-8}[s]$ during the relaxation

step and, as shown by the sample trajectories in 6.11(c), the RRM does construct the slow invariant manifold with remarkable accuracy.

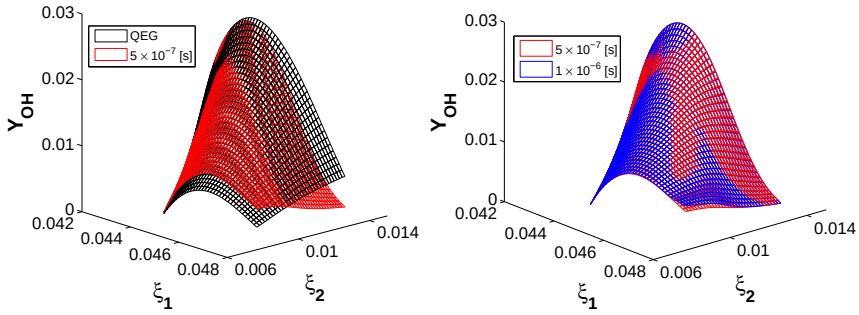

Figure 6.10.: Y_{OH} coordinate: refinement of a two-dimensional quasi equilibrium grid via the relaxation redistribution method.

6.5. Conclusions

In this chapter, the method of invariant grids is applied for the first time to reduce a detailed hydrogen mechanism in non-isothermal conditions. The two dimensional reduced model was then compared to the detailed one in an adiabatic constant volume reactor with H_2-air in stoichiometric proportions.

The spectral quasi equilibrium grid (SQEG) [15] proves suitable for providing the iterative procedure with an initial collection of points (initial grid). The one- and two-dimensional SQEG grids describe quite well the dynamics of the major species, but they are not able to capture the correct evolution of some of the radicals. Therefore, several MIG iterations are needed in order to construct accurate 1D and 2D discrete approximation of the slow invariant manifold (SIM), providing the reduced description of the original nine-dimensional system. A bi-variate linear interpolation was used to reconstruct the SIM from the invariant grid during the time integration of the reduced system. As indicated by the reduction in the number of time steps needed to integrate the reduced system by an order of magnitude, the stiffness is significantly reduced and the two-dimensional model proves to be an excellent approximation of the detailed dynamics.

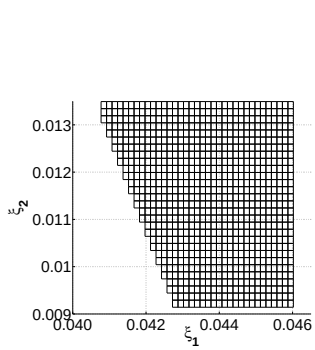

(a) `Grid`

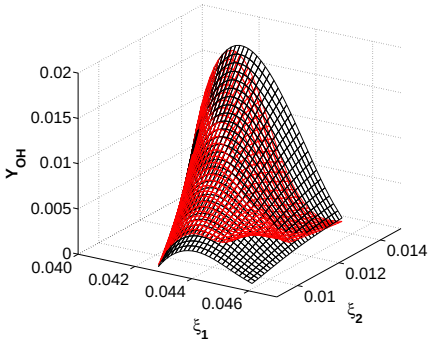

(b) `Refinement`

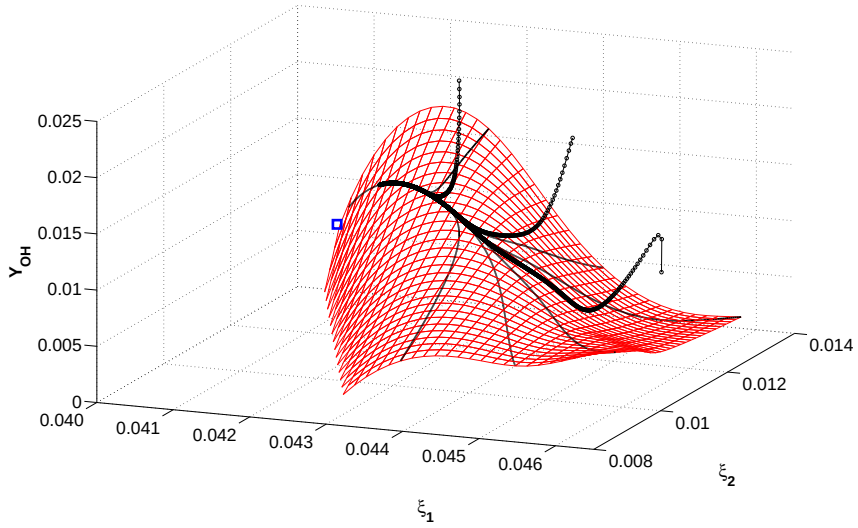

(c) `Trajectories`

Figure 6.11.: Stoichiometric mixture of hydrogen and air under fixed $\bar{h} = 100[kJ/kg]$ and $p = 1bar$. (a)-(b): the RRM is used to refine a QEG (black) parameterized by $0.041 < \xi_1 < 0.046$ and $0.0091 < \xi_2 < 0.0135$. (c): the relaxed grid is reported in red and both trajectories along it (thin continuous line) and trajectories attracted to it (circles) are shown. A blue square denotes the steady state.

7. Coupling within the lattice Boltzmann method

7.1. Introduction

In the present chapter, we intend to investigate on the potential of using reduced kinetics within the lattice Boltzmann framework: to this end, we consider a reduced description (2 degrees of freedom) of a detailed mechanism for reactive mixtures of hydrogen-air, obtained by the method of invariant grids.

The chapter is organized as follows. In section 7.2, we briefly outline the adopted reduction technique. The detailed lattice Boltzmann scheme for simulating reactive flows and the suggested coupling with reduced chemistry are presented in section 7.3. The validation studies are presented in section 7.4 and 7.5, where we consider the propagation of one-dimensional flames in premixed mixtures of hydrogen-air, and two-dimensional laminar premix counterflow flames. Finally, conclusions are drawn in section 7.6.

7.2. Model reduction technique

In our approach, we first seek the reduced description of a batch reactor under fixed pressure p and mixture-averaged enthalpy $\bar{h}$. The construction of the reduced model follows two steps:

1. construction of a quasi equilibrium grid using the algorithm described in chapter 5,

2. refinement of a quasi equilibrium grid using the method of invariant grids (see chapters 4 and 6).

The slow dynamics of (1.9) takes place along the invariant grid and obeys the reduced q-dimensional system (q is the dimension of the invariant grid),

$$\frac{d\xi^i}{dt} = \boldsymbol{m}_i \boldsymbol{P} \boldsymbol{f}, \quad i = 1, \ldots, q. \tag{7.1}$$

Once the invariant grid is obtained, it can be stored in tables for a later use in the flow solver. The grid parameterization is performed by attaching, to every grid state, the q quantities ξ^j, evaluated according to (5.1). The coordinates at each grid point, the corresponding temperature, the right-hand side of (7.1) and all components of the projected vector field $\boldsymbol{P}\boldsymbol{f}$ are stored in q-dimensional arrays and can be accessed through the grid parameters ξ^j.

Remark: Along invariant grids, thermodynamic projector performs fast-slow motion decomposition of the vector field $\boldsymbol{f}$. In other words, the fast component of $\boldsymbol{f}$ belongs to the null space of the matrix $\boldsymbol{P}$ discussed in section 6.3.1. For this reason, the projector in (7.1) must be thermodynamic, whereas for the refinement procedure we may use a different projector matrix.

7.3. Lattice Boltzmann method for reactive flows

We consider here the simplest lattice Boltzmann formulation suitable for simulations of combustion. To this end, following the suggestion of Yamamoto et al [69], reactive flows can be simulated with the lattice Boltzmann (LB) method as reported in the next section 7.3.1.

Note, however, that more elaborate and complete LB models for mixtures [4, 5] and compressible flows [55] shall be taken into account in the near future, too.

7.3.1. Original model

In the following, we consider the 1D 3-bit lattice (Fig. 3.1). However, the application of the illustrated methodologies to a larger lattice is straightforward. We assume that the flow field is not affected by the chemical reaction, transport coefficients are constant and Fick's law applies to the

diffusion. Therefore, the background flow is treated as one-component medium whose pressure populations evolution is discussed in chapter **3**, and obey the equations (3.1). Let T_0 be a reference temperature, the evolution equations for temperature and concentration of species i are written as

$$\begin{aligned}\tilde{T}_\alpha\left(\boldsymbol{x}+\boldsymbol{e}_\alpha, t+\delta t\right)-\tilde{T}_\alpha\left(\boldsymbol{x}, t\right) &= -\tfrac{1}{\tau_T}\left[\tilde{T}_\alpha\left(\boldsymbol{x}, t\right)-\tilde{T}_\alpha^{eq}\left(\tilde{T}, \boldsymbol{u}\right)\right]+w_\alpha Q_T,\\ Y_{i\alpha}\left(\boldsymbol{x}+\boldsymbol{e}_\alpha, t+\delta t\right)-Y_{i\alpha}\left(\boldsymbol{x}, t\right) &= -\tfrac{1}{\tau_{Y_i}}\left[Y_{i\alpha}\left(\boldsymbol{x}, t\right)-Y_{i\alpha}^{eq}\left(Y_i, \boldsymbol{u}\right)\right]+w_\alpha Q_{Y_i},\end{aligned} \tag{7.2}$$

where

$$\tilde{T}=T/T_0=\sum_\alpha T_\alpha, \quad Y_i=\sum_\alpha Y_{i\alpha}, \tag{7.3}$$

and the equilibrium populations $\tilde{T}_\alpha^{eq}$, $Y_{i\alpha}^{eq}$ are expressed as in (3.4), after replacing p with $\tilde{T}$ and Y_i respectively. Let t_0 be a factor for converting physical time into LB time units: $(t)_{LB}=(t)_{phys}\Big/t_0$, the source terms take the explicit form

$$Q_T=\frac{1}{T_0}\left(\sum_{i=1}^{n}\frac{\dot{\omega}_i W_i}{\bar{\rho}\bar{C}_p}h_i\right)t_0\delta t,\; Q_{Y_i}=\frac{\dot{\omega}_i W_i}{\bar{\rho}}t_0\delta t, \tag{7.4}$$

where $\bar{C}_p$ is the mean specific heat of the mixture per unit mass at constant pressure. The thermal diffusivity κ and diffusion coefficient D_i of species i are related to the relaxation parameters as follows

$$\kappa=\frac{2\tau_T-1}{6}\delta t, \quad D_i=\frac{2\tau_{Y_i}-1}{6}\delta t. \tag{7.5}$$

7.3.2. Discussion of the model

In the above sections, we briefly review the lattice Boltzmann model for reactive flows originally presented in [69], where more details can be found. However, it is worth reporting here the basic assumptions of the model:

- The chemical reaction does not affect the flow field in an incompressible model.
- The transport properties are constant.
- The diffusion follows the Fick's law.
- Viscous energy dissipation and radiative heat loss are neglected.

It is worth noticing that, the LB equation (3.1) for pressure density functions p_α recovers, in the low-Mach number regime, the incompressible Navier-Stokes equations, which can be written as follows (in the absence of body forces):

$$\begin{aligned} &\partial_j u_j = 0 \\ &\partial_t u_i + u_j \partial_j u_i = -\tfrac{1}{\bar{\rho}} \partial_i p + \partial_j \left(\nu \partial_j u_i \right). \end{aligned} \tag{7.6}$$

Here, ∂_t and ∂_j denote partial derivatives with respect to time and the jth spacial direction respectively, while Einstein summation convention is adopted for j. Therefore, pressure and density only have small fluctuations around their reference values, and compressibility effects are not taken into account in the adopted model. The above assumptions are used for the sake of simplicity, and the methodology suggested in this chapter can be still used, in combination with more recent LB models where compressibility is included as well (see, e.g., [13, 14]).

A detailed discussion on fundamental aspects of the lattice Boltzmann equations (3.1) and (7.2), derivation of the equilibrium populations (3.4), relations between transport coefficients and relaxation parameters (e.g. (7.5)) can be found in [11, 64]. Moreover, the lattice Boltzmann equations (7.2) recover the following partial differential equations (PDE) [69]:

$$\partial_t \bar{h} + u_j \partial_j \bar{h} = \partial_j \left(\kappa \partial_j \bar{h} \right) + \sum_{i=1}^{n} \frac{\dot{\omega}_i W_i}{\bar{\rho}} h_i, \tag{7.7}$$

and

$$\bar{\rho} \left(\partial_t Y_i + u_j \partial_j Y_i \right) = \partial_j \left(\bar{\rho} D_i \partial_j Y_i \right) + \dot{\omega}_i W_i, \tag{7.8}$$

which account for the conservation of energy and a generic species i, respectively.

7.3.3. Modified algorithm

The slow manifold, constructed by the procedure of section 7.2, is invariant under the dynamics of the system (1.9), which only accounts for the chemical source terms. Since, at each lattice point of the domain, the LB equations also contain advection and diffusion terms, the computed grid is not invariant with respect to the LB dynamics (see Fig. 7.1). On the other hand, the time scales associated with chemical reactions are typically faster than the time scales of the flow. In this case, we can still use the chemical slow invariant manifold for speeding up computations. To this end, we suggest to modify the LB algorithm of section 7.3.1 as follows:

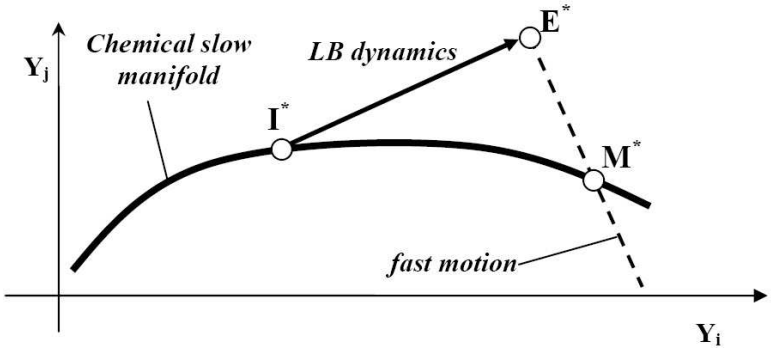

Figure 7.1.: Starting from an initial state I^*, the LB dynamics runs out of the chemical slow manifold.

- COLLISION

$$\begin{aligned} \tilde{h}^*_\alpha(\boldsymbol{x},t) &= \tilde{h}_\alpha(\boldsymbol{x},t) - \tfrac{1}{\tau_T}\left[\tilde{h}_\alpha(\boldsymbol{x},t) - \tilde{h}^{eq}_\alpha(h,\boldsymbol{u})\right], \\ \tilde{Y}_{i\alpha}(\boldsymbol{x},t) &= Y_{i\alpha}(\boldsymbol{x},t) - \tfrac{1}{\tau_{Y_i}}\left[Y_{i\alpha}(\boldsymbol{x},t) - Y^{eq}_{i\alpha}(Y,\boldsymbol{u})\right], \end{aligned} \tag{7.9}$$

- STREAMING + REACTION

$$\begin{aligned} \tilde{h}_\alpha(\boldsymbol{x}+\boldsymbol{e}_\alpha, t+\delta t) &= \tilde{h}^*_\alpha(\boldsymbol{x},t) + w_\alpha Q_h, \\ \tilde{Y}^*_{i\alpha}(\boldsymbol{x}+\boldsymbol{e}_\alpha, t+\delta t) &= \tilde{Y}_{i\alpha}(\boldsymbol{x},t) + w_\alpha Q_{Y_i}, \end{aligned} \tag{7.10}$$

- POPULATION CORRECTION

$$Y_{i\alpha}(\boldsymbol{x},t) = Y^*_{i\alpha}(\boldsymbol{x},t) + \psi_{i\alpha}. \tag{7.11}$$

Here, we have reformulated the temperature evolution equations in terms of dimensionless enthalpy: $\tilde{h} = h/h_0$, with h_0 a reference enthalpy. Now, the equilibrium populations and the heat source term are given by

$$\begin{aligned} \tilde{h}^{eq}_\alpha &= w_\alpha \tilde{h}\left[1 + 3\left(\boldsymbol{e}_\alpha \boldsymbol{u}^T\right) + \tfrac{9}{2}\left(\boldsymbol{e}_\alpha \boldsymbol{u}^T\right)^2 - \tfrac{3}{2}\boldsymbol{u}^2\right], \\ Q_h &= \tfrac{1}{h_0}\left(\sum_{i=1}^{n} \tfrac{\dot{\omega}_i W_i}{\rho} h_i\right) t_0 \delta t. \end{aligned} \tag{7.12}$$

The correction step (7.11) can be understood by referring to Fig. 7.1. The LB dynamics brings the initial state I^* (located on the chemical slow manifold) to the point E^* (slightly off-manifold). Nevertheless, assuming that such a manifold is still attractive for the overall dynamics, E^* has to quickly relax to the point M^*. This relaxation occurs along the local fast direction, towards a manifold computed under the fixed mixture enthalpy

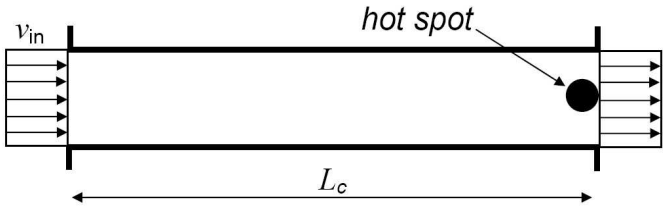

Figure 7.2.: Schematic representation of the 1D setup.

and element fractions (6.6) of state E^*. Let $(M^* - E^*)(i)$ be the i-th element of vector $(M^* - E^*)$, the correction terms are evaluated by the conditions

$$\begin{aligned} \sum_\alpha \psi_{i\alpha} &= (M^* - E^*)(i), \\ \sum_\alpha \boldsymbol{e}_\alpha \psi_{i\alpha} &= 0, \\ \sum_\alpha \boldsymbol{e}_\alpha^2 \psi_{i\alpha} &= 0, \end{aligned} \tag{7.13}$$

meaning that the zero-th order moment of $Y_{i\alpha}$ collapses from E^* to M^*, while none of other moments are affected. The conditions (7.13) are written for the 1D lattice of Fig. 3.1, but the same idea can be easily applied to a larger lattice, too.

The described procedure intends to get rid of the fast motions which require explicit solvers, like the LB method, to choose a small time step. Finally, notice that the source terms in (7.10) are now obtained from tables via interpolation.

7.4. Example: Plane flame propagation

In the following, we consider a stoichiometric hydrogen-air mixture entering an adiabatic channel (constant cross section) under room conditions ($T = 300K$, $p = 1bar$) at fixed velocity. A heat source is placed at the outlet in order to ignite the mixture (see Fig. 7.2). The background flow, from equation (3.1), keeps both pressure and velocity field uniform in space and time. A flame front is formed and propagates upstream since the laminar flame speed is larger than the flow velocity. For simplicity, we use the assumption of equal diffusivity D for all species and Lewis number $Le = \kappa/D = 1$. In this case, the mixture enthalpy $\bar{h}$ and the element fractions (6.6) remain constant throughout the domain, and the

reduced dynamics takes place along the invariant grid constructed under fixed pressure, mixture-averaged enthalpy at stoichiometric proportions. Notice however that, the latter assumption is not restricting and a generalization is obtained by extending the invariant grid with enthalpy and element fractions as additional degrees of freedom. On the other hand, in premixed systems, those quantities are conserved up to small fluctuations and, for such applications, the above approximation is often sufficient. Finally, in combustion problems with low-Mach number, the pressure p can be considered constant for most cases.

7.4.1. 2D reduced description

In our study, the detailed mechanism of Li et al [44] (9 species, 21 elementary reactions) for hydrogen combustion is considered, and we search for a reduced description with only two degrees of freedom. To this end, let us construct the 2D quasi equilibrium grid for a stoichiometric H_2-air mixture under fixed pressure $p = 1bar$ and enthalpy $\bar{h} = 2.8kJ/kg$, corresponding to the temperature $T_0 = 300K$ of a stoichiometric unburned mixture $H_2 + 0.5O_2 + 1.88N_2$. The vector set $\{\boldsymbol{m}_j\}$ in (5.1) is used to reparameterize the original variables Y_i in terms of new ones ξ^j, which are expected to follow a slow dynamics. Many suggestions for defining slow lumped variables in chemical kinetics are known in the literature, and for our purposes we use

$$\xi^1 = \sum_{i=1}^{9} \frac{Y_i}{W_i}, \quad \xi^2 = \frac{Y_O}{W_O} + \frac{Y_{OH}}{W_{OH}} + \frac{Y_{H_2O}}{W_{H_2O}}, \tag{7.14}$$

expressing the *total number of moles* (slow dissociation/recombination reactions) and *free oxygen* (slow reactions where the $O-O$ bond is broken), respectively (see, e.g., [65]). It is important to stress that, though the choice of $\{\boldsymbol{m}_j\}$ affects the accuracy of the quasi equilibrium grid in describing the slow manifold, the latter grid is anyway refined and the final result does not depend on the initial guess (see chapter 4). First of all, starting from the steady state, equations (5.45) are solved moving along ξ^1 with $\varepsilon_1 = 1.8 \times 10^{-4}$. Second, the grid is extended along ξ^2 with $\varepsilon_2 = \varepsilon_1$ and the construction ends when the concentration point, corresponding to the unburned mixture, is reached. The 2D quasi equilibrium grid, shown in Fig. 7.3, is relaxed to the invariant grid using equation (2.23), where the projector is thermodynamic and constructed according to (6.9). We have chosen the parameter $\delta t = 1 \times 10^{-8}$, and the convergence ratio between

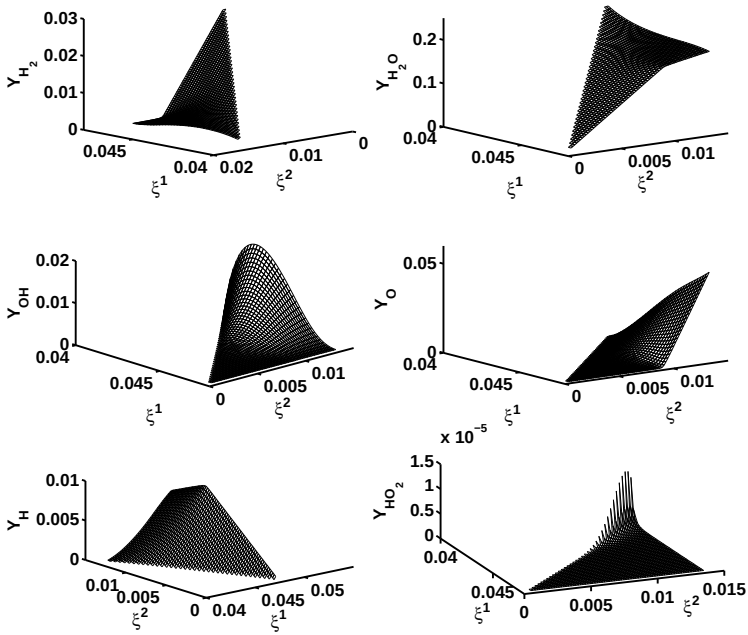

Figure 7.3.: Six coordinates of the 2D quasi equilibrium grid for stoichiometric H_2-air mixture, under $p = 1bar$ and $\bar{h} = 2.8kJ/kg$.

the invariance defect and the vector field was set $\|\boldsymbol{\Delta}\|/\|\boldsymbol{f}\| \leq 0.01$ at every grid node. Whenever the latter ratio keeps increasing while refining, the corresponding grid node is discarded. The 2D refined grid is shown in Fig. 7.4, and it is compared to the initial quasi equilibrium grid in Fig. 7.5. Notice that, in the low temperature region ($T < 800K$), the invariant grid is not convergent, meaning that a 2D description is not enough and the dimension of the slow invariant manifold is larger than two. The grid coordinates, the thermodynamic projection of the vector field $\boldsymbol{f}$ and the two parameters ξ^1, ξ^2 are redistributed on a regular Cartesian grid, stored in two dimensional arrays and each grid node is identified by an index pair (i, j). Any tabulated quantity $\mathcal{Q}$, associated with a generic parameter pair $\left(\xi^1, \xi^2\right)$, is reconstructed by linear bi-variate interpolation:

$$\mathcal{Q} = \iota_A \mathcal{Q}_A + \iota_B \mathcal{Q}_B + \iota_C \mathcal{Q}_C + \iota_D \mathcal{Q}_D, \tag{7.15}$$

where A, B, C, D are the grid nodes corresponding to (i, j), $(i+1, j)$, $(i, j+1)$, $(i+1, j+1)$, respectively, while ι_A, ι_B, ι_C, ι_D are the interpolation weights

$$\begin{aligned} \iota_A &= (1-\pi_1)(1-\pi_2), \quad \iota_B = \pi_1 (1-\pi_2), \\ \iota_C &= (1-\pi_1)\pi_2, \quad \iota_D = \pi_1 \pi_2, \end{aligned} \tag{7.16}$$

with $\pi_1 = \left(\xi^1 - \xi^1_A\right)/\left(\xi^1_B - \xi^1_A\right)$ and $\pi_2 = \left(\xi^2 - \xi^2_A\right)/\left(\xi^2_C - \xi^2_A\right)$. More details on multi-variate interpolation can be found in the Appendix C.

7.4.2. Setup and comparisons

In the simulation, the length of the adiabatic channel is $L_c = 5[mm]$, the inlet velocity $u_{in} = 1.2[m/s]$ and the species diffusivity $D = 5 \times 10^{-5} m^2/s$. All quantities given in physical units of time $[s]$ and length $[m]$ are converted into LB units dividing by the factors

$$t_0 = \frac{\left(\frac{L_c}{u_{in}}\right)_{phys}}{\left(\frac{L_c}{u_{in}}\right)_{LB}}, \quad L_0 = \frac{(L_c)_{phys}}{(L_c)_{LB}}, \tag{7.17}$$

respectively. Let δx be the space step, the time step

$$\delta t_{LB} = \left(\frac{\delta x}{e}\right)_{LB}, \quad \delta t_{phys} = t_0 \delta t_{LB}, \tag{7.18}$$

is set by defining the ratio $(L_c/u_{in})_{LB}$, and $e = 1$ is the magnitude of the non-zero lattice velocities of Fig. 3.1. The initial profiles are flat,

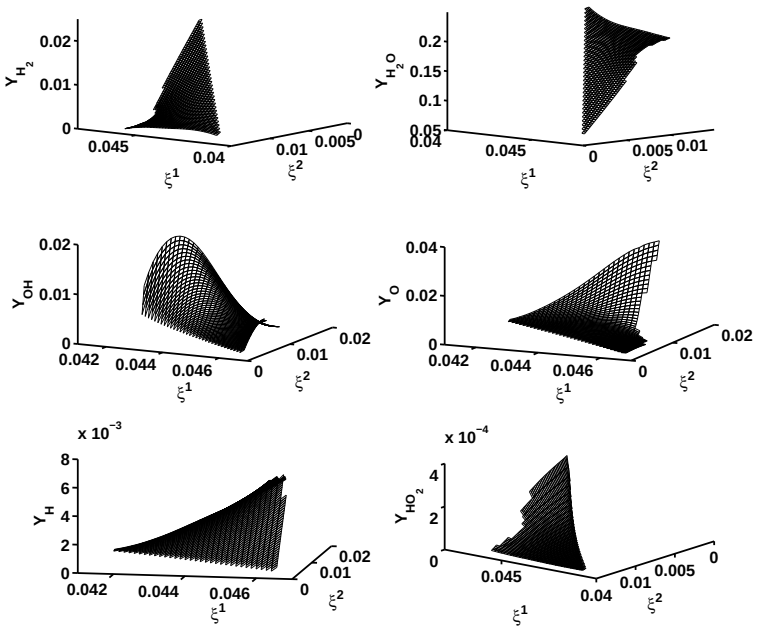

Figure 7.4.: Six coordinates of the refined 2D invariant grid for stoichiometric H_2-air mixture, under $p = 1bar$ and $\tilde{h} = 2.8kJ/kg$.

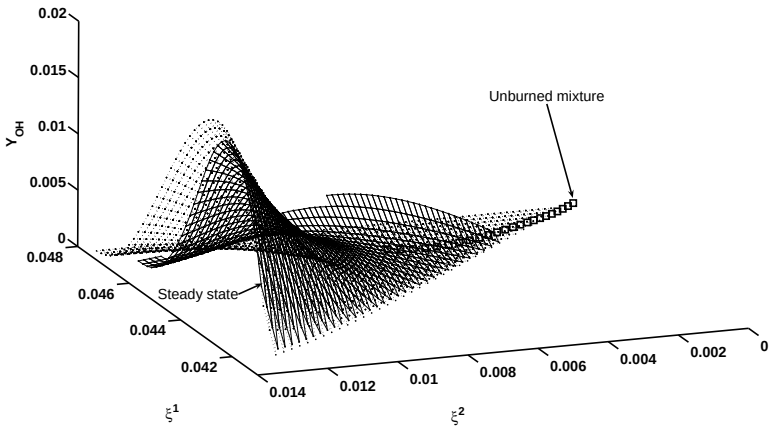

Figure 7.5.: OH coordinate: 2D quasi equilibrium grid (dashed lines), 2D invariant grid (continuous lines), trajectory starting from the unburned mixture (squares).

corresponding to the unburned mixture with $T = 300K$, everywhere except in a neighborhood of the outlet, where the temperature peaks up to $T = 1400K$, in order to let the mixture ignite. At the inlet, the initial conditions are imposed while, at the outlet, the fully developed boundary conditions are used for every field. Because of the stiffness of the chemical source term, a stable computation, carried out by using the model in section 7.3.1, requires $\delta t_{phys} \leq 6 \times 10^{-8}[s]$. Notice that, due to unity Lewis number, the enthalpy is uniform in space and the temperature is given by solving the uppermost equation in (1.9).

Identical setup can be also simulated using the modified algorithm of section 7.3.3, where the reduced description is provided either by the 2D quasi equilibrium grid or by the refined invariant grid. The latter option is chosen, results are shown in Fig. 7.6 and compared to the solution of the original detailed reaction model. The invariant grid does not extend in the low temperature zone: here, the source terms are evaluated as in the original model and the correction step (7.11) is not performed. For simplicity, based on the assumption that the variables (7.14) are slow in the whole concentration space, the point M^* of Fig. 7.1 is the grid state which corresponds to the pair $\left(\xi^1, \xi^2\right)$ computed at E^*. The agreement between the two models is excellent and, using the modified algorithm, computa-

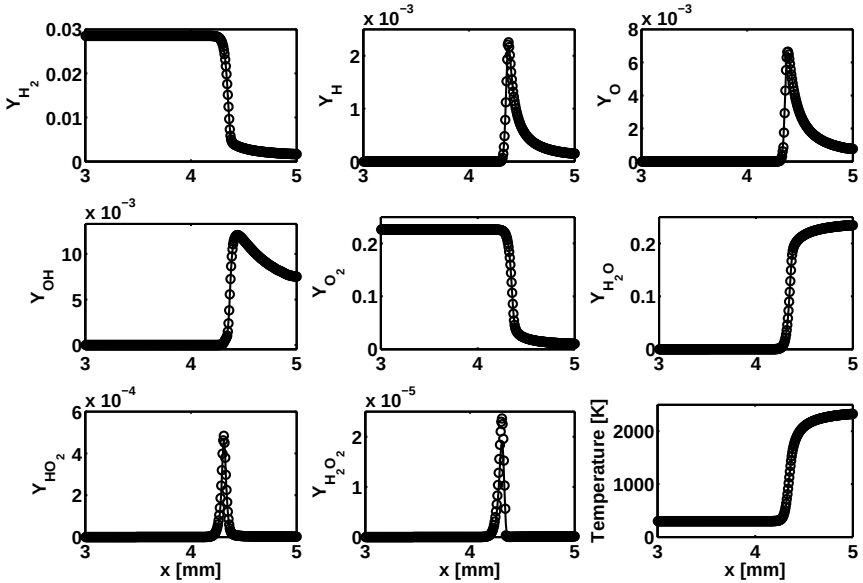

Figure 7.6.: Fields along the channel at a given time: detailed model (continuous line) and reduced model (circles).

tions are stable with the time step $\delta t_{phys} \leq 5 \times 10^{-7}[s]$. Moreover, in the latter case the extra effort, due to an additional step (7.11), is counterbalanced by savings during the computation of the chemical source terms: indeed, those quantities demand the evaluation of exponential functions (see (1.2) and (1.3)), whereas for the reduced model a fast look up table is adopted. As a result, in our simulations, the modified sequence of section 7.3.3, with interpolated source terms Q_{Y_i}, is about 30% faster than the detailed reaction algorithm, where Q_{Y_i} are explicitly computed. Overall, the suggested methodology exhibits a speedup of ten times.

7.4.3. Dimension reduction

Let all species have equal diffusivity D, a projection of species evolution equations in (7.2) onto the invariant grid, according to the slow variables

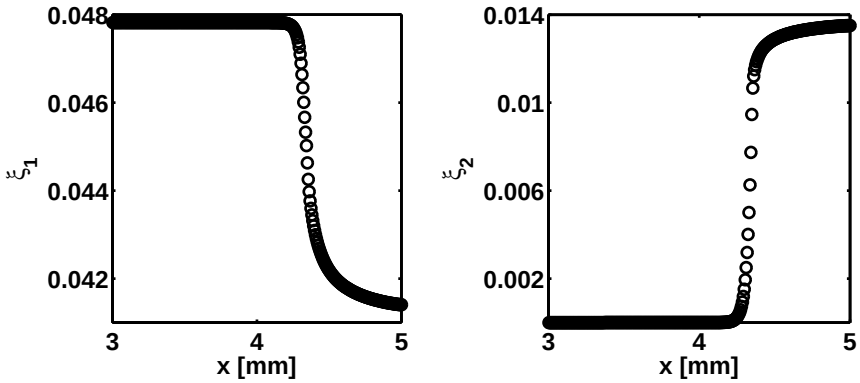

Figure 7.7.: Manifold parameters along the channel.

(7.14), gives

$$\begin{aligned}\tilde{h}_\alpha\left(\boldsymbol{x}+\boldsymbol{e}_\alpha, t+\delta t\right)-\tilde{h}_\alpha\left(\boldsymbol{x}, t\right) &= -\tfrac{1}{\tau_T}\left[\tilde{h}_\alpha\left(\boldsymbol{x}, t\right)-\tilde{h}_\alpha^{eq}\left(h, \boldsymbol{u}\right)\right]+w_\alpha Q_h,\\ \xi_\alpha^j\left(\boldsymbol{x}+\boldsymbol{e}_\alpha, t+\delta t\right)-\xi_\alpha^j\left(\boldsymbol{x}, t\right) &= -\tfrac{1}{\tau_\xi}\left[\xi_\alpha^j(\boldsymbol{x}, t)-\xi_\alpha^{jeq}\left(\xi^j, \boldsymbol{u}\right)\right]+w_\alpha Q_{\xi^j}.\end{aligned} \tag{7.19}$$

Here, the equilibrium populations for the reduced variables ξ^j read

$$\xi_\alpha^{jeq}=w_\alpha \xi^j\left[1+3\left(\boldsymbol{e}_\alpha \boldsymbol{u}^T\right)+\frac{9}{2}\left(\boldsymbol{e}_\alpha \boldsymbol{u}^T\right)^2-\frac{3}{2}\boldsymbol{u}^2\right], \tag{7.20}$$

where $D=\delta t(2\tau_\xi-1)/6$, $Q_{\xi^j}=\sum_i \boldsymbol{m}_j(i)\, Q_{Y_i}$, $\xi^j=\sum_{i=1}^{9}\boldsymbol{m}_j(i)\, Y_i=\sum_{\alpha=1}^{3}\xi_\alpha^j$. Now, the setup of section 7.4.2 can be simulated by solving for only the two lumped variables ξ^j using (7.19) and tabulated source terms Q_{ξ^j}, while the flow dynamics still follows (3.1). The result is shown in Fig. 7.7, and all relevant fields $Y_i\left(\xi^1,\xi^2\right)$, $T\left(\xi^1,\xi^2\right)$ can be reconstructed by interpolation on the invariant grid in a post-processing. Here, in the low temperature region, a 1D induction manifold is used, instead of detailed chemistry. The induction manifold is obtained by a fit from the detailed solution and it is parametrized by ξ^1. This time, due to the slow dynamics of ξ^j, computations are stable with $\delta t \leq 1\times 10^{-6}$: yet, as reported in Fig. 7.8, the detailed solution is reproduced with excellent accuracy.

It is worth stressing that a remarkable saving, in terms of memory, is now achieved, too. Indeed, for the presented 1D problem, the number of

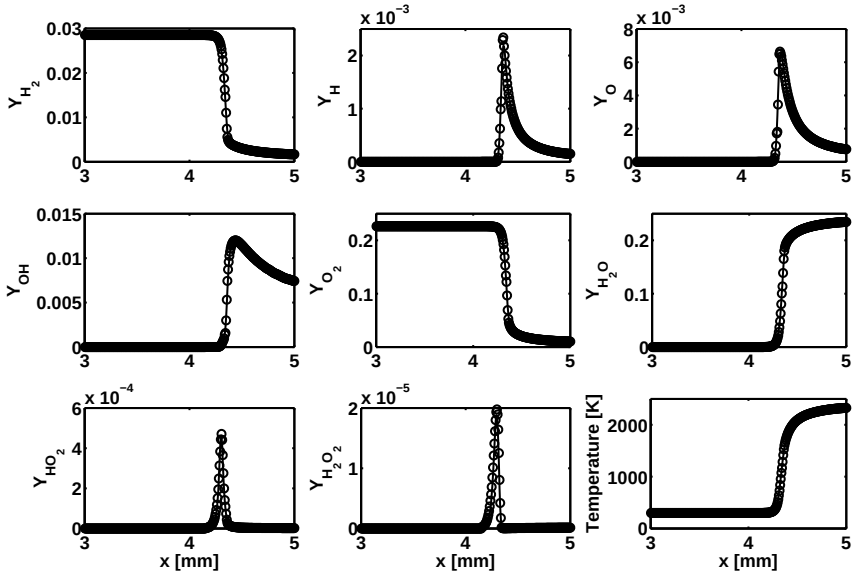

Figure 7.8.: Detailed solution (continuous lines) vs reduced solution (circles) reconstructed by parameters of Fig. 7.7.

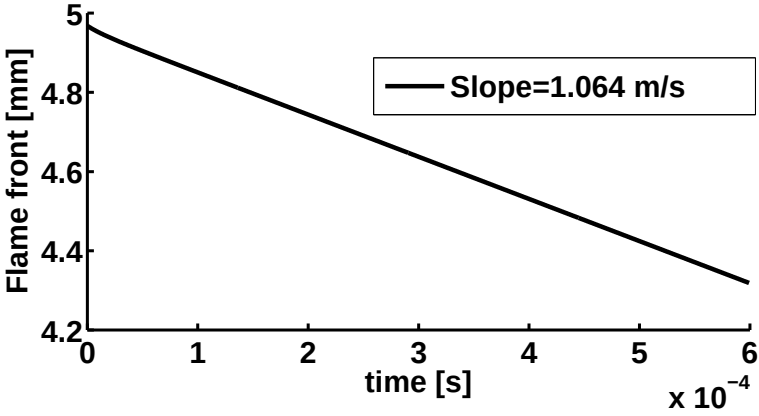

Figure 7.9.: Flame front position vs time.

density functions, stored at each lattice node, is one fourth. Whenever the hypothesis of equal diffusivity can be applied, such an approach reveals to be extremely convenient, especially in the case of larger population sets needed for 2D and 3D reactive flows. Finally, in Fig. 7.9 the flame position is shown as function of time. The flame is defined as the point with the highest heat release Q_h at a given time. The linear dependence indicates that the flame front moves at constant speed given by: S_L = slope + $u_{in} \cong 2.26 m/s$. The value of the burning velocity S_L is in perfect accordance with the detailed model prediction (up to 2%) and in a good agreement with experimental data (see, e.g., [43]).

7.5. Example: Premix counterflow flames

In this section, we consider the so-called counterflow laminar flame as two dimensional benchmark of the suggested methodology. A well premixed stoichiometric H_2-air mixture is uniformly ejected from two parallel stationary flat nozzles, located at $y = \pm L_y$. When properly ignited, the fuel reacts generating two twin flames in this counterflow, while the burned gas exits the domain along the x-direction. As illustrated in the sketch of Fig. 7.10, under the assumption of symmetrical flow with respect to the stagnation lines $x = 0$ and $y = 0$, the computational domain can be restricted to the region where $x \geq 0$ and $y \geq 0$.

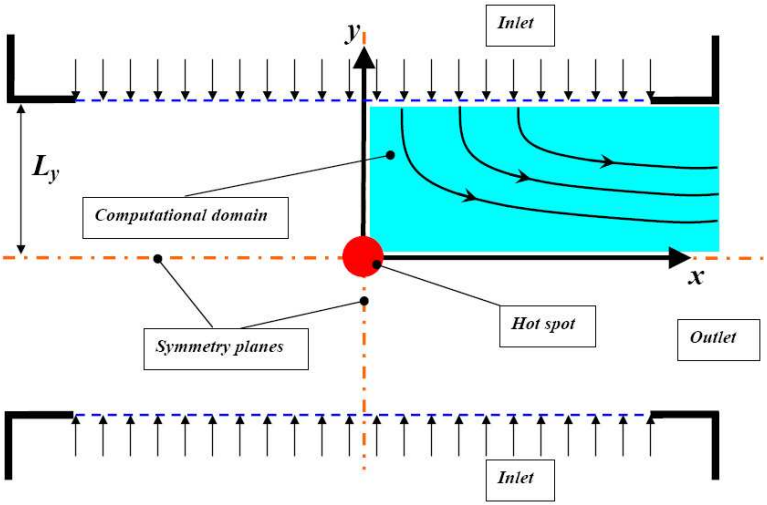

Figure 7.10.: Layout of the counterflow laminar flame.

In the present configuration, the half-length of the gap between the two nozzles is $L_y = 2[mm]$, the computational domain is rectangular with aspect-ratio $L_x/L_y = 1.67$, and symmetry conditions at the stagnation lines are used. At the inlet, we impose a constant velocity $u_{in} = -2.4[m/s]$, room temperature $T_{in} = 300[K]$, pressure $p = p_0 = 1[bar]$ and species concentrations corresponding to the unburned mixture. At the outlet, the pressure is constant $p = p_0$, and we utilize fully developed boundary conditions as discussed below.

7.5.1. Flow field

In our simulation, we adopt a $200(N_x) \times 120(N_y)$ grid, and a constant kinematic viscosity: $\nu = 1.6 \times 10^{-5}[m^2/2]$. At the inlet, the equilibrium populations, corresponding to the pressure $p = p_0 = 1[bar]$ and velocities $u_x = 0$, $u_y = u_{in}$, are maintained. In order to implement symmetry condition, we apply the mirror bounce-back scheme to the missing pressure density functions along the stagnation line $x = 0$:

$$p_x = p_{mx}, \quad p_{xy} = p_{mxy}, \quad p_{xmy} = p_{mxmy}, \tag{7.21}$$

while along the line $y = 0$,

$$p_y = p_{my}, \quad p_{xy} = p_{xmy}, \quad p_{mxy} = p_{mxmy}. \tag{7.22}$$

At the outlet, the fully developed boundary conditions are imposed by replacing all pressure populations with the corresponding equilibrium populations evaluated with $p = p_0$, and velocities at the neighbor node along x:

$$p_\alpha (N_x) = p_\alpha^{eq} (p_0, u_x (N_x - 1), u_y (N_x - 1)). \tag{7.23}$$

Finally, the wall of the nozzle at the end of the upper limit of the domain is simulated using five nodes, where the standard bounce-back condition is imposed:

$$p_{my} = p_y, \quad p_{xmy} = p_{mxy}, \quad p_{mxmy} = p_{xy}. \tag{7.24}$$

It has been proved that the lattice Boltzmann method is able to reproduce the results of conventional methods (finite differences) in the case of counterflow with high accuracy [69]. Figure 7.11 shows the streamlines of the flow field when the steady solution is reached, while in Fig. 7.12 we report the normalized velocities (with respect to u_{in}) along the stagnation lines.

7.5.2. Temperature and concentration fields

In the following, we simulate the temperature and concentration fields using both the full model and a reduced one (two degrees of freedom). For the sake of simplicity, here we assume equal diffusion coefficients $D_i = D = 5 \times 10^{-5} [m^2/s]$ for all species, and unity Lewis number: $Le = D/\kappa = 1$. In this case, the two dimensional invariant grid of Fig. 7.4 can be adopted as reduced description of the detailed model. According to the procedure of section 7.4.3, here we apply the lattice Boltzmann equation only to the invariant manifold parameters $\xi^{1,2}$ (7.14), and all the relevant fields are reconstructed in a post-processing via bi-linear interpolation on the grid tables. Similarly to the pressure populations, the mirror bounce-back scheme is used as boundary condition for the missing density functions, $Y_{i,\alpha}, \xi_\alpha^i$, along the stagnation lines. At the inlet, the equilibrium populations corresponding to the unburned mixture are constantly imposed, while at the outlet we make use of the following extrapolation:

$$Y_{i\alpha} (N_x) = Y_{i\alpha} (N_x - 1), \quad \xi_\alpha^i (N_x) = \xi_\alpha^i (N_x - 1), \tag{7.25}$$

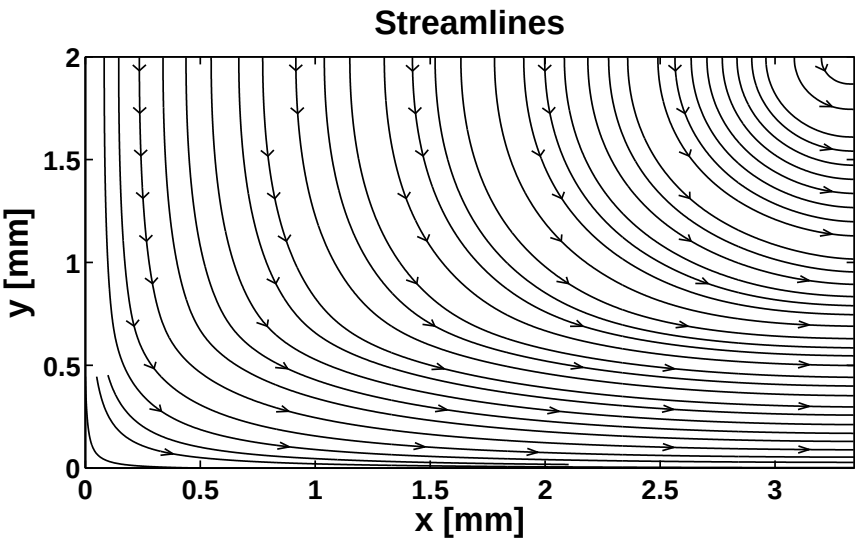

Figure 7.11.: Streamlines of the background flow field.

for the detailed and reduced model, respectively. The nozzle wall is supposed to be adiabatic and the usual bounce-back condition is adopted. Because of unity Lewis number, the mixture-averaged enthalpy $\bar{h}$ remains constant throughout the entire domain, thus it is dependent on the species concentrations according to the uppermost equation in (1.9).

In both models, the mixture, initially under room temperature $T_0 = 300[K]$, is ignited by placing a hot spot at the origin of the reference system. A comparison between the detailed and reduced fields, along the stagnation line $x = 0$, is shown in Fig. 7.13 at the same time instant $t = 1.05[ms]$, and an excellent agreement is demonstrated.

Moreover, in Figures 7.14, 7.15, 7.16, 7.17, 7.18, 7.19, we report a sequence of snapshots where concentration and temperature fields are shown in the whole computational domain. On the basis of the present study, we can argue that the reduced model is indeed able to match the detailed solution with high accuracy. However, similarly to the one-dimensional example in section 7.4.3, the time step δt needed for stably solving the lattice Boltzmann equations can be increased by one order of magnitude in the reduced model.

Remark-Notice that, in the case of low-Mach number combustion and fixed

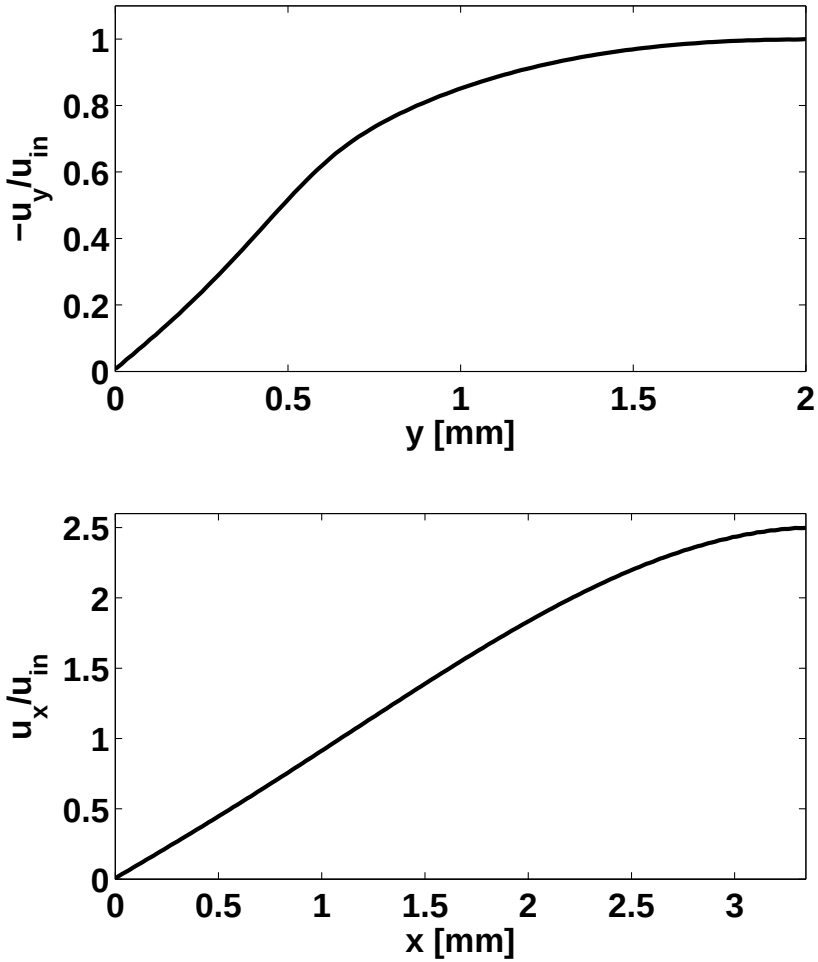

Figure 7.12.: Distribution of non-dimensional velocities along the symmetry axis.

pressure, the above assumptions (on the Lewis number Le) can be gradually relaxed, so that three cases of different complexity are obtained.

1. Equal diffusivities with $Le = 1$. Even though this might lead to an inaccurate approximation for hydrogen systems (e.g. quite different diffusivities should be used for light species such as H_2 and H), here it is considered for validation purposes. Moreover, such a condition is of interest for simulating turbulent flames [45].

2. Equal diffusivities with $Le \neq 1$. In this case, the element composition is conserved but the mixture-averaged enthalpy $\bar{h}$ changes in the domain. Now, the conservation equation for enthalpy has to be solved along with the species equations (see (7.19)), and the reduced system is fully described by three variables ($q + 1$ variables in the general case of a q-dimensional invariant grid): ξ^1, ξ^2 and $\bar{h}$. Hence, the construction of chapter 6 has to be performed for a discrete set of enthalpies.

3. General case. In general, also the element composition varies in the domain due to differential diffusion effects. Thus, equations for the lumped variables ξ^j, mixture enthalpy $\bar{h}$ and the element mole numbers N_k (6.6) need to be solved, whereas a generic tabulated quantity is function of additional variables: $\mathcal{Q} = \mathcal{Q}\left(\xi^1, \xi^2, \bar{h}, N_H, N_O\right)$. The evolutionary equation for the element mole number N_k is obtained combining (1.11) and (7.8):

$$\bar{\rho}\left(\partial_t N_k + u_j \partial_j N_k\right) = \partial_j \left(\bar{\rho}\partial_j \left(\sum_{i=1}^{n} \frac{D_i \mu_{ik} Y_i}{W_i}\right)\right), \tag{7.26}$$

where

$$N_k = \sum_{i=1}^{n} \frac{\mu_{ik} Y_i}{W_i}.$$

For mass is conserved, the contribution due to the source terms $\dot{\omega}_i$ vanishes in (7.26). Formula (7.26) can be recast as follows:

$$\bar{\rho}\left(\partial_t N_k + u_j \partial_j N_k\right) = \partial_j \left(\bar{\rho}\bar{D}_k \partial_j N_k\right) + \partial_j \left(\bar{\rho} N_k \partial_j \bar{D}_k\right), \tag{7.27}$$

where the quantity

$$\bar{D}_k = \left(\sum_{i=1}^{n} \frac{D_i \mu_{ik} Y_i}{W_i}\right) \Bigg/ N_k,$$

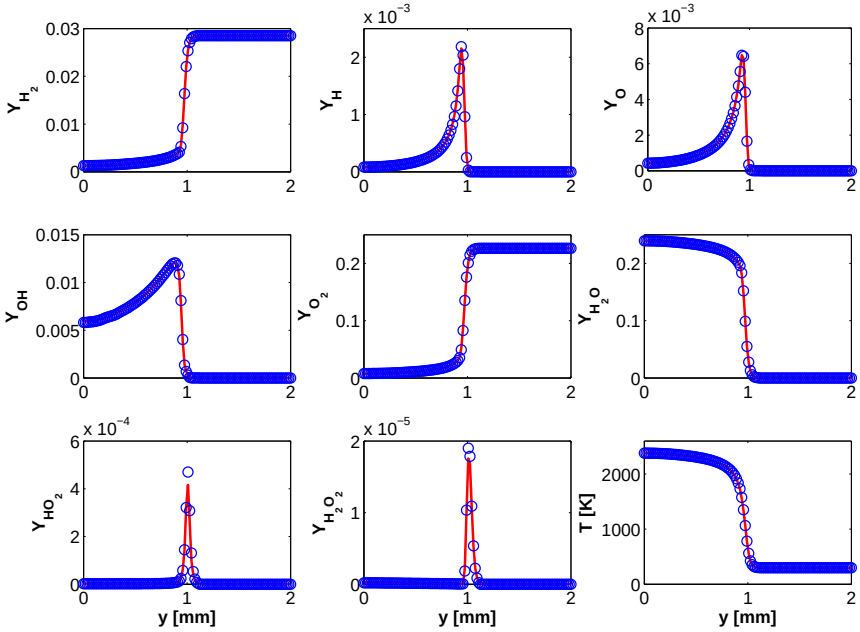

Figure 7.13.: Comparison between detailed (line) and reduced (circles) concentration and temperature profiles along the stagnation line $x = 0$ at the fixed time instant $t = 1.05[ms]$.

can be also tabulated as a function of grid parameters. Notice that, equation (7.27) presents the same form as the species equations (7.8) with diffusivity $\bar{D}_k$ and source term $\partial_j \left(\bar{\rho} N_k \partial_j \bar{D}_k\right)$. Therefore, the latter partial differential equation can be still solved using a lattice Boltzmann type equation with the relaxation parameter $\tau = \tau\left(\bar{D}_k\right)$ of the form (7.5). Nevertheless, this time the source term in (7.27) is non-local and it needs to be evaluated, e.g., with finite differences.

7.6. Conclusions

In this chapter, we suggest a methodology for using accurate reduced chemical kinetics in combination with a lattice Boltzmann solver for simulating reactive flows. It has been shown that the MIG is suitable for providing the reduced description of chemistry, and this approach enables to cope

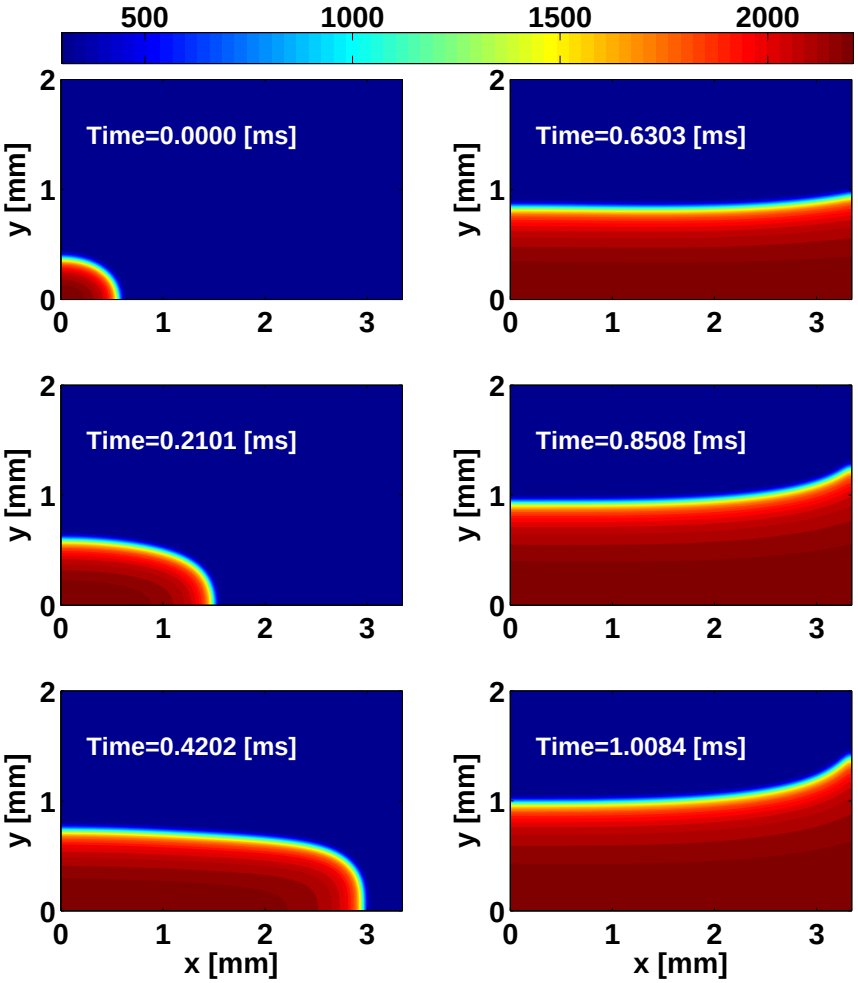

Figure 7.14.: Detailed model using the $D2Q9$: evolution of the temperature field.

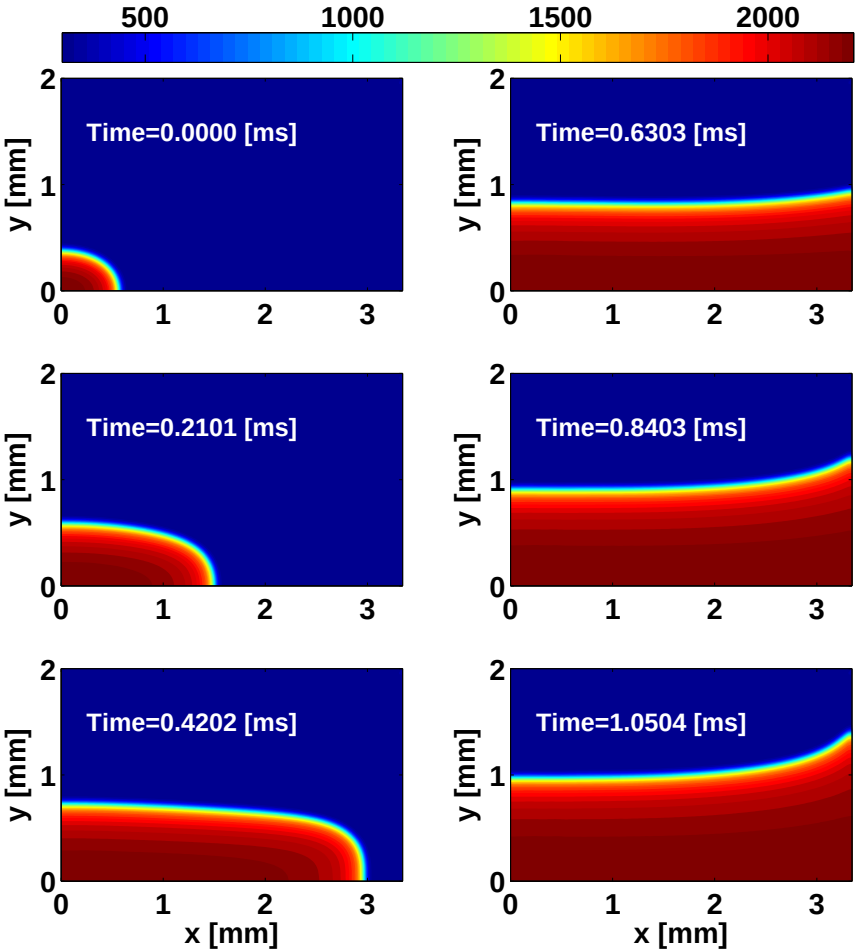

Figure 7.15.: Reduced model using the $D2Q9$ lattice in combination with a 2-dimensional invariant grid: evolution of the temperature field.

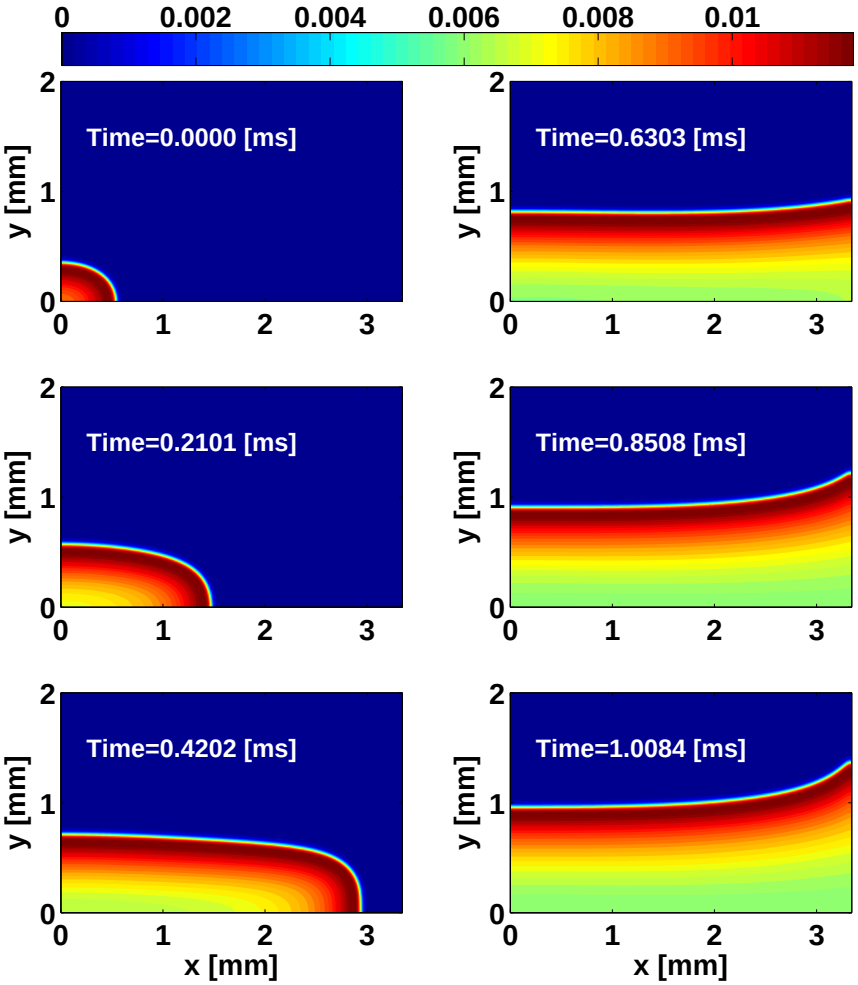

Figure 7.16.: Detailed model using the $D2Q9$: evolution of OH mass fraction.

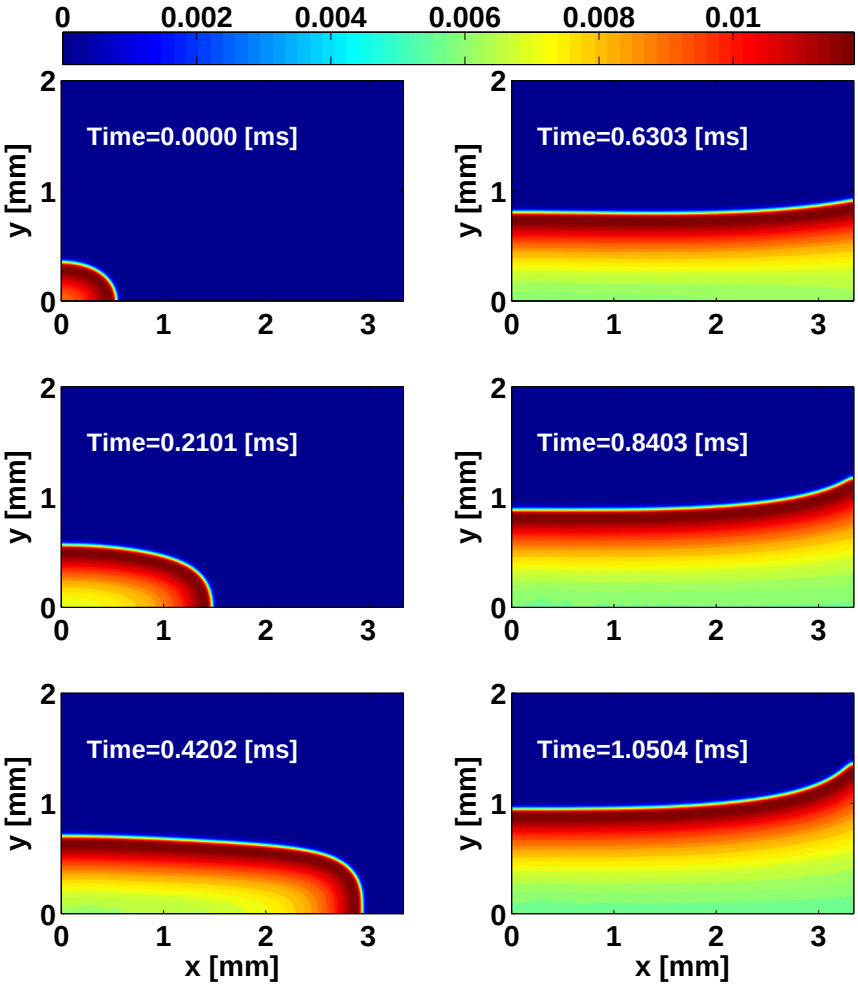

Figure 7.17.: Reduced model using the $D2Q9$ lattice in combination with a 2-dimensional invariant grid: evolution of OH mass fraction.

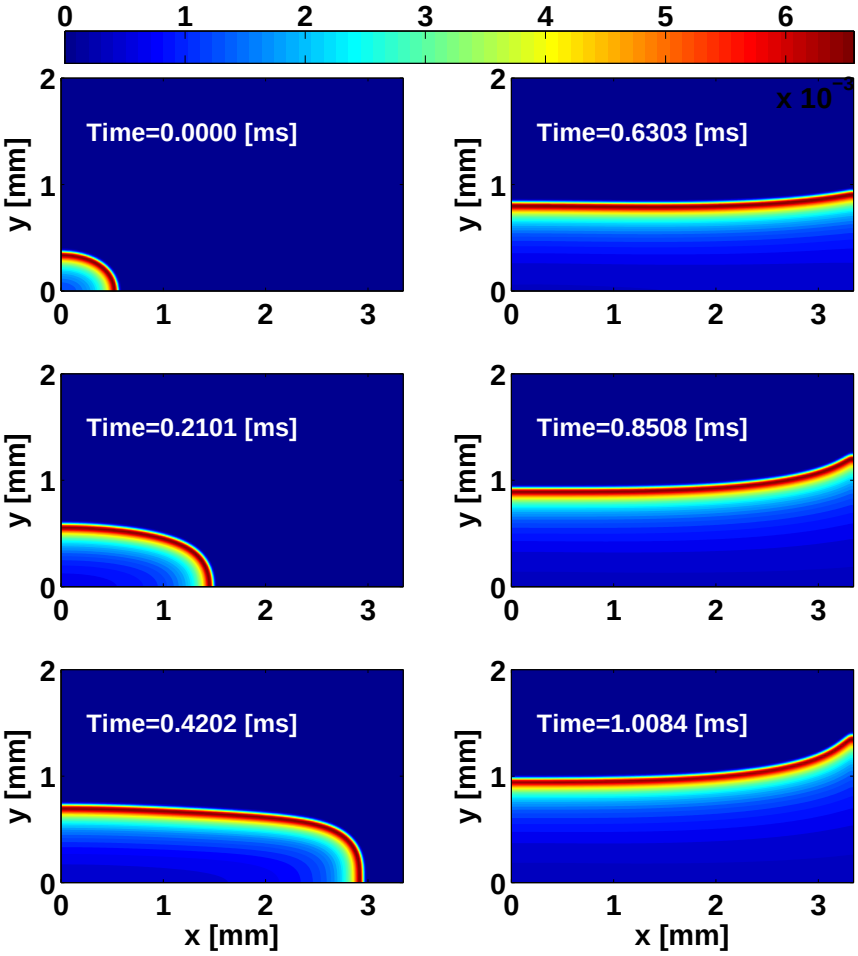

Figure 7.18.: Detailed model using the $D2Q9$: evolution of O mass fraction.

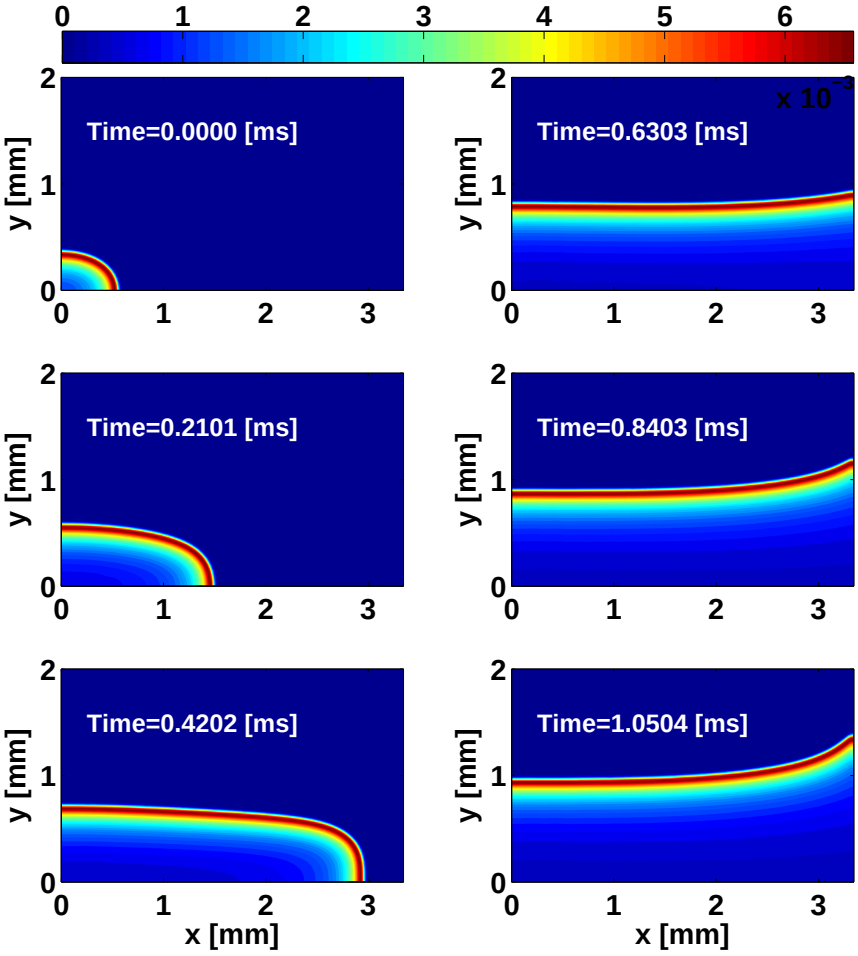

Figure 7.19.: Reduced model using the $D2Q9$ lattice in combination with a 2-dimensional invariant grid: evolution of O mass fraction.

with stiffness when solving the LB species equations due to the possibility of choosing a lager time step δt. This is particularly desirable in the case of explicit solvers, and it results in a remarkable speedup.

Moreover, we show that the number of fields involved in the computation can be drastically reduced, and this aspect is of paramount importance because it effectively addresses the issue of large memory demand. Indeed, while simulating reactive flows with detailed chemistry by the lattice Boltzmann method, the number of fields (density functions) stored in memory is remarkably large compared to conventional methods by a factor ranging from tens to hundreds in the case of 2- and 3-dimensional problems. Therefore, for instance, detailed LB simulations of 2- and 3-dimensional hydrocarbon flames (with hundreds of chemical species) are currently not affordable. In this respect, the present study intends to be a first step toward the efficient, yet accurate, solution to this problem. Applications with hydrocarbon fuels (e.g. methane) and more sophisticated LB models, capable to take into account compressibility effects, shall be considered in the near future.

The better the thoughts are expressed - the more the nail has been hit on the head.

L. Wittgenstein (1889 - 1951)

8. Conclusions and outlook

In this thesis, the problem of reducing the description of a detailed reaction mechanism is addressed. To this end, a novel automated methodology is elaborated and validated for combustion applications. The suggested technique follows a consistent approach of constructing accurate approximations of invariant manifolds for the system of kinetic equations. It turns out that the procedure of model reduction can be split in two separated processes: first the approximate slow invariant manifold (SIM) of a dynamical system is constructed, second the reduced equations of the slow motion along such a manifold and the fast motion towards it are studied.

The core of the construction of SIM (method of invariant grid, MIG for short) is based on two refinement procedures, associated with an algorithm for generating an initial rough and cheap approximation of the slow invariant manifold. In this respect, a SIM can be considered as the stable fixed point of Newton-like iterations aiming at solving the invariance condition, linearized and treated as an equation. Moreover, it is shown that the relaxation of the film equation represents an alternative and effective way of refining non-invariant manifolds, with an embarrassingly simple implementation. A novel relaxation method, which is not restricted by the Courant instability due to an implicit construction of the projector, is also presented and validated in the case of a detailed hydrogen mechanism.

Based on the notion of quasi equilibrium manifold (QEM), a new algorithm for a fast generation of initial SIM approximations is here suggested and validated. It turns out that thermodynamics is useful for at least two aspects of model reduction. First of all, it helps in defining a QEM regarded as the locus of minima of the thermodynamic Lyapunov function (entropy, free energy, free enthalpy, depending on the context) of the kinetic system. Second, once the refinement procedure is terminated and the slow sub-space has been found, defining the thermodynamic projector on the invariant manifold enables us to reconstruct “a posteriori” also the fast subspace, spanned by the null space of the latter projector. As a result, a less stiff dynamical system of equations, governing the slow motion on the manifold, can be written and solved.

Finally, it is shown that the method of invariant grid represents a valuable tool when simulating reactive flows using the lattice Boltzmann (LB) method. Validations are presented in the case of one dimensional freely propagating flame, and two dimensional laminar counter-flow flames. To the best of my knowledge, these are the first applications of a reduced reaction mechanism within the lattice Boltzmann framework. For the sake of simplicity, here the simple LB model of Yamamoto et al. for reactive flows has been employed, where reactions do not affect the flow field.

On one hand, this does not represent a limitation "per se", and the presented methodology can be utilized in combination with more sophisticated models without any restrictions. On the other, the outcome of coupling the LB method with MIG reduced mechanisms is very promising, and it is surely a motivation for further investigations. Indeed, a continuation of this work can be achieved when simulating the flow field using fully compressible models, establishing so the missing link between the flow field and reactions. In fact, accurate and consistent models for compressible flow simulations on standard LB lattices have been proposed very recently (see, e.g., [54]), and their implementation within the context of the suggested methodology is of utmost interest for combustion simulations. In addition, recent studies (see, e.g., [18]) have introduced novel LB schemes for turbulent flow simulations, which prove to be competitive to traditional computational tools.

This certainly paves the way for the development of reliable and efficient software for predicting turbulent reactive flows, based on the LB method and reduced reaction mechanisms, in realistic engineering applications where e.g. hydrocarbon fuels are involved.

9. Nomenclature

Notation

Symbol	Explanation
x_i	chemical species i
n	total number of chemical species, number of degrees of freedom
d	number of chemical elements
r	number of reaction steps
ν_s, ν'_s, ν''_s	stoichiometric vectors of step s
$\Omega_s, \Omega_s^{\pm}$	reaction rates of step s
$k_s^{\pm}$	reaction rate constants of step s
N_i	number of moles of species (element) i
V	volume of a chemical reactor
c_i	molar concentration of species i
A_s, β_s, E_{as}	pre-exponetial factor, temperature exponent and activation energy of step s
$\mathcal{R}$	universal gas constant
$\dot{\omega}_i$	rate of change of species i
$K_{c,s}$	equilibrium reaction rate constant of step s
Y_i	mass fraction of species i
$\boldsymbol{c}, \boldsymbol{\psi}$	states of the phase-space
T	temperature

continued on next page

Symbol (cont.)	Explanation (cont.)
$\boldsymbol{f}$	vector of motions in the phase-space
$\dot{\boldsymbol{c}}$	time derivative of $\boldsymbol{c}$
U_i	inner energy of species i
$\bar{U}$	mixture-averaged inner energy
h_i	enthalpy of species i
$\bar{h}$	mixture-averaged enthalpy
$a_{ji,\ j=1,\ldots,7}$	tabulated constants of species i
p	mixture pressure
W_i	molecular weight of species i
$\bar{\rho}$	mixture density
$\boldsymbol{D}$	element conservation matrix
μ_{ik}	number of atoms of element k in species i
$S_{i,s}^{abs}$	absolute sensitivity of c_i on the rate constant k_s^+
$S_{i,s}^{rel}$	relative sensitivity of c_i on the rate constant k_s^+
$\boldsymbol{J}$	Jacobian matrix
$\boldsymbol{J}', \boldsymbol{J}''$	symmetric and non symmetric parts of $\boldsymbol{J}$
c_i^{eq}, c_i^{ss}	molar concentration of species i at steady state
$\boldsymbol{\Omega}$	arbitrary manifold
$\boldsymbol{\Omega}_{slow}$	slow invariant manifold
$\mathcal{D}$	domain of $\boldsymbol{R}^n$
T_y	tangent space of $\boldsymbol{\Omega}$, slow subspace
$E_y,\ L$	complement to T_y in $\boldsymbol{R}^n$, fast subspace
$\boldsymbol{P}$	projector onto T_y
$\mathrm{im}(\boldsymbol{P})$	image of $\boldsymbol{P}$
$\ker(\boldsymbol{P})$	null space of $\boldsymbol{P}$
$\boldsymbol{\Delta}$	defect of invariance
ξ_i	ith parameter
$\mathcal{W}$	domain in the parameter space

continued on next page

Symbol (cont.)	Explanation (cont.)
q	dimension of the parameter space
$F : \mathcal{W} \to \mathcal{D}$	immersion
$\|\boldsymbol{\eta}\|$	Euclidean norm of an arbitrary vector $\boldsymbol{\eta}$
$\langle \boldsymbol{\eta}_1, \boldsymbol{\eta}_2 \rangle$	entropic product between $\boldsymbol{\eta}_1$ and $\boldsymbol{\eta}_2$
$G,\ \tilde{G}$	thermodynamic Lyapunov function
$\boldsymbol{\nabla} G$	gradient of G
$\boldsymbol{H}$	second derivative matrix of G
$\boldsymbol{I}$	identity matrix
$\mathcal{G}$	discrete subset of $\mathcal{D}$ (grid)
$F \mid_{\mathcal{G}}$	restriction of F on $\mathcal{G}$
$\hat{\boldsymbol{u}}_1, ..., \hat{\boldsymbol{u}}_q$	vector basis of thermodynamic projector
$\mathcal{G}_{inv}$	invariant grid
$\mathcal{G}_0$	initial grid
$DG(\boldsymbol{\eta})$	linear functional acting on an arbitrary vector $\boldsymbol{\eta}$
$\boldsymbol{a}_{s,f},\ \boldsymbol{x}_{r,l}^{s,f}$	slow and fast eigenvectors of $\boldsymbol{J}$
$\delta \boldsymbol{c}$	shift vector
$\boldsymbol{S}$	intersection between the null space of $\boldsymbol{P}$ and the null space of $\boldsymbol{D}$
$\hat{h}$	dimension of $\boldsymbol{S}$
$\boldsymbol{b}_1, ..., \boldsymbol{b}_{\hat{h}}$	vector basis of $\boldsymbol{S}$
$\delta_1, ..., \delta_{\hat{h}}$	unknowns in the Newton method
δt	time step
$\hbar$	damping parameter for Newton method
$DMQN$	lattice boltzmann model where $M = 1, 2, 3$ and N : number of discrete velocities
p_α	pressure distribution function, pressure populations
f_α	density distribution function
$p_0,\ p_{ref}$	reference pressure

continued on next page

Symbol (cont.)	Explanation (cont.)
ρ_0	reference density
$\boldsymbol{e}_\alpha$	particle velocity in the lattice Boltzmann equations
p_α^{eq}	equilibrium pressure populations
f_α^{eq}	equilibrium density populations
$\boldsymbol{u}$	fluid velocity
w_α	equilibrium population weight
τ_F	relaxation parameter
ν	kinematic viscosity
$\mathcal{H}$	$\mathcal{H}$-function
$\boldsymbol{a}_i^{s,f}, \boldsymbol{b}_i^{s,f}$	CSP vectors
$\boldsymbol{A}_{s,f}, \boldsymbol{B}^{s,f}, \boldsymbol{\tau}$	CSP matrices
δ_{ij}	Kronecker delta
$\boldsymbol{m}_1, ..., \boldsymbol{m}_q$	parameterization vectors
λ_i	eigenvalue of $\boldsymbol{J}$
$\boldsymbol{Q}$	ILDM transition matrix
$\boldsymbol{J}^{sym}$	symmetrized Jacobian matrix
$\tilde{\boldsymbol{Q}}_f$	spectral projector
δ_H	Hausdorff distance
$\boldsymbol{E}$	QEG constraint matrix
ε	small parameter
$\boldsymbol{\rho}_i$	vector in the null space of $\boldsymbol{D}$
$\boldsymbol{t}_i$	vector in the null space of $\boldsymbol{E}$
$\bar{s}$	mixture-averaged entropy
s_i	entropy of species i
X_i	mole fraction of species i
ϕ	equivalence ratio
ϕ_i	specific mole number of species i
$\mathcal{Q}$	tabulated quantity

continued on next page

Symbol (cont.)	Explanation (cont.)
ι_i	weight for interpolation
T_0	reference temperature
$\tilde{T}$	dimensionless temperature
$\tilde{T}_\alpha$	temperature distribution function
$\tilde{T}_\alpha^{eq}$	equilibrium population for temperature
$Y_{i\alpha}$	mass fraction distribution function
$Y_{i\alpha}^{eq}$	equilibrium population for mass fraction of species i
$Q_T,\ Q_{Y_i}$	source terms in the lattice Boltzmann equation
$Q_h,\ Q_{\xi^i}$	source terms in the lattice Boltzmann equation
$\bar{C}_p$	mean specific heat of a gas mixture
κ	thermal diffusivity
D_i	diffusion coefficient of species i
t_0	time conversion factor
$()_{LB}$	lattice Boltzmann units
$()_{phys}$	physical units
h_0	reference enthalpy
$\tilde{h}$	dimensionless enthalpy
$\tilde{h}_\alpha$	enthalpy distribution function
$\tilde{h}_\alpha^{eq}$	equilibrium population for enthalpy
$\tilde{h}_\alpha^*,\ Y_{i\alpha}^*$	intermediate populations
$\psi_{i\alpha}$	correction term
Le	Lewis number
π_i	weighting function
$L_c,\ L_x,\ L_y$	channel dimensions
u_{in}	inlet velocity
T_{in}	inlet temperature
δx	space step
ξ_α^j	distribution function of a grid parameter

continued on next page

Symbol (cont.)	Explanation (cont.)
ξ_α^{jeq}	equilibrium population for a grid parameter
S_L	burning velocity
C_{pi}	specific heat of species i under constant pressure
C_{vi}	specific heat of species i under constant volume
λ, λ_k	Lagrange multipliers
SIM	slow invariant manifold
QSSA	quasi steady state assumption
ILDM	intrinsic low dimensional manifold
CSP	computational singular perturbation
MIG	method of invariant grids
CFD	computational fluid dynamics
LB	lattice Boltzmann
N-S	Navier-Stokes
QEM	quasi equilibrium manifold
QEG	quasi equilibrium grid
QEGA	quasi equilibrium grid algorithm
SQEM	spectral quasi equilibrium manifold
SQEG	spectral quasi equilibrium grid
SEILDM	symmetric entropic intrinsic low dimensional manifold
ODE	ordinary differential equation
GQEG	guided quasi equilibrium grid
SEGQEG	symmetric entropic guided quasi equilibrium grid
RCCE	rate controlled constrained equilibrium
RK4	Runge-Kutta 4-th order
RRM	relaxation redistribution method
H_2	hydrogen
O_2	oxygen

continued on next page

Symbol (cont.)	Explanation (cont.)
N_2	nitrogen
H_2O	water
H	hydrogen radical
O	oxygen radical
OH	hydroxyl radical
HO_2	hydroperoxyl radical
H_2O_2	hydrogen peroxide

10. Curriculum Vitae

Eliodoro Chiavazzo

Personal Data

Date of birth:	25th May 1978
Sex:	male
Place of birth:	Nocera Inferiore (SA) (Italy)
Citizen of:	Italy

Education

- **PhD thesis (2006-2009)**
  - Title: Invariant manifolds and lattice Boltzmann method for combustion
  - Advisor: Prof. Dr. K.B. Boulouchos and Dr. I. Karlin
  - Department: Institute of Energy Technology, Mechanical Engineering
  - Place: ETH Zürich (Switzerland)
- **Diploma of Mechanical Engineering (1997-2003)**
  - Title: Feasibility study of an electro-hydraulic variable valve actuator (VVA) for internal combustion engines
  - Advisor: Prof. Dr. M. Migliaccio and Dr. G. Police
  - Department: Department of Mechanical Engineering, and "Istituto Motori" of the Italian National Council of Research (CNR)

  - Place: University of Naples Federico II, Naples (Italy)

Work experience

- **Mechatronics Designer (2003-2006)**
  - Place: Dell'Orto S.p.a. and Italian National Council of Research, Naples (Italy)
- **Research consultant (2005)**
  - Place: ProtoDesign S.r.l, Avellino (Italy)

Teaching experience

- **Teaching assistant (2006-2008, three semesters)**
  - Course: Thermodynamics II
  - Place: ETH Zürich (Switzerland)
- **Lecturer (2005)**
  - Course: Principles of CAD design
  - Place: District of Campania, Angri (Italy)

Publications

- E. Chiavazzo, I.V. Karlin, A.N. Gorban, K. Boulouchos, *Coupling of the model reduction technique with the lattice Boltzmann method for combustion simulations*, (Preprint), 2009
- E. Chiavazzo, I.V. Karlin, A.N. Gorban, *The Role of Thermodynamics in Model Reduction when using Invariant Grids*, (Preprint), 2009
- E. Chiavazzo, I.V. Karlin, A.N. Gorban, K. Boulouchos, *Combustion simulation via lattice Boltzmann and reduced chemical kinetics*, (to appear in Jour. of Statististical Mechanics: Teory and experiments), 2009
- E. Chiavazzo, I.V. Karlin, C.E. Frouzakis, K. Boulouchos, *Method of invariant grid for model reduction of hydrogen combustion*, Proc. Combust. Instit., 32:519-526, 2009

- E. Chiavazzo, I.V. Karlin, *Quasi-equilibrium grid algorithm: Geometric construction for model reduction*, Jour. Comput. Phys., 227:5535-5560, 2008
- E. Chiavazzo, A.N. Gorban, I.V. Karlin, *Comparison of invariant manifolds for model reduction in chemical kinetics*, Communications in Computational Physics, 2:964-992, 2007

Patents

- P. Dell'Orto, M. Marchetti, E. Chiavazzo, G. Manganiello, A. Di Gaeta, G. Police, *Electro-hydraulic variable valve actuator and method to control valves of internal combustion engines*, Publication number: EP1770247. Date of Publication: 04.04.2007 (European patent)
- P. Dell'Orto, M. Marchetti, E. Chiavazzo, G. Manganiello, A. Di Gaeta, G. Police, *Variable-actuation, electro-hydraulic system and device controlling the valves of internal combustion engines*, Publication number: EP1843013. Date of Publication: 10.10.2007 (European patent)
- P. Dell'Orto, A. Di Gaeta, G. Police, M. Marchetti, E. Chiavazzo, G. Manganiello, *Dispositivo elettromeccanico di comando delle valvole di motori a combustione interna ad azionamento variabile*, Publication number: MI2005A001811. Date of Publication: 28.09.2005 (Italian patent)

Presentations

- E. Chiavazzo, I.V. Karlin, A.N. Gorban, K. Boulouchos, *Invariant Grids and Lattice Boltzmann Method for Combustion*, International Workshop on Model Reduction in Reacting Flows, April 2009 Notre Dame, Indiana (USA)
- E. Chiavazzo, *Invariant Manifolds and Lattice Boltzmann method for Combustion*, Invited Lecture at Prof. H. J. Herrmann group at ETH-Zurich, January 2009 Zurich (Switzerland)
- E. Chiavazzo, I.V. Karlin, C.E. Frouzakis, K. Boulouchos, A.N. Gorban, Method of invariant grids for model reduction of hydrogen combustion, 32nd International Symposium on Combustion, August 2008 Montréal (Canada)

- E. Chiavazzo, I.V. Karlin, A.N. Gorban, *Simulation of combustion fields via the lattice Boltzmann method and reduced chemical kinetics*, 17$^{\text{th}}$ Discrete Simulation of Fluid Dynamics, August 2008 Florianópolis (Brazil)
- E. Chiavazzo, I.V. Karlin, A.N. Gorban, *Model reduction by using invariant grids*, International Workshop on Model Reduction in Reacting Flows, September 2007 Rome (Italy)
- E. Chiavazzo, A.N. Gorban, I.V. Karlin, *The method of invariant grids for model reduction*, 2$^{\text{nd}}$ International Workshop on Mathematics in Chemical and Biochemical Kinetics and Engineering, February 2007 Houston, Texas (USA)
- E. Chiavazzo, I.V. Karlin, *Method of invariant grids for chemical kinetics*, 15$^{\text{th}}$ Discrete Simulation of Fluid Dynamics, August 2006 Geneva (Switzerland)
- P. Dell'Orto, P. Colombo, E. Chiavazzo, G. Manganiello, M. Marchetti, M. Migliaccio, P. Grassia, *The Dell'Orto Direct Injection System for Small Engines*, Development Trends of Motorcycles, 3$^{\text{rd}}$ International conference, April 2005 Bologna (Italy)
- P. Dell'Orto, P. Colombo, E. Chiavazzo, G. Manganiello, M. Marchetti, M. Migliaccio, P. Grassia, *Motorcycles Engine Management System*, Development Trends of Motorcycles, 3$^{\text{rd}}$ International conference, April 2005 Bologna (Italy)

Bibliography

[1] S. Ansumali. *Minimal Kinetic Modeling of Hydrodynamics*. PhD thesis, Swiss Federal Institute of Technology, ETH-Zurich, 2004.

[2] S. Ansumali, I. V. Karlin, S. Arcidiacono, A. Abbas, and N. Prasianakis. Hydrodynamic beyond navier-stokes: Exact solution to the lattice boltzmann hierarchy. *Phys. Rev. Lett.*, 98(124502), 2007.

[3] S. Arcidiacono, J. Mantzaras, S. Ansumali, I. V. Karlin, C. Frouzakis, and K. B. Boulouchos. Simulation of binary mixtures with the lattice boltzman method. *Phys. Rev. E*, 74(5), 2006.

[4] S. Arcidiacono, J. Mantzaras, S. Ansumali, I. V. Karlin, C. E. Frouzakis, and K. Boulouchos. Simulation of binary mixtures with the lattice boltzmann method. *Phys. Rev. E*, 74, 2006.

[5] S. Arcidiacono, I. V. Karlin, J. Mantzaras, and C. E. Frouzakis. Lattice boltzmann model for the simulation of multicomponent mixtures. *Phys. Rev. E*, 76, 2007.

[6] P. L. Bhatnagar, E. P. Gross, and M. Krook. A model for collision processes in gases. i. small amplitude processes in charged and neutral one-component systems. *Phys. Rev.*, 94(3):511–525, 1954.

[7] P. Bishnu, D. Hamiroune, and M. Metghalchi. Development of constrained equilibrium codes and their applications in nonequilibrium thermodynamics. *ASME*, 123:214–220, 2001.

[8] G. Buzzi Ferraris. *Metodi Numerici e Software in C++*. Pearson Education Italia, 1998.

[9] V. Bykov, I. Goldfarb, V. Gol'dshtein, and U. Maas. On a modified version of ildm approach: asymptotic analysis based on integral manifolds. *IMA Jour. of Applied Math.*, pages 1–24, 2005.

[10] V. I. Bykov, G. S. Yablonskii, and T. A. Akramov. The rate of the free energy decrease in the course of the complex chemical reaction. *Dokl. Akad. Nauk SSSR (Doklady Chemistry)*, 234(3):621–634, 1977.

[11] S. Chen and G. Doolen. Lattice boltzmann method for fluid flows. *Annual Review of Fluid Mechanics*, 30:329–364, 1998.

[12] S. Chen, D. Martínez, and R. Mei. On boundary conditions in lattice boltzmann methods. *Physics of fluids*, 8(9):2527–2536, 1996.

[13] S. Chen, Z. Liu, C. Zhang, Z. He, Z. Tian, B. Shi, and C. Zheng. A novel coupled lattice boltzmann model for low mach number combustion simulation. *Applied Mathematics and Computation*, 193:266–284, 2007.

[14] S. Chen, Z. Liu, Z. Tian, B. Shi, and C. Zheng. A simple lattice boltzmann scheme for combustion simulation. *Computers and Mathematics with Applications*, 55:1424–1432, 2008.

[15] E. Chiavazzo and I. V. Karlin. Quasi-equilibrium grid algorithm: Geometric construction for model reduction. *J. Comput. Phys.*, 227: 5535–5560, 2008.

[16] E. Chiavazzo, A. N. Gorban, and I. V. Karlin. Comparison of invariant manifolds for model reduction in chemical kinetics. *Comm. in Comput. Physics*, 2:964–992, 2007.

[17] E. Chiavazzo, I. V. Karlin, C. E. Frouzakis, and K Boulouchos. Method of invariant grid for model reduction of hydrogen combustion. *Proceedings of the Combustion Institute*, 32:519–526, 2009.

[18] S. S. Chikatamarla. *Hierarchy of lattice Boltzmann models for fluid mechanics.* PhD thesis, Swiss Federal Institute of Technology, ETH-Zurich, 2008.

[19] P. Constantin, C. Foias, B. Nicolaenko, and R. Temam. Integral manifolds and inertial manifolds for dissipative partial differential equations. *Applied Math. Sci.*, 70, 1988.

[20] R. Courant, K. O. Friedrichs, and H. Lewy. On the partial difference equations of mathematical physics. *IBM J.*, 11:215–234, 1967.

[21] A. Debussche and R. Temam. Inertial manifolds and slow manifolds. *Appl. Math. Lett.*, 4:73–76, 1991.

[22] V. I. Dimitrov. Partial kinetic models in the h_2-o_2 system. *Reaction Kinetics and Catalysis Letters*, 7(1):111–114, 1977.

[23] C. A. Eckett. *Numerical and Analytical Studies of the Dynamics of Gaseous Detonations*. PhD thesis, California Institute of Technology, Pasadena, 2001.

[24] C. E. Frouzakis and K. Boulouchos. Analysis and reduction of the ch_4-air mechanism at lean conditions. *Comb. Sci. Tech.*, 159:281–303, 2000.

[25] G. W. Gibbs. *Elementary Principles of Statistical Mechanics*. Dover, 1960.

[26] A. N. Gorban and I. V. Karlin. Method of invariant manifold for chemical kinetics. *Chem. Eng. Sci.*, 58:4751–4768, 2003.

[27] A. N. Gorban and I. V. Karlin. Thermodynamic parametrization. *Physica A*, 190:393–404, 1992.

[28] A. N. Gorban and I. V. Karlin. *Invariant Manifolds for Physical and Chemical Kinetics*. Springer, Berlin, 2005.

[29] A. N. Gorban, P. A. Gorban, and I. V. Karlin. Legendre integrators, post-processing and quasiequilibrium. *J. Non-Newt. Fluid Mech.*, 120: 149–167, 2004.

[30] A. N. Gorban, I. V. Karlin, and A. Y. Zinovyev. Invariant grids for reaction kinetics. *Physica A*, 333:106–154, 2004.

[31] A.N. Gorban and I.V. Karlin. Uniqueness of thermodynamic projector and kinetic basis of molecular individualism. *Physica A*, 336:391–432, 2004.

[32] A.N. Gorban, I.V. Karlin, V.B. Zmievskii, and T.F. Nonnenmacher. Relaxational trajectories: global approximations. *Physica A*, 231: 648–672, 1996.

[33] D.A. Goussis and M. Valorani. An efficient iterative algorithm for the approximation of the fast and slow dynamics of stiff systems. *J. Comput. Phys.*, 214:316–346, 2006.

[34] D. Hamiroune, P. Bishnu, M. Metghalchi, and J. C. Keck. Rate-controlled constrained-equilibrium method using constraint potentials. *Combust. Theory Model.*, 2:81–94, 1998.

[35] P. Ilg, I. V. Karlin, and H. C. Öttinger. Canonical distribution functions in polymer dynamics. (i). dilute solutions of flexible polymers. *Physica A*, 315:367–385, 2002.

[36] E. T. Jaynes. Information theory and statistical mechanics. *Statistical Physics*, 3:160–185, 1963.

[37] I. V. Karlin, A. Ferrante, and H. C. Öttinger. Perfect entropy functions of the lattice boltzmann method. *Europhys. Lett.*, 47:182–188.

[38] N. Kazantzis. Singular pdes and the problem of finding invariant manifolds for nonlinear dynamical systems. *Phys. Lett. A*, 272:257–263, 2000.

[39] J. C. Keck and D. Gillespie. Rate-controlled partial-equilibrium method for treating reacting gas-mixtures. *Combust. Flame*, 17:237–241.

[40] R.J. Kee, G. Dixon-Lewis, J. Warnatz, M.E. Coltrin, and J.A. Miller. Report no. sand86-8246. *Sandia National Laboratories*, 1996.

[41] S. H. Lam and D. A. Goussis. *Conventional asymptotic and computational singular perturbation for symplified kinetics modelling.* Springer, Berlin, 1991.

[42] S. H. Lam and D. A. Goussis. The csp method for simplifying kinetics. *Int. J. Chem. Kin.*, 26:461–486, 1994.

[43] C. K. Law and O. C. Kwon. Effects of hydrocarbon substitution on atmospheric hydrogen-air flame propagation. *Int. Jour. of hydrogen energy*, 29:867–879, 2004.

[44] J. Li, Z. Zhao, A. Kazakov, and F. L. Dryer. *Int. J. Chem. Kinet.*, 36:566–575, 2004.

[45] P. A. Libby and F. A. Williams. *Turbulent Reactive Flows.* Springer, New York, 1980.

[46] A. M. Lyapunov. *The general problem of the stability of motion.* Taylor & Francis, 1992.

[47] U. Maas and S. B. Pope. Simplifying chemical kinetics: Intrinsic low-dimensional manifolds in composition space. *Combust. Flame*, 88: 239–264, 1992.

[48] R. S. MacKay. Slow manifolds. *Energy Localisation and Transfer*, pages 149–192, 2004.

[49] J. Nafe and U. Maas. A general algorithm for improving ildms. *Combust. Theory Modelling*, 6:697–709, 2002.

[50] N. Peters. Systematic reduction of flame kinetics: Principles and details. *Prog. Astronaut. Aeronaut.*, 113:67–86, 1988.

[51] N. Peters. Reducing mechanism. In M. D. Smooke, editor, *Reduced Kinetic Mechanisms and Asymptotic Approximations for Methane-Air Flames*, pages 48–67. Springer-Verlag.

[52] N. Peters and B. Rogg. *Reduced Kinetic Mechanisms for Applications in Combustion Systems*. Springer-Verlag, 1992.

[53] S. B. Pope. Gibbs function continuation for the stable computation of chemical equilibrium. *Combust. Flame*, 139:222–226, 2004.

[54] N. Prasianakis. *Lattice Boltzmann Method for Thermal Compressible Flows*. PhD thesis, Swiss Federal Institute of Technology, ETH-Zurich, 2008.

[55] N. Prasianakis and I. V. Karlin. Lattice boltzmann method for thermal flow simulation on standard lattices. *Phys. Rev. E*, 76, 2007.

[56] H. Rabitz. Chemical dynamics and kinetics phenomena as revealed by sensitivity analysis techniques. *Chemical Review*, 87:101–112, 1987.

[57] H. Rabitz, M. Kramer, and D. Dacol. Sensitivity analysis in chemical kinetics. *Ann. Rev. Phys. Chem.*, 34:419–461, 1983.

[58] A. G. Ramm. Invariant manifolds for dissipative systems. *Journal of Mathematical Physics*, 50:042701, 2009.

[59] W. C. Reynolds. The element potential method for chemical equilibrium analysis: Implementation in the interactive program stanjan. *Mechanical Engineering Department, Standford University*, 1986.

[60] J.C. Robinson. A concise proof of the “geometric" construction of inertial manifolds. *Phy. Lett. A*, 200:415–417, 1995.

[61] R. T. Rockafellar. *Convex Analysis*. paperback edition, 1996.

[62] S. M. Rump. INTLAB – INTerval LABoratory. In T. Csendes, editor, *Developments in Reliable Computing*, pages 77–104. Kluwer Academic Publishers, Dordrecht, 1999.

[63] L.B. Ryashko and E.E. Shnol. On exponentially attracting invariant manifolds of odes. *Nonlinearity*, 16:147–160, 2003.

[64] S. Succi. *The Lattice Boltzmann Equation for Fluid Dynamics and Beyond*. Oxford University Press, Oxford, 2001.

[65] Q. Tang and S. B. Pope. A more accurate projection in the rate-controlled constrained-equilibrium method for dimension reduction of combustion chemistry. *Combust. Theory Model.*, 8:255–279, 2004.

[66] A. S. Tomlin, T. Turanyi, and M. J. Pilling. Mathematical tools for the construction, investigation and reduction of combustion mechanisms. In M. J. Pilling, editor, *Low-Temperature Combustion and Autoignition*, pages 293–437. Elsevier.

[67] J. Warnatz, U. Maas, and R. W. Dibble. *Combustion: Physical and Chemical Fundamentals, Modeling and Simulation, Experiments, Pollutant Formation.* Hardcover, 2006.

[68] F. A. Williams. *Combustion Theory. The fundamental theory of chemically reactive flow systems.* Addison-Wesley Publishing Company, 1985.

[69] K. Yamamoto, X. He, and G. D. Doolen. Simulation of combustion fields with lattice boltzmann method. *J. Stat. Phys.*, 107:367–383, 2002.

Appendix

A. Lyapunov function and its derivatives

Here, we assume that the reaction kinetic equations (1.4), together with a proper closure, describe the temporal evolution of a closed reactive system towards a unique steady state. In particular, three classical conditions are considered in this study:

1. isochoric isothermal system;
2. isobaric isenthalpic system;
3. isolated system.

Due to the second law of thermodynamics, for all those cases there exists a strictly convex function, only dependent on the state, that decreases monotonically in time under the dynamics dictated by the kinetic equations. Such a function is a global Lyapunov function with respect to the system of kinetic equations, and it reaches its global minimum at the steady state. In particular, under isochoric and isothermal conditions, a Lyapunov function is related to the mixture Helmholtz free energy

$$G = \sum_{i=1}^{n} c_i \left[\ln\left(\frac{c_i}{c_i^{ss}}\right) - 1 \right], \tag{A.1}$$

expressed in terms of molar concentrations c_i, where $\boldsymbol{c}^{ss} = (c_1^{ss}, ..., c_n^{ss})$ is the steady state. In this case, the first and second derivatives of G take a particularly simple form:

$$\boldsymbol{\nabla} G\,(i) = \left.\frac{\partial G}{\partial c_i}\right|_{V,T} = \ln\left(\frac{c_i}{c_i^{ss}}\right), \quad \boldsymbol{H}(i,j) = \left.\frac{\partial^2 G}{\partial c_i \partial c_j}\right|_{V,T} = \delta_{ij}\frac{1}{c_i}, \tag{A.2}$$

with δ_{ij} denoting the kronecker delta.

For both isobaric isenthalpic mixtures and isolated systems, the Lyapunov function is related to the specific mixture-averaged entropy (in mass units)

as follows:

$$G = -\frac{1}{\bar{W}} \sum_{i=1}^{n} \left[s_i(T) - \mathcal{R} \ln(X_i) - \mathcal{R} \ln\left(\frac{p}{p_{ref}}\right) \right] X_i + \sum_{k=1}^{d} \left(\lambda_k \sum_{i=1}^{n} \frac{\mu_{ik}}{W_i} Y_i \right), \tag{A.3}$$

where the evaluation of the Lagrange multipliers λ_k is discussed below, while the mixture mean molecular weight $\bar{W}$ and the mole fraction X_k can be expressed in terms of the mass fractions as

$$\bar{W} = \frac{1}{\sum_{j=1}^{n} Y_j / W_j}, \quad X_k = \frac{Y_k}{W_k \sum_{j=1}^{n} Y_j / W_j}. \tag{A.4}$$

The specific entropy s_j of species j depends on temperature as follows

$$s_j(T) = \mathcal{R} \left(a_{1j} \ln T + a_{2j} T + \frac{a_{3j}}{2} T^2 + \frac{a_{4j}}{3} T^3 + \frac{a_{5j}}{4} T^4 + a_{7j} \right), \tag{A.5}$$

and p_{ref} represents a reference pressure, which generally is assumed to be $1bar$. This time, the computation of the gradient $\boldsymbol{\nabla} G$ and the Hessian matrix $\boldsymbol{H}$ is not straightforward any longer, since (A.3) explicitly depends on the temperature, which is in turn implicit function of $\bar{h}$ or $\bar{U}$ through the non-linear relations in (1.8) and (1.10).

During our study, three approaches have been implemented and tested. The first approach is named *finite differencing*, and it approximates the exact first derivative (e.g. for isobaric isenthalpic systems) making use of the following ratio:

$$\left.\frac{\partial G}{\partial c_i}\right|_{p,\bar{h}} \cong \frac{G(T', \ldots, c_i + \varepsilon, \ldots) - G(T, \ldots, c_i, \ldots)}{\varepsilon}, \tag{A.6}$$

with the temperature T' evaluated by solving (e.g. iteratively by Newton-Raphson method) the following equation:

$$\bar{h}(T', \ldots, c_i + \varepsilon, \ldots) = \bar{h}(T, \ldots, c_i, \ldots). \tag{A.7}$$

In general, first derivatives are evaluated using either forward (such as (A.6)) or backward approximations, while central schemes are preferred for second derivatives. Moreover, in order to improve the accuracy, the

positive small parameter ε must be chosen of the order of the square root of machine precision. More details can be found in [8].

According to the second approach, it is possible to differentiate (in principle up to any order) the subroutine itself which evaluates the function (A.3): generally, such a technique is referred to as *automatic differentiation* (AD). In our case with fixed $\bar{h}$ and p, the AD was applied to the main subroutine implementing (A.3), where the temperature is given by a secondary subroutine implementing a Newton-Raphson method for solving the enthalpy conservation equation in (1.10). The AD systematically applies the chain rule to the full sequence of elementary assignments in the code, and it provides with exact values of the derivatives, which are thus not affected by any round-off errors (unlike the finite differencing). However, by using INTLAB [62] for Matlab, we have found that the AD is slower than the finite differencing by an order of magnitude. Finally, it is possible to find the exact form of the derivatives of G, and in the following we first illustrate this approach for an isobaric isenthalpic reactor.

The mixture-averaged specific enthalpy for an ideal mixture is

$$\bar{h}\left(T, Y_i\right) = \sum_{i=1}^{n} h_i\left(T\right) Y_i. \tag{A.8}$$

The total differential $d\bar{h}$ takes the form:

$$d\bar{h}\left(T, Y_i\right) = \left.\frac{\partial \bar{h}}{\partial T}\right|_{Y_i} dT + \left.\frac{\partial \bar{h}}{\partial Y_1}\right|_{T, Y_{i\neq 1}} dY_1 + \cdots + \left.\frac{\partial \bar{h}}{\partial Y_n}\right|_{T, Y_{i\neq n}} dY_n. \tag{A.9}$$

Setting $d\bar{h} = 0$ (isenthalpic system), and recording the definition of mixture-averaged specific heat under constant pressure $\bar{C}_p$ and specific enthalpies h_i, the exact differential of temperature is written as:

$$dT = -\frac{1}{\bar{C}_p\left(T, Y_1, ..., Y_n\right)} \sum_{i=1}^{n} h_i\left(T\right) dY_i. \tag{A.10}$$

In other words, the partial derivatives of temperature under constant pressure and mixture-averaged specific enthalpy read:

$$\left.\frac{\partial T}{\partial Y_i}\right|_{p,\bar{h}} = -\frac{h_i\left(T\right)}{\bar{C}_p\left(T, Y_1, ..., Y_n\right)} = -\frac{h_i\left(T\right)}{\sum\limits_{j=1}^{n} C_{pj}\left(T\right) Y_j}, \tag{A.11}$$

where the fit for the specific heat C_{pj} of species j takes the form [40]

$$C_{pj}(T) = \mathcal{R}\left(a_{1j} + a_{2j}T + a_{3j}T^2 + a_{4j}T^3 + a_{5j}T^4\right). \tag{A.12}$$

The derivative of (A.11), with respect to Y_j, reads

$$\left.\frac{\partial^2 T}{\partial Y_i \partial Y_j}\right|_{p,\bar{h}} = \frac{h_i(T)\, C_{pj}(T)}{\bar{C}_p^2(T, Y_1, ..., Y_n)} - \frac{h_i(T)\, h_j(T)}{\bar{C}_p^3(T, Y_1, ..., Y_n)} \sum_{k=1}^{n} Y_k \frac{\partial C_{pk}}{\partial T}(T). \tag{A.13}$$

By making use of the relations (A.4) and the chain rule, it is now possible to write explicitly the components of the gradient $\boldsymbol{\nabla} G$,

$$\left.\frac{\partial G}{\partial Y_i}\right|_{p,\bar{h}} = -\frac{s_i}{W_i} - \left.\frac{\partial T}{\partial Y_i}\right|_{p,\bar{h}} \sum_{k=1}^{n} \frac{Y_k}{W_k}\frac{\partial s_k}{\partial T} + \frac{\mathcal{R}}{W_i} \ln\left(\frac{Y_i \bar{W}}{W_i}\right) + \frac{\mathcal{R}}{W_i} \ln\left(\frac{p}{p_{ref}}\right) + \sum_{k=1}^{d} \lambda_k \frac{\mu_{ik}}{W_i}, \tag{A.14}$$

and of the Hessian matrix $\boldsymbol{H}$,

$$\begin{aligned}\left.\frac{\partial^2 G}{\partial Y_i \partial Y_j}\right|_{p,\bar{h}} = \frac{-1}{W_i}\frac{\partial s_i}{\partial T}\left.\frac{\partial T}{\partial Y_j}\right|_{p,\bar{h}} - \frac{1}{W_j}\frac{\partial s_j}{\partial T}\left.\frac{\partial T}{\partial Y_i}\right|_{p,\bar{h}} - \\ \left.\frac{\partial^2 T}{\partial Y_i \partial Y_j}\right|_{p,\bar{h}} \sum_{k=1}^{n} \frac{Y_k}{W_k}\frac{\partial s_k}{\partial T} - \\ \left.\frac{\partial T}{\partial Y_i}\right|_{p,\bar{h}} \left.\frac{\partial T}{\partial Y_j}\right|_{p,\bar{h}} \sum_{k=1}^{n} \frac{Y_k}{W_k}\frac{\partial^2 s_k}{\partial T^2} + \frac{\mathcal{R}}{W_i}\left(\frac{\delta_{ij}}{Y_i} - \frac{\bar{W}}{W_j}\right).\end{aligned} \tag{A.15}$$

Let us assume that the steady state of the system has been computed (e.g. using STANJAN [59]). Let $\partial G^*/\partial Y_i$ be the first derivative of G, at the steady state, evaluated by setting $\lambda_k = 0$, $k = 1, ..., d$, in (A.14). Imposing the following zero-gradient condition at the steady state (point of global minimum):

$$\begin{bmatrix} \frac{\mu_{11}}{W_1} & \cdots & \frac{\mu_{1d}}{W_d} \\ \vdots & \ddots & \vdots \\ \frac{\mu_{n1}}{W_1} & \cdots & \frac{\mu_{nd}}{W_d} \end{bmatrix} \begin{bmatrix} \lambda_1 \\ \vdots \\ \lambda_d \end{bmatrix} = - \begin{bmatrix} \frac{\partial G^*}{\partial Y_1} \\ \vdots \\ \frac{\partial G^*}{\partial Y_n} \end{bmatrix}, \tag{A.16}$$

and applying the first Gauss transformation to the rectangular algebraic system (A.16), the condition for the Lagrange multipliers λ_k is explicitly

written:

$$\begin{bmatrix} \frac{\mu_{11}}{W_1} & \cdots & \frac{\mu_{1d}}{W_d} \\ \vdots & \ddots & \vdots \\ \frac{\mu_{n1}}{W_1} & \cdots & \frac{\mu_{nd}}{W_d} \end{bmatrix}^T \begin{bmatrix} \frac{\mu_{11}}{W_1} & \cdots & \frac{\mu_{1d}}{W_d} \\ \vdots & \ddots & \vdots \\ \frac{\mu_{n1}}{W_1} & \cdots & \frac{\mu_{nd}}{W_d} \end{bmatrix} \begin{bmatrix} \lambda_1 \\ \vdots \\ \lambda_d \end{bmatrix} =$$
$$- \begin{bmatrix} \frac{\mu_{11}}{W_1} & \cdots & \frac{\mu_{1d}}{W_d} \\ \vdots & \ddots & \vdots \\ \frac{\mu_{n1}}{W_1} & \cdots & \frac{\mu_{nd}}{W_d} \end{bmatrix}^T \begin{bmatrix} \frac{\partial G^*}{\partial Y_1} \\ \vdots \\ \frac{\partial G^*}{\partial Y_n} \end{bmatrix}.$$

The case of an isolated system ($\bar{U}, V = const$) can be analyzed in a similar manner. Indeed, the only changes concern the partial derivatives (A.11) and (A.13),

$$\left.\frac{\partial T}{\partial Y_i}\right|_{V,\bar{U}} = -\frac{U_i(T)}{\bar{C}_v(T, Y_1, ..., Y_n)} = -\frac{U_i(T)}{\sum_{j=1}^{n} C_{vj}(T) Y_j},$$

$$\left.\frac{\partial^2 T}{\partial Y_i \partial Y_j}\right|_{V,\bar{U}} = \frac{e_i(T) C_{vj}(T)}{\bar{C}_v^2(T, Y_1, ..., Y_n)} - \frac{U_i(T) U_j(T)}{\bar{C}_v^3(T, Y_1, ..., Y_n)} \sum_{k=1}^{n} Y_k \frac{\partial C_{vk}}{\partial T}(T),$$

where $\bar{C}_v$ is the mixture-averaged specific heat under constant volume, and $C_{vj}(T)$, for any species j, is given by the Meyer relation:

$$C_{vj} = C_{pj} - \mathcal{R}.$$

Moreover, now the mixture density $\bar{\rho}$ is constant while the pressure

$$p = \bar{\rho} \mathcal{R} T \sum_{i=1}^{n} \frac{Y_i}{W_i}$$

changes in time, and this needs to be taken into account in formulas (A.14) and (A.15).

Note however that, in chapter 6 the isolated chemical system is described in terms of molar concentrations c_i, and in this case it proves more convenient to deal with the Lyapunov function (6.3). Indeed now the mixture density (conserved quantity) can be expressed as a linear combination of molar concentration, $\bar{\rho} = \sum_{i=1}^{n} W_i c_i$, and already taken into account for constructing the Lyapunov function. Thus, all derivatives are computed

under fixed $\bar{U}$, and their explicit expressions are derived below. The conservation of the mixture-averaged internal energy can be written

$$\bar{C}_v dT + \frac{1}{\bar{\rho}} \sum\nolimits_{k=1}^{n} W_k U_k(T)\, dc_k = 0,$$

so that the first and second partial derivatives of temperature with respect to molar concentrations take the form:

$$\left.\frac{\partial T}{\partial c_i}\right|_{\bar{U}} = -\frac{W_i U_i(T)}{\bar{\rho}\bar{C}_v}, \tag{A.17}$$

$$\left.\frac{\partial^2 T}{\partial c_j \partial c_i}\right|_{\bar{U}} = -\frac{W_i\left(\bar{C}_v \frac{dU_i}{dT}\left.\frac{\partial T}{\partial c_j}\right|_{\bar{U}} - U_i \left.\frac{\partial \bar{C}_v}{\partial c_j}\right|_{\bar{U}}\right)}{\rho \bar{C}_v^2}, \tag{A.18}$$

where

$$\bar{C}_v = \frac{1}{\bar{\rho}} \sum\nolimits_{k=1}^{n} W_k C_{vk}(T)\, c_k,\ \left.\frac{\partial \bar{C}_v}{\partial c_j}\right|_{\bar{U}}$$
$$= \frac{1}{\bar{\rho}}\left[\left.\frac{\partial T}{\partial c_j}\right|_{\bar{U}} \left(\sum\nolimits_{k=1}^{n} W_k \frac{dC_{vk}}{dT} c_k\right) + W_j C_{vj}(T)\right].$$

By definition, mole fractions and molar concentrations are related by

$$mix = \sum\nolimits_{j=1}^{n} c_j, \quad X_k = \frac{c_k}{mix},$$

so that the following condition holds:

$$\frac{\partial X_k}{\partial c_i} = \frac{\delta_{ki} mix - c_k}{mix^2}.$$

The gradient of the G function (6.3) has the following components:

$$\left.\frac{\partial G}{\partial c_i}\right|_{\bar{U}} = -\frac{1}{\bar{\rho}}\left[\left.\frac{\partial T}{\partial c_i}\right|_{\bar{U}} \left(\sum\nolimits_{k=1}^{n} \frac{ds_k}{dT} c_k\right) + s_i\right] + \frac{\mathcal{R}}{\bar{\rho}} \ln\left(\frac{c_i}{\sum_{k=1}^{n} c_k}\right) +$$
$$\frac{\mathcal{R}}{\bar{\rho}}\left[\ln\left(\frac{p}{p_{ref}}\right) + \frac{\sum_{k=1}^{n} c_k}{p} \left.\frac{\partial p}{\partial c_i}\right|_{\bar{U}}\right] + \sum\nolimits_{k=1}^{d} \lambda_k \mu_{ik} + \lambda W_i, \tag{A.19}$$

where

$$p = \mathcal{R} T \sum\nolimits_{k=1}^{n} c_k, \quad \left.\frac{\partial p}{\partial c_i}\right|_{\bar{U}} = \mathcal{R} \left.\frac{\partial T}{\partial c_i}\right|_{\bar{U}} \sum\nolimits_{k=1}^{n} c_k + \mathcal{R} T,$$

while the Hessian matrix of G is computed as follows:

$$\begin{aligned}\left.\frac{\partial^2 G}{\partial c_j \partial c_i}\right|_{\bar{U}} = &-\frac{1}{\bar{\rho}} \left.\frac{\partial^2 T}{\partial c_j \partial c_i}\right|_{\bar{U}} \left(\sum\nolimits_{k=1}^{n} \frac{ds_k}{dT} c_k\right) - \\ &\frac{1}{\bar{\rho}} \left.\frac{\partial T}{\partial c_i}\right|_{\bar{U}} \left.\frac{\partial T}{\partial c_j}\right|_{\bar{U}} \left(\sum\nolimits_{k=1}^{n} \frac{d^2 s_k}{dT^2} c_k\right) - \\ &\frac{1}{\bar{\rho}} \left.\frac{\partial T}{\partial c_i}\right|_{\bar{U}} \frac{ds_j}{dT} - \frac{1}{\bar{\rho}} \left.\frac{\partial T}{\partial c_j}\right|_{\bar{U}} \frac{ds_i}{dT} + \frac{\mathcal{R}}{\bar{\rho}} \frac{\sum_{k=1}^{n} c_k}{c_i} \frac{\partial X_i}{\partial c_j} + \\ \frac{\mathcal{R}}{\bar{\rho}} \left[\frac{1}{p} \left(\left.\frac{\partial p}{\partial c_j}\right|_{\bar{U}} + \left.\frac{\partial p}{\partial c_i}\right|_{\bar{U}} \right) - \frac{\sum_{k=1}^{n} c_k}{p^2} \left.\frac{\partial p}{\partial c_j}\right|_{\bar{U}} \left.\frac{\partial p}{\partial c_i}\right|_{\bar{U}} + \frac{1}{\mathcal{R}T} \left.\frac{\partial^2 p}{\partial c_j \partial c_i}\right|_{\bar{U}}\right],\end{aligned}$$

and the second derivative matrix of pressure reads

$$\left.\frac{\partial^2 p}{\partial c_j \partial c_i}\right|_{\bar{U}} = \mathcal{R} \left(\left.\frac{\partial^2 T}{\partial c_j \partial c_i}\right|_{\bar{U}} \sum\nolimits_{k=1}^{n} c_k + \left.\frac{\partial T}{\partial c_i}\right|_{\bar{U}} + \left.\frac{\partial T}{\partial c_j}\right|_{\bar{U}} \right).$$

The Lagrange multipliers λ_k and λ in (A.19) are derived in a similar way as illustrated for the previous case, by imposing zero gradient at the steady state.

B. Jacobian matrix

Let $\boldsymbol{\psi}$ be an arbitrary point of the phase-space. The linearization of the vector field of motion $\boldsymbol{f}$ about $\boldsymbol{\psi}$ is written:

$$\boldsymbol{f}(\boldsymbol{\psi}+\delta\boldsymbol{\psi}) \cong \boldsymbol{f}(\boldsymbol{\psi}) + \boldsymbol{J}(\boldsymbol{\psi})\,\delta\boldsymbol{\psi}, \tag{B.1}$$

where the Jacobian matrix $\boldsymbol{J} = [\partial f_i/\partial Y_j]$ can be related to the Hessian matrix $\boldsymbol{H} = \left[\partial^2 G/\partial Y_i \partial Y_j\right]$ of the Lyapunov function G, and it acts on an arbitrary vector $\boldsymbol{\eta}$ as follows:

$$\boldsymbol{J}\boldsymbol{\eta}^T = \sum_{s=1}^{r} \boldsymbol{\nu}_s \left[\Omega_s^+ \left(\boldsymbol{\alpha}_s \boldsymbol{H}\boldsymbol{\eta}^T\right) - \Omega_s^- \left(\boldsymbol{\beta}_s \boldsymbol{H}\boldsymbol{\eta}^T\right)\right]. \tag{B.2}$$

The matrix $\boldsymbol{J}$ in (B.2) can be decomposed as shown below:

$$\boldsymbol{J} = \boldsymbol{J}' + \boldsymbol{J}'', \tag{B.3}$$

where the two matrices $\boldsymbol{J}'$ and $\boldsymbol{J}''$ act as follows:

$$\boldsymbol{J}'\boldsymbol{\eta}^T = -\frac{1}{2}\sum_{s=1}^{r} \left[\Omega_s^+ + \Omega_s^-\right] \boldsymbol{\nu}_s \left(\boldsymbol{\nu}_s \boldsymbol{H}\boldsymbol{\eta}^T\right), \tag{B.4}$$

$$\boldsymbol{J}''\boldsymbol{\eta}^T = \frac{1}{2}\sum_{s=1}^{r} \left[\Omega_s^+ - \Omega_s^-\right] \boldsymbol{\nu}_s \left(\left(\boldsymbol{\alpha}_s + \boldsymbol{\beta}_s\right) \boldsymbol{H}\boldsymbol{\eta}^T\right). \tag{B.5}$$

The Jacobian decomposition (B.3) splits $\boldsymbol{J}$ in two parts. The first one $\boldsymbol{J}'$ is symmetric in the following sense

$$\boldsymbol{\eta}_1 \boldsymbol{J}' \boldsymbol{H} \boldsymbol{\eta}_2^T = \boldsymbol{\eta}_2 \boldsymbol{J}' \boldsymbol{H} \boldsymbol{\eta}_1^T, \quad \forall \boldsymbol{\eta}_1, \boldsymbol{\eta}_2, \tag{B.6}$$

while the second one $\boldsymbol{J}''$ vanishes at the steady state, due to the principle of detail balance: $\Omega_s^+ = \Omega_s^-$. In other words, at the steady state of the system, we have

$$\boldsymbol{J} = \boldsymbol{J}'. \tag{B.7}$$

The symmetric part $\boldsymbol{J}'$ is relevant to the MIG method, and it takes the following explicit form:

$$\sum_{j=1}^{n} \boldsymbol{J}'(i,j)\,\boldsymbol{\eta}(j) = -\sum_{s=1}^{r} \frac{\Omega_s^+ + \Omega_s^-}{2} \boldsymbol{\nu}_s(i) \sum_{j=1}^{n} \left(\boldsymbol{H}\boldsymbol{\nu}_s^T\right)(j)\,\boldsymbol{\eta}(j)\,,$$

$$\sum_{j=1}^{n} \boldsymbol{J}'(i,j)\,\boldsymbol{\eta}(j) = -\sum_{s=1}^{r} \sum_{j=1}^{n} \frac{\Omega_s^+ + \Omega_s^-}{2} \boldsymbol{\nu}_s(i) \left(\boldsymbol{H}\boldsymbol{\nu}_s^T\right)(j)\,\boldsymbol{\eta}(j)\,,$$

$$\sum_{j=1}^{n} \boldsymbol{J}'(i,j)\,\boldsymbol{\eta}(j) = -\sum_{j=1}^{n} \sum_{s=1}^{r} \frac{\Omega_s^+ + \Omega_s^-}{2} \boldsymbol{\nu}_s(i) \left(\boldsymbol{H}\boldsymbol{\nu}_s^T\right)(j)\,\eta(j)\,,$$

$$\boldsymbol{J}'(i,j) = -\sum_{s=1}^{r} \frac{\Omega_s^+ + \Omega_s^-}{2} \boldsymbol{\nu}_s(i) \left(\boldsymbol{H}\boldsymbol{\nu}_s^T\right)(j)\,. \tag{B.8}$$

Similarly, the non symmetric part of the Jacobian matrix $\boldsymbol{J}''$ can be written as follows:

$$\boldsymbol{J}''(i,j) = \sum_{s=1}^{r} \frac{\Omega_s^+ - \Omega_s^-}{2} \boldsymbol{\nu}_s(i) \left[\boldsymbol{H}\left(\boldsymbol{\alpha}_s + \boldsymbol{\beta}_s\right)^T\right](j)\,. \tag{B.9}$$

Remark. Notice that, any function obtained by multiplying G by an arbitrary factor is still a thermodynamic Lyapunov function of the kinetic equations. Therefore, the matrices $\boldsymbol{J}$, $\boldsymbol{J}'$ and $\boldsymbol{J}''$ can be analytically determined, up to an unknown multiplicative constant, using (B.3), (B.8), (B.9) and the explicit expressions for $\boldsymbol{H}$ described in the Appendix A. Nevertheless, if needed, the unknown multiplicative constant can be recovered by computing the Jacobian $\boldsymbol{J}$ via automatic differentiation only at the steady state, and imposing the condition (B.7).

C. Multi-variate linear interpolation

Let us consider a q-dimensional invariant grid in a n-dimensional phase-space. Let $Y(\xi_1, ..., \xi_q)$ be a scalar quantity defined at a generic grid node. Multi-dimensional interpolation of the function Y, for an arbitrary number of variables q, is generally a non trivial task. Nevertheless, if the variables ξ_i lie on a regular Cartesian grid, the multi-variate linear interpolation may be a convenient option. To this end, the interpolating process is split in three steps:

- locating the grid hyper-cube which bounds the interpolant point;
- evaluation of the weighting functions;
- interpolation.

The pertinent hyper-cube can be identified by the coordinates $\left(\xi_1^*, ..., \xi_q^*\right)$ of one of its corners. Once a reference point $\left(\xi_1^{ref}, ..., \xi_q^{ref}\right)$ has been fixed on the grid, the localizing coordinated are expressed as function of

$$\xi_i^* = \xi_i^* \left(\frac{\xi_i - \xi_i^{ref}}{\Delta\xi_i} \right), \tag{C.1}$$

where $\Delta\xi_i$ is the constant stepping along the ith variable, and $(\xi_1, ..., \xi_q)$ is the interpolant point. Notice that (C.1) can be significantly fast compared to the case of non-uniform grids, where a proper searching algorithm is needed. In two dimensions, the interpolation problem is illustrated in Fig. C.1, where the interpolant point (ξ_1, ξ_2) and its bounding rectangle are reported. In this case, let us define a weighting function π, for each coordinate, as follows

$$\pi_1 = \frac{\xi_1 - \xi_{1,0}}{\xi_{1,1} - \xi_{1,0}}, \quad \pi_2 = \frac{\xi_2 - \xi_{2,0}}{\xi_{2,1} - \xi_{2,0}}. \tag{C.2}$$

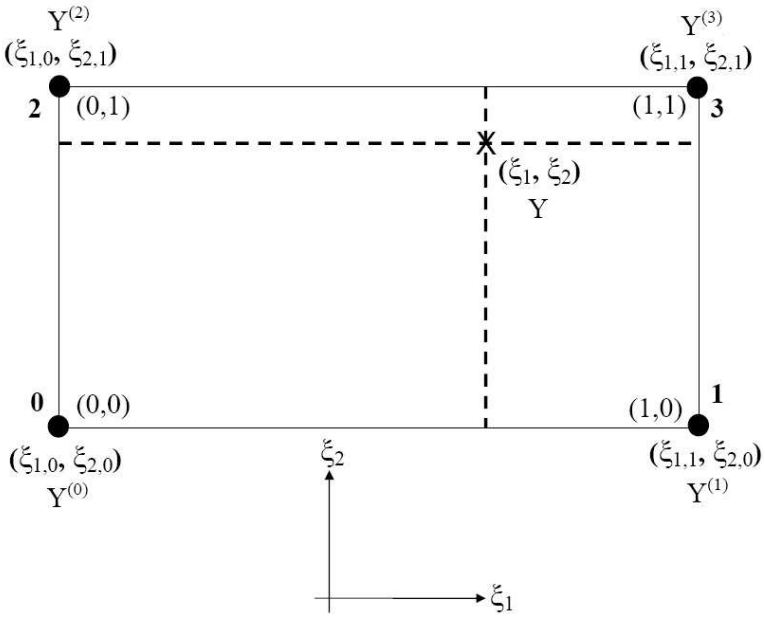

Figure C.1.: Bivariate linear interpolation on a regular Cartesian grid. From [23]

The interpolated scalar Y can be expressed in terms of the function values at the grid points by the relation:

$$Y = Y^{(0)}\left(1-\pi_1\right)\left(1-\pi_2\right) + Y^{(1)}\pi_1\left(1-\pi_2\right) + Y^{(2)}\left(1-\pi_1\right)\pi_2 + Y^{(3)}\pi_1\pi_2. \tag{C.3}$$

The general procedure for interpolating functions with q variables is described below. Let $\left(l_1^{(i)},\ldots,l_q^{(i)}\right)$ identify the points of the bounding hyper-cube, where $l_j^{(i)}$ is a binary number $(0,1)$, for each coordinate $j = 1,...,q$ and each cube corner $i = 0,...,2^q-1$. The location of the corner i, in the variable space, is $\left(\xi_{1,l_1^{(i)}},\ldots,\xi_{q,l_q^{(i)}}\right)$. The numbering scheme is designed such that the corner number i corresponds to the base 10 representation of the base 2 number: $l_q^{(i)}l_{q-1}^{(i)}\ldots l_1^{(i)}$. Therefore the labels are related to the point number by

$$l_j^{(i)} = \text{int}\left(\frac{i}{2^{j-1}}\right) \bmod 2, \tag{C.4}$$

where "int" and "mod" implement the integer and the modulo operator, respectively. The weighting function π_j for the jth coordinate takes the form

$$\pi_j = \frac{\xi_j - \xi_{j,0}}{\xi_{j,1} - \xi_{j,0}}, \tag{C.5}$$

while the the interpolated value is

$$Y = \sum_{i=0}^{2^q-1}\left[Y^{(i)}\prod_{j=1}^{q}\left(l_j^{(i)}\pi_j + \left(1-l_j^{(i)}\right)\left(1-\pi_j\right)\right)\right]. \tag{C.6}$$

D. Detailed mechanism for hydrogen and air

Reaction		A_s	n_s	E_s
1. $H_2 + O_2 \rightleftharpoons O + OH$		3.55×10^{15}	-0.41	16.6
2. $O + H_2 \rightleftharpoons H + OH$		5.08×10^{4}	2.67	6.29
3. $H_2 + OH \rightleftharpoons H_2O + H$		2.16×10^{8}	1.51	3.43
4. $O + H_2O \rightleftharpoons OH + OH$		2.97×10^{6}	2.02	13.4
5. $H_2 + M \rightleftharpoons H + H + M$		4.58×10^{19}	-1.40	104.38
6. $O + O + M \rightleftharpoons O_2 + M$		6.16×10^{15}	-0.50	0.00
7. $O + H + M \rightleftharpoons OH + M$		4.71×10^{18}	-1.0	0.00
8. $H + OH + M \rightleftharpoons H_2O + M$		3.8×10^{22}	-2.00	0.00
9. $H + O_2(+M) \rightleftharpoons HO_2(+M)^a$	k_O	6.37×10^{20}	-1.72	0.52
10. $HO_2 + H \rightleftharpoons H_2 + O_2$		1.66×10^{13}	0.00	0.82
11. $HO_2 + H \rightleftharpoons OH + OH$		7.08×10^{13}	0.00	0.30
12. $HO_2 + O \rightleftharpoons O_2 + OH$		3.25×10^{13}	0.00	0.00
13. $HO_2 + OH \rightleftharpoons H_2O + O_2$		2.89×10^{13}	0.00	-0.50
14. $HO_2 + HO_2 \rightleftharpoons H_2O_2 + O_2$		4.20×10^{14}	0.00	11.98
15. $HO_2 + HO_2 \rightleftharpoons H_2O_2 + O_2$		1.30×10^{11}	0.00	-1.63
16. $H_2O_2(+M) \rightleftharpoons 2OH(+M)^b$	k_O	1.20×10^{17}	0.00	45.5
	k_∞	2.95×10^{14}	0.00	48.4
17. $H_2O_2 + H \rightleftharpoons H_2O + OH$		2.41×10^{13}	0.00	3.97
18. $H_2O_2 + H \rightleftharpoons HO_2 + H_2$		4.82×10^{13}	0.00	7.95
19. $H_2O_2 + O \rightleftharpoons OH + HO_2$		9.55×10^{6}	2.00	3.97
20. $H_2O_2 + OH \rightleftharpoons HO_2 + H_2O$		1.00×10^{12}	0.00	0.00
21. $H_2O_2 + OH \rightleftharpoons HO_2 + H_2O$		5.8×10^{14}	0.00	9.56

Table D.1.: Detailed H_2-air reaction mechanism. Units are cm^3, mol, sec, $Kcal$, K, and $k_s(T) = A_s T^{n_s} exp(-E_s/RT)$. [a]Troe parameter is: $F_c = 0.8$. Efficiency factors are: $\varepsilon_{H_2O} = 10.0$, $\varepsilon_{H_2} = 1.0$ and $\varepsilon_{O_2} = -0.22$. [b]Troe parameter is: $F_c = 0.5$. Efficiency factors are: $\varepsilon_{H_2O} = 11.0$, $\varepsilon_{H_2} = 1.5$.

E. Equilibrium populations for lattice Boltzmann

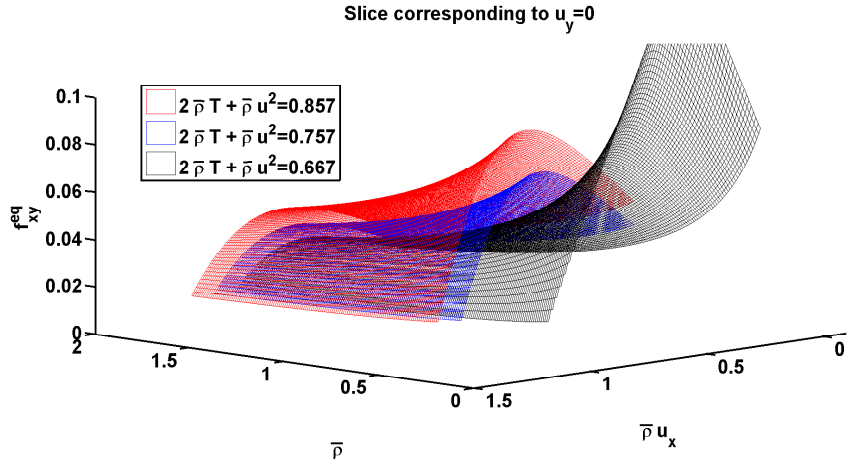

Figure E.1.: Entropic equilibrium population f_{xy}^{eq} for the standard lattice Boltzmann stencil $D2Q9$, with $\varepsilon_k = 1 \times 10^{-2}$.

For illustration purposes, here we use the quasi equilibrium grid algorithm in the form (5.45), for constructing approximate equilibrium populations f_α^{eq} of the entropic lattice Boltzmann method (see section 3.3). By referring to the 2D stencil $D2Q9$ in Fig. 3.2, the solution to the minimization problem of the $\mathcal{H}$-function under fixed density $\bar{\rho}$, momentum $\bar{\rho}\boldsymbol{u}$, and energy $2\bar{\rho}T + \bar{\rho}\boldsymbol{u}^2$

$$\begin{aligned} \min \quad & \mathcal{H} = \textstyle\sum_{\alpha=1}^{9} f_\alpha \ln\left(f_\alpha / w_\alpha\right), \\ s.t. \quad & \textstyle\sum_{\alpha=1}^{9} f_\alpha = \bar{\rho},\ \sum_{\alpha=1}^{9} \boldsymbol{e}_\alpha f_\alpha = \bar{\rho}\boldsymbol{u},\ \sum_{\alpha=1}^{9} \boldsymbol{e}_\alpha^2 f_\alpha = 2\bar{\rho}T + \bar{\rho}\boldsymbol{u}^2, \end{aligned} \tag{E.1}$$

is given by a four-dimensional manifold in a nine-dimensional phase space. Two dimensional slices of the quasi equilibrium grid corresponding to min-

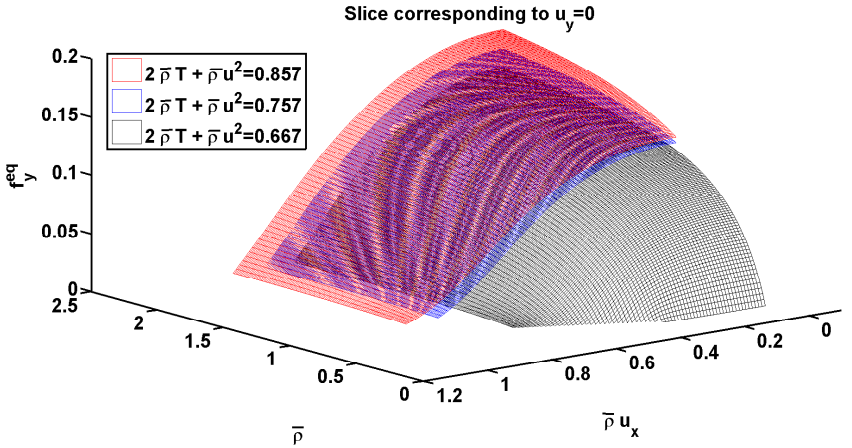

Figure E.2.: Entropic equilibrium population f_y^{eq} for the standard lattice Boltzmann stencil $D2Q9$, with $\varepsilon_k = 1 \times 10^{-2}$.

imization problem (E.1) are shown in Fig. E.1 and E.2 for the populations f_{xy}^{eq} and f_y^{eq}, respectively. Notice that, this time the four reduced description variables ξ^j are represented by density, momentum and energy, while the seed f_α^0 is chosen such that: $f_\alpha^0 = w_\alpha$.